

Temperature, pressure and water content dependence of dislocation mobility in olivine

Dissertation

zur Erlangung der Würde eines
Doktors der Naturwissenschaften

- Dr. rer. nat. -

der Bayreuther Graduiertenschule für Mathematik und Naturwissenschaften

vorgelegt von

Lin Wang

aus Anhui (China)

Bayreuth, 2018

This doctoral thesis was prepared at the department of (department) at the University of Bayreuth from 10.2014 until 04.2018 and was supervised by Prof. Dr. Tomoo Katsura.

This is a full reprint of the dissertation submitted to obtain the academic degree of Doctor of Natural Sciences (Dr. rer. nat.) and approved by the Bayreuth Graduate School of Mathematical and Natural Sciences (BayNAT) of the University of Bayreuth.

Date of submission: 05.04.2018

Date of defence: 10.07.2018

Acting director: Prof. Dr. Dirk Schüler

Doctoral committee:

Prof. Dr. Tomoo Katsura	(reviewer)
Prof. Dr. David Rubie	(reviewer)
Prof. Dr. Daniel Frost	(chairman)
Dr. Gerd Steinle-Neumann	

Table of contents

Summary	5
Zusammenfassung	8
Symbols and definitions	12
1. Introduction to dislocation theory and rheology of the Earth's upper mantle	14
1.1 Theory of dislocations	14
1.1.1 Dislocations	14
1.1.2 Orowan's equation.....	21
1.1.3 Models of dislocation creep.....	23
1.1.4 Other deformation mechanisms.....	29
1.2 Earth's upper mantle rheology	33
1.2.1 Viscosity estimation of the upper mantle.....	33
1.2.2 Seismic anisotropy in the upper mantle	37
1.2.3 Dislocation creep, crystallographic preferred orientation (CPO), mantle flow and seismic anisotropy	38
1.3 Mineralogical models of the Earth's mantle.....	40
1.4 Experimental techniques to study the upper mantle rheology	42
1.4.1 Deformation techniques	42
1.4.2 Diffusion techniques	44
1.4.3 Dislocation recovery techniques.....	45
1.5 Previous studies on rheological properties of olivine.....	47
1.5.1 Deformation experiments.....	47
1.5.2 Diffusion experiments.....	54
1.5.3 Dislocation recovery experiments	57
1.6 Aims of this study.....	60
1.6.1 Temperature dependence of annihilation rate constants for A-type and B-type dislocations	61

1.6.2	Pressure dependence of annihilation rate constants for A-type and B-type dislocations	61
1.6.3	Water dependence of annihilation rate constants for C-type dislocations.....	62
1.6.4	TEM study of E-type dislocations at different conditions.....	63
1.6.5	Examination of cross-slip as a controlled mechanism for olivine deformation.....	63
1.7	General techniques in this study	64
1.7.1	Sample preparation	64
1.7.2	Deformation experiments.....	65
1.7.3	Dislocation recovery	66
1.7.4	Observations of dislocations	66
1.7.5	Data reductions.....	67
1.8	References	67
2.	List of manuscripts and statements of author's contribution	75
3.	Temperature dependence of [100](010) and [001](010) dislocation mobility in natural olivine	77
3.1	Abstract.....	77
3.2	Introduction	77
3.3	Experimental Procedures.....	81
	Sample Preparation	81
	Production of high dislocation densities.....	81
	Dislocation annihilation by annealing.....	83
	Measurement of dislocation density	84
	TEM observation.....	84
	Data reduction	85
3.4	Results.....	86
3.5	Discussion.....	91
	Comparison with previous studies.....	91
	Comparison of results with other techniques	92
	Geophysics application	93
3.6	Conclusion.....	96

3.7	Acknowledgements.....	97
3.8	References.....	97
4.	Identical activation volumes of dislocation mobility in the [100](010) and [001](010) slip systems in natural olivine	102
4.1	Abstract	102
4.2	Introduction	102
4.3	Experimental Procedures.....	104
4.4	Results	105
4.5	Discussion.....	108
	Diffusion-controlled dislocation motion in recovery process.....	108
	Comparison with previous studies.....	109
	Comparison with other techniques	110
	Geophysical application	111
4.6	Acknowledgements.....	111
4.7	References.....	112
5.	Identical mechanism for the motion of screw and edge dislocations in natural olivine	116
5.1	Abstract	116
5.2	Introduction	116
5.3	Experimental Procedures.....	118
5.4	Results	120
5.5	Discussion.....	122
5.6	Implications.....	124
5.7	Acknowledgements.....	126
5.8	References.....	126
6.	Activation of [100](001) slip system by water incorporation in olivine.....	129
6.1	Abstract	129
6.2	Introduction	130
6.3	Experimental Procedures.....	132
	Sample Preparation	132

Hydration/dehydration experiments	132
Deformation experiments.....	134
FT-IR measurements	135
TEM observation	135
6.4 Results	136
6.5 Discussion.....	140
Comparison of the dislocation microstructures with previous studies	140
The mechanism of activation of the [100](001) slip system due to water incorporation.....	141
6.6 Implications.....	142
6.7 Acknowledgements.....	142
6.8 References.....	143
7 Small effect of water on olivine dislocation creep.....	147
7.1 Abstract.....	147
7.2 Introduction	147
7.3 Experimental Procedures.....	150
Sample Preparation	150
Hydration/dehydration experiments.....	150
Deformation experiments.....	151
TEM observation	152
Recovery experiments	153
FT-IR measurements	153
Measurement of dislocation density and data reduction	154
7.4 Results	154
7.5 Discussion.....	158
Comparison with previous studies.....	158
Geophysical implications	160
7.6 Acknowledgements.....	161
7.7 References.....	161
Acknowledgments.....	165

Summary

This thesis is a comprehensive study of dislocation in natural olivine. Since olivine is the most abundant and weakest mineral in the Earth's upper mantle, it is believed that the upper mantle dynamics are controlled by the rheological properties of olivine. Dislocation creep is considered as the most important mechanism for olivine creep at the upper mantle for the following reasons. First, a large amount of strain is accommodated by dislocation creep, and therefore the viscosity of the upper mantle is determined by dislocation creep to a large extent. Second, olivine fabrics, which can reflect mantle flow geometry, are due to dislocation creep. Previous deformation and diffusion experiments gave some information on olivine dislocation creep. However, both of them have limitations. On one hand, the high strain rates in deformation experiments make the application of results from these experiments to natural conditions doubtful. On the other hand, the link between diffusion and dislocation creep is rather indirect. The application of results from diffusion experiments to natural conditions has to be based on certain creep models. In this project, dislocation recovery method was used to study the dislocation motions in natural olivine and investigate upper mantle rheology. In addition, transmission electron microscopy (TEM) was used to make observations to check whether $[100](001)$ slip system exists at hydrous conditions or not.

Temperature dependence of $[100](010)$ and $[001](010)$ slip system

The decrease of seismic anisotropy with depth [e.g. *Dziewonski and Anderson, 1981; Gung et al., 2003; Mainprice et al., 2000; Montagner and Kennett, 1996*] can be explained by olivine fabric transition of A- to B-type due to temperature [e.g. *Carter and Ave'Lallemant, 1970*] based on deformation experiments. However, stresses and strain rates in these experiments are much higher than those in natural conditions. Therefore, the results from deformation experiments have to be examined by an independent method. Dislocation recovery was employed to measure the annihilation rate constants of dislocations in the

[100](010) and [001](010) slip systems in olivine single crystals at temperatures of 1,450 to 1,760 K, room pressure, and oxygen partial pressures near the Ni-NiO buffer conditions in order to determine the temperature dependences for these two slip systems. The activation energies for both slip systems are identical, i.e. 400 kJ/mol, indicating identical temperature dependences for these two slip systems. Therefore, temperature cannot cause the A- to B-type fabric transition.

Pressure dependence of [100](010) and [001](010) slip system

Pressure was proposed as a reason for the A- to B-type fabric transition in olivine based on deformation experiments [e.g. *Raterron et al.*, 2009]. In order to test whether this is true or not at low stress conditions, dislocation recovery experiments were conducted on olivine single crystals for [100](010) and [001](010) slip systems at pressures of 2 to 12 GPa, 1650 K and oxygen fugacity at Ni-NiO buffer conditions. The activation volumes for these two slip systems are identical, i.e. 2.5 cm³/mol. Therefore, pressure cannot cause the A- to B-type fabric transition at low stress conditions. Moreover, since the activation volume is small, the effect of pressure on dislocation creep is also small.

Rate-limiting process of motions of screw dislocation in natural olivine

The traditional climb-model for dislocation creep assumes that the rate-limiting process for dislocation motions is climb of edge dislocations. However, motions of both edge and screw dislocations are needed to produce macroscopic strain in a material. If the rate-limiting process of motions of screw dislocations is different from that of edge dislocations, the climb-model must be modified. Dislocation recovery experiments were conducted on [001](010) screw and edge dislocations in olivine single crystals at 1473 to 1673 K, room pressure and oxygen partial pressure near the Ni-NiO buffer conditions. The activation energy for the motions of screw and edge dislocations are identical, i.e. 400 kJ/mol. Therefore, the

rate-limiting process of motions of screw dislocations is identical to that of edge dislocations. Thus, the climb-model can be applied to not only to edge but also screw dislocations.

Activation of [100](001) slip system by water incorporation in olivine

E-type fabric has been proposed as the dominant fabric at moderate water content and low stress conditions [Katayama *et al.*, 2004]. This indicates that the [100](001) slip system must dominate at such conditions. However, there is no previous study to confirm its existence at such conditions. TEM observations were conducted on olivine single crystals that were simple sheared the [100] direction on the (001) plane at anhydrous and hydrous conditions. The (001) plane was found as a slip plane only at hydrous conditions. Therefore, incorporation of water into olivine helps to activate the [100](001) slip system.

Water dependence of [001](100) slip system

The effect of water on olivine dislocation creep has been under debate recently. Deformation experiments suggested that the dislocation creep rate of olivine aggregates is enhanced by water with a power of 1.2 [e.g. Hirth and Kohlstedt *et al.*, 2003] and that [001](100) slip system has the largest water dependence among all slip systems in olivine [e.g. Jung and Karato., 2001]. In contrast, Si diffusion experiments suggested that the water dependence of dislocation creep is small [Fei *et al.*, 2013]. In this study, dislocation recovery experiments were conducted on pre-deformed olivine single crystals at 1,473 K, 5 GPa, and oxygen fugacity near the enstatite-magnesite-olivine-graphite (EMOG) buffer at water contents ranging from 5 to 90 wt. ppm to determine the annihilation rates for [001] dislocations on the (100) plane. The dislocation annihilation rate constants increase with water content with a power of 0.3. Therefore, water has only a small effect on olivine dislocation creep.

Zusammenfassung

Diese Doktorarbeit ist eine umfangreiche Studie über Versetzungen in natürlichem Olivin. Da Olivin das am häufigsten vorkommende und gleichzeitig mechanisch schwächste Mineral im oberen Erdmantel ist, wird angenommen, dass die rheologischen Eigenschaften von Olivin die Dynamik des oberen Erdmantels kontrollieren. Als wichtigster Mechanismus für Kriechen von Olivin im oberen Mantel wird das Versetzungskriechen angesehen. Die Gründe dafür sind erstens die Aufnahme eines hohen Anteils von Verformung durch Versetzungskriechen, sodass die Viskosität des oberen Mantels weitgehend durch Versetzungskriechen bestimmt wird. Zweitens werden Olivin-Texturen, welche Fließmuster im Mantel widerspiegeln können, durch Versetzungskriechen verursacht. Vorhergehende Verformungs- und Diffusionsexperimente gaben Aufschluss über das Versetzungskriechen von Olivin, haben jedoch Einschränkungen. Zum einen ist die Anwendung von Ergebnissen, die in Verformungsexperimenten unter hohen Verformungsraten ermittelt worden sind, auf natürliche Bedingungen zweifelhaft, zum anderen ist der Zusammenhang zwischen Diffusion und Versetzungskriechen nur indirekt. Die Anwendung der Ergebnisse aus Diffusionsexperimenten auf natürliche Bedingungen muss auf spezifischen Kriechmodellen basieren. In diesem Projekt wurde hauptsächlich eine Methode genutzt, bei der die Erholung von Versetzungen verursacht wird (Versetzungs-Erholungs-Methode), um die Versetzungsbewegungen in natürlichem Olivin zu analysieren und dadurch die Rheologie des oberen Mantels zu untersuchen.

Des Weiteren wurde mithilfe von transmissionselektronenmikroskopischen (TEM) Untersuchungen geprüft, ob das $[100](001)$ Gleitsystem bei wasserhaltigen Bedingungen existiert.

Temperaturabhängigkeit der $[100](010)$ und $[001](010)$ Gleitsysteme

Die Verminderung der seismischen Anisotropie mit zunehmender Tiefe [z.B. *Dziewonski und Anderson*, 1981; *Gung et al.*, 2003; *Mainprice et al.*, 2000; *Montagner und Kennett*, 1996]

kann durch einen Übergang der Textur von A- zu B-Typ aufgrund von Temperaturänderung [z.B. Carter und Ave'Lallemant, 1970] erklärt werden. Diese Kenntnisse basieren auf den Ergebnissen aus Verformungsexperimenten. Mechanische Spannungs- und Verformungsraten unter experimentellen Bedingungen sind jedoch signifikant höher als unter natürlichen Bedingungen.

Deswegen müssen Ergebnisse, die aus Verformungsexperimenten gewonnen werden, mit einer unabhängigen Methode überprüft werden.

Es wurde die Versetzungs-Erholungs-Methode an Olivin-Einkristallen, um die Konstanten der Annihilationsraten von Versetzungen in den [100](010) und [001](010) Gleitsystemen bei Temperaturen von 1,450 bis 1,760 K, Raumdruck und einem Sauerstoff-Partial-Druck im Bereich des Ni-NiO-Puffers zu messen. Aus diesen Konstanten kann eine Temperaturabhängigkeit für die beiden genannten Gleitsysteme bestimmt werden. Die Aktivierungsenergien für die genannten Gleitsysteme sind mit 400 kJ/mol identisch, welches auf eine identische Temperaturabhängigkeit hinweist. Daher kann Temperaturänderung nicht die Texturentwicklung von A zu B-Typ verursachen.

Druckabhängigkeit des [100](010) und [001](010) Gleitsystems

Aufgrund von weiteren Verformungsexperimenten [z.B. Raterron et al., 2009] wird eine Druckänderung als Grund für den Übergang von A- zu B-Typ Textur in Olivin vorgeschlagen. Um dies bei niedriger mechanischer Spannung zu testen, wurden Experimente zur Versetzungs-Erholung an Olivin-Einkristallen für die [100](010) und [001](010) Gleitsysteme bei Drücken von 2 bis 12 GPa, 1,650 K und Sauerstoffugazitäten im Bereich des Ni-NiO Puffers durchgeführt. Die Aktivierungsvolumina für die genannten Gleitsysteme sind mit 2.5 cm³/mol identisch. Deshalb kann eine Druckänderung nicht den Übergang von A- zu B-Typ Textur bei niedrigen mechanischen Spannungen verursachen.

Zudem ist der Druckeffekt auf Versetzungskriechen aufgrund des niedrigen Aktivierungsvolumens ebenfalls gering.

Geschwindigkeitsbestimmender Prozess von Bewegungen von Schraubenversetzungen in natürlichem Olivin

Im klassischen Modell über Versetzungskriechen durch Klettern der Versetzungen wird angenommen, dass der geschwindigkeitsbestimmende Prozess für Versetzungsbewegungen das Klettern von Stufenversetzungen ist. Jedoch werden Bewegungen von Stufen- sowie Schraubenversetzungen benötigt, um makroskopische Verformung in einem Material hervorzurufen. Wenn sich der geschwindigkeitsbestimmende Prozess von Schraubenversetzungsbewegungen von dem von Stufenversetzungsbewegungen unterscheidet, muss das Modell über Versetzungskriechen durch Klettern der Versetzungen modifiziert werden. Es wurden Experimente zur Versetzungs-Erholung an [001](010) Schrauben- und Stufenversetzungen bei Temperaturen von 1,473 bis 1,673 K, Raumdruck und einer Sauerstoff fugazität im Bereich des Ni-NiO Puffers durchgeführt. Die Aktivierungsenergie für die Bewegung von Schrauben- und Stufenversetzungen ist mit 400 kJ/mol identisch. Daraus ergibt sich, dass der geschwindigkeitsbegrenzende Prozess von Schraubenversetzungsbewegungen der gleiche Prozess für Stufenversetzungen ist. Das Versetzungsklettern-Modell kann daher nicht nur für Stufen-, sondern auch für Schraubenversetzungen angewendet werden.

Aktivierung des [100](001) Gleitsystems durch die Aufnahme von Wasser in Olivin

Die E-Typ Textur wurde als dominierende Textur bei moderaten Wassergehalten und Bedingungen niedriger mechanischer Spannung vorgeschlagen [Katayama et al., 2004]. Dies weist darauf hin, dass das [100](001) Gleitsystem unter diesen Bedingungen dominiert. Bisher gibt es keine Studie, die die Existenz dieses Gleitsystems bei den genannten Bedingungen bestätigt. Es wurden TEM Untersuchungen an Olivin-Einkristallen, die in [100] Richtung auf (001) Ebenen geschert wurden, unter trockenen und wasserhaltigen Bedingungen durchgeführt. Die (001) Ebene fungierte nur unter wasserhaltigen Bedingungen als Gleitebene. Daraus wird

geschlussfolgert, dass der Einbau von Wasser in Olivin die Aktivierung des [100](001) Gleitsystems vorantreibt.

Wasser-Abhängigkeit des [100](001) Gleitsystems

Der Effekt von Wasser auf das Versetzungskriechen von Olivin wird zur Zeit stark diskutiert. Verformungsexperimente weisen darauf hin, dass Versetzungskriechraten in polykristallinem Olivin bei Wasseranwesenheit beschleunigt ist und mit der Potenz von 1.2 zunimmt [z.B. Hirth und Kohlstedt et al., 2003]. Das [100](001) Gleitsystem wird als Gleitsystem mit größter Wasserabhängigkeit unter allen vorhandenen Gleitsystemen in Olivin angesehen [z.B. Jung und Karato., 2001]. Im Gegensatz dazu zeigen Si Diffusionsexperimente eine geringe Wasserabhängigkeit von Versetzungskriechen an [Fei et al., 2013]. In dieser Arbeit wurden Experimente zur Versetzungs-Erholung von vorverformten Olivin-Einkristallen bei Temperaturen von 1473 K, 5 GPa und einer Sauerstoffugazität im Bereich des Enstatit-Magnesit-Olivin-Graphit (EMOG) Puffers durchgeführt, um Annihilationsraten für [001] Versetzungen in der (100) Gleitebene zu bestimmen. Die Wassergehalte liegen im Bereich von 5 - 90 ppm. Die Konstanten der Annihilationsraten der Versetzungen steigen mit zunehmenden Wassergehalt mit einer Potenz von 0.3. Daraus wird gefolgert, dass Wasser einen geringen Effekt auf Olivin-Versetzungen hat.

Symbols and definitions

\bar{B} : dislocation mobility tensor

b : Burger's vector of dislocations

c^* : concentration of vacancy under stressed conditions

c^0 : concentration of vacancy at equilibrium conditions

C_{H_2O} : concentration of water

D_{gb} : grain-boundary diffusivity of a component

D_{sd} : lattice diffusivity of a component

E : activation energy

f : force exerted on a dislocation

f_{O_2} : oxygen fugacity

G : shear modulus

H : activation enthalpy

J : flux of a component

k : dislocation annihilation rate constant

K : resistance force during dislocation motion

L : grain size

L_c : dislocation climb distance

L_g : dislocation glide distance

M : direction of dislocation motion

T : length of a dislocation

t : time

T : unit vector tangent to the dislocation

v : individual dislocation velocity

\bar{v} : average dislocation velocity

ΔV : activation volume

$\bar{\sigma}_{ex}$: external stress tensor

$\bar{\sigma}_{in}$: internal stress tensor

ε : strain

η : viscosity

ρ : free dislocation density

τ : resolved stress on a unit length dislocation

Ω : molar volume of atom

1. Introduction to dislocation theory and rheology of the Earth's upper mantle

1.1 Theory of dislocations

1.1.1 Dislocations

The concept of dislocations was first proposed to reconcile theoretical and experimental values of the applied shear stress for plastic deformation. Instead of shearing the bulk of the crystal in one step, macroscopic strains are results of accumulation of micro strains on lattice scales. A dislocation is defined as a line defect that marks a boundary between strained and unstrained areas in a crystal (Fig. 1.1.1a). Sweep of a dislocation through the whole crystal leaves a step on a surface of the crystal and leads to a macroscopic strain (Fig. 1.1.1b).

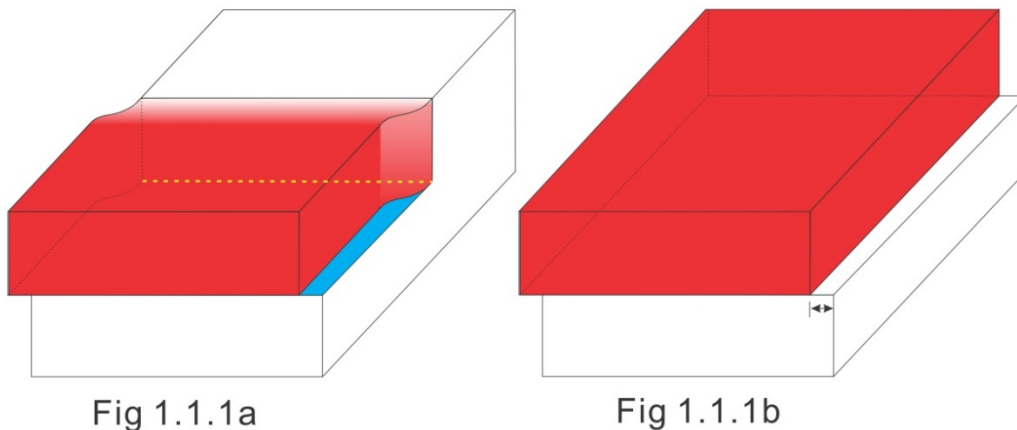


Fig 1.1.1. The red region is displaced relative to the region below. Therefore, the material is deformed. The yellow line marks the boundary between the deformed and undeformed areas in 1.1.1a, defined as the dislocation. In Fig. 1.1.1b, the dislocation line goes through the whole plane and leaves a step at surface, leading to a macroscopic strain.

1.1.1.1 Characterization of dislocations

Dislocations can be visualized using the Volterra construction. Let the lattice shown in the left part of Fig. 1.1.2 be perfect and undeformed. Cut the lattice along any plane indicated in the middle part of the cubes and let the atoms on one side of the cutting plane shift by a vector \mathbf{b} relative to the corresponding atoms on the other side. Then rejoin the atoms on either side of the cutting plane. The new distorted lattice is shown in the right part of the figure. The lattice structure itself is actually almost perfect except near the lines AB. The line defects AB in the lattice are dislocation lines and the region where lattices are strongly distorted is called the dislocation core.

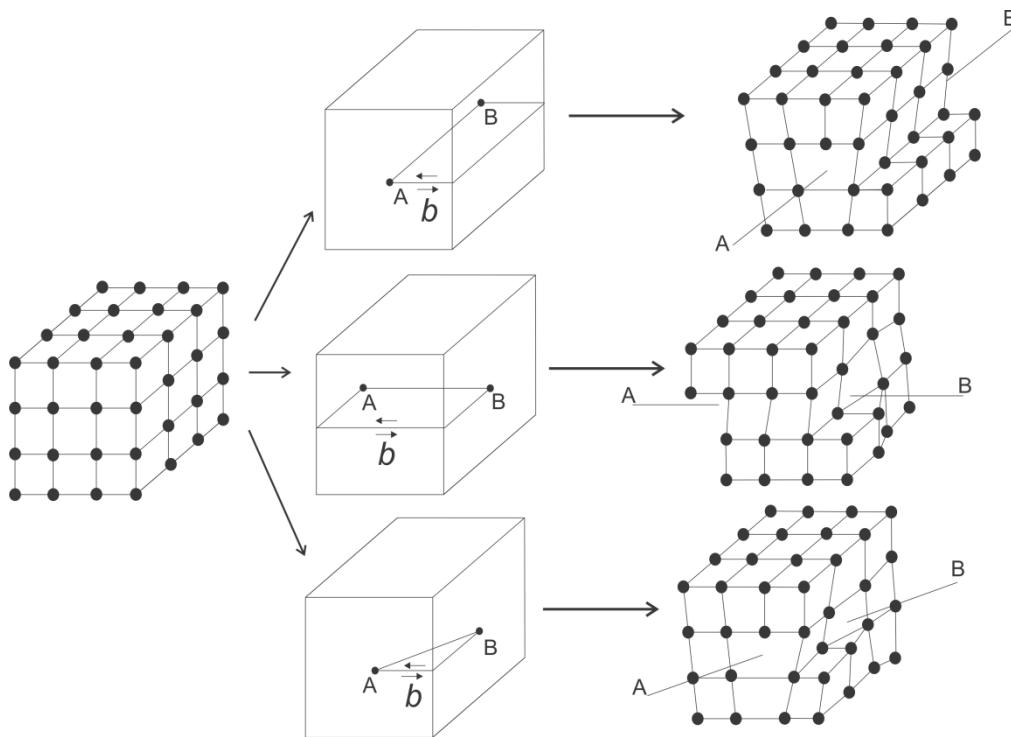


Fig 1.1.2. Dislocations with different characters. The top, middle and bottom cases show edge, screw and mixed dislocations, respectively.

The slip vector \mathbf{b} is called Burger's vector. The plane defined by \mathbf{T} and \mathbf{b} is called slip plane, where \mathbf{T} is a unit vector tangent to the dislocation line. A slip plane and \mathbf{b} consist of a slip system. The upper two figures in Fig. 1.1.2 show two end-member types of dislocation

lines depending on the geometry between T and b . An edge dislocation has b perpendicular to T and a screw has b parallel to T . Dislocations with an in-between structure are called mixed dislocations. An edge dislocation also can be visualized simply by inserting or removing a half plane of atoms into or from the lattice (Fig. 1.1.3). A dislocation has to move in a certain direction (M) on a slip plane in order to produce macroscopic strain. The relationships among b , M and T are summarized in Table 1.1.1.

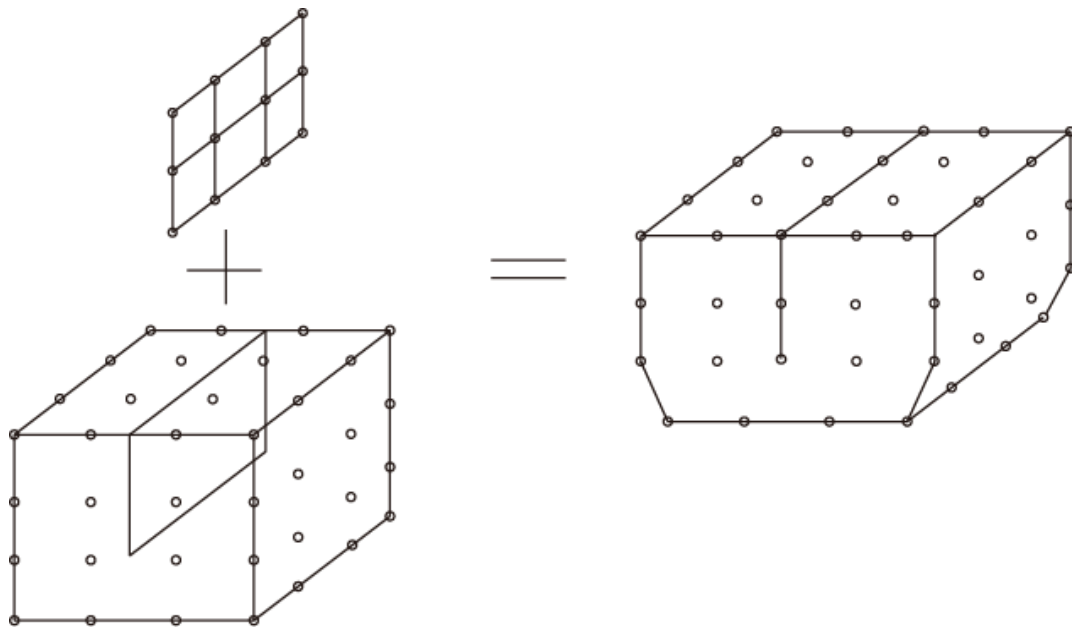


Fig 1.1.3. Schematic image shows that an edge dislocation can be visualized by inserting a lattice plane into a perfect lattice.

Table 1.1.1. Geometry between b , M and T

	b relative to T	M relative to T	b relative to M
Edge	Perpendicular	Perpendicular	Parallel
Screw	Parallel	Perpendicular	Perpendicular

The Burger's vector can also be defined using the Burger's circuit (Fig. 1.1.4). The direction of T is first fixed and a circuit is made around T based on the right-hand rule. Then, the same circuit is transferred to an ideal crystal to obtain a closure failure, which defines the

magnitude and direction of \mathbf{b} . A dislocation whose \mathbf{b} is a unit vector of the crystal structure is called a perfect dislocation. Dislocations otherwise are called partial dislocations. Dislocations are said to be opposite when they have \mathbf{b} in the opposite directions. The physical meaning of opposition can be understood from two aspects. Firstly, opposite dislocations move in opposite directions under the same stress conditions (Fig. 1.1.5a). Secondly opposite dislocations annihilate each other when they meet to leave a perfect crystal structure (Fig. 1.1.5b).

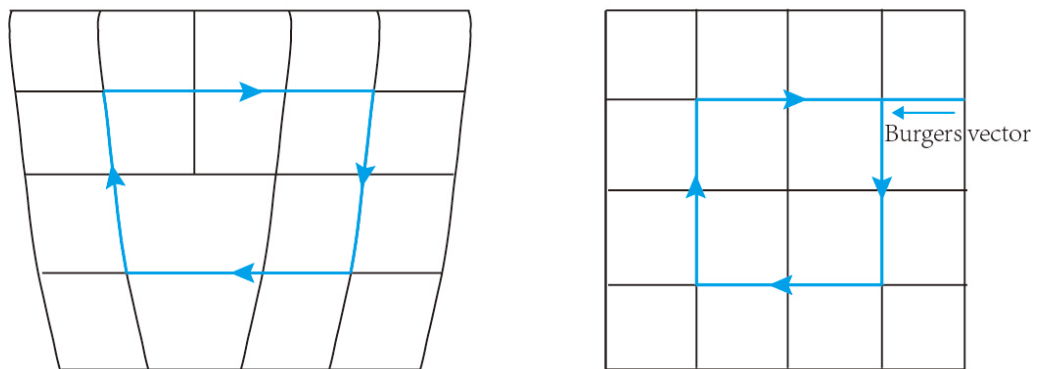


Figure 1.1.4 Construction of Burger's circuit to define an Burger's vector.

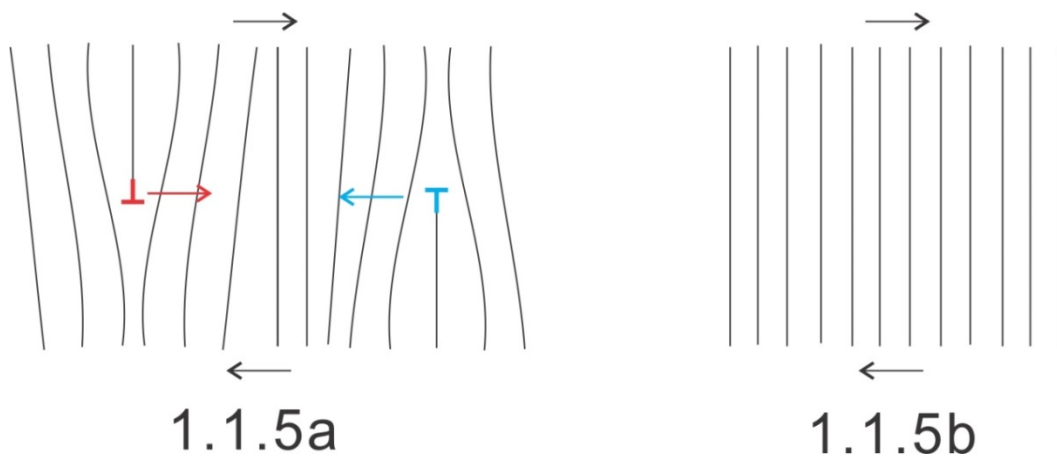


Figure 1.1.5 Physical meaning of opposite dislocations.

1.1.1.2 Movement of dislocations

As stated above, a dislocation can move on its slip plane. This motion is called glide. Glide can happen stepwise by simply breaking and reconfiguring chemical bonds immediately around the dislocation line (Fig. 1.1.6). Therefore, there is no volume change and is called conservative motion. After a dislocation sweeps the whole slip plane, it leaves a step that equals to b at the surface of the crystal (Fig 1.1.1). Both screw and edge dislocations can have glide motion. The only special property with screw dislocations is that it has no unique slip plane because $T // b$ and therefore it can glide on any plane. In order to distinguish the change of slip planes, the glide of a screw dislocation out of its formal slip plane is called cross-slip.

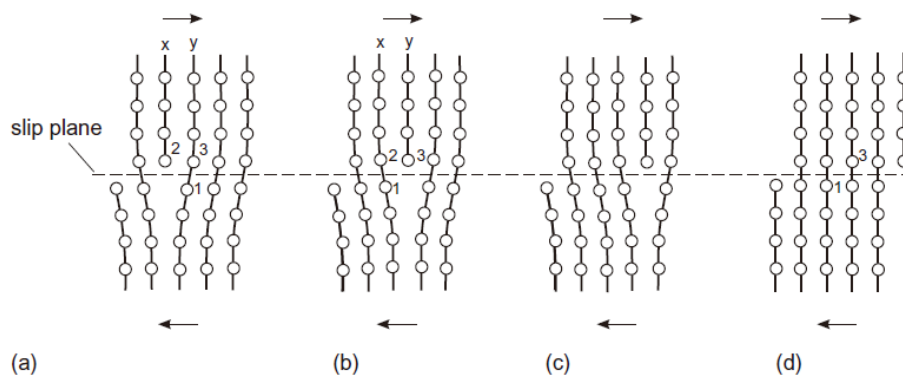


Fig. 1.1.6. Dislocation glide

At low temperatures where diffusion is difficult, movements of dislocations are restricted almost entirely to glide. However, at high temperatures, an edge dislocation can move out of its slip plane by a process called climb (Fig 1.1.7). When a vacancy diffuses to a dislocation line, it moves up by one atom spacing out of its original slip plane (positive climb) and when a vacancy diffuses away from a dislocation line, it moves downward (negative climb). Climb of edge dislocation can be visualized as moving the extra half plane up or down. It clearly causes volume change and therefore, climb is a non-conservative process. Generally, the volume change due to motions of a unit-length dislocation by a distance s is $b \times T \cdot s$.

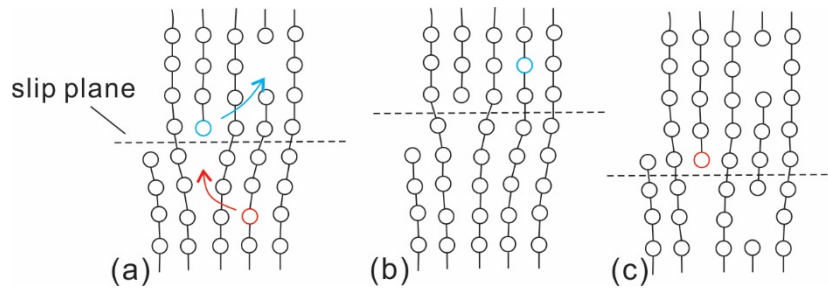


Fig 1.1.7. Positive (b) and negative (c) climb of a dislocation

In practice, not the whole part of a dislocation line glides or climbs during dislocation motions. A step is formed on the dislocation line by bowing out segments of a dislocation line. The step due to the bowing in and out of the slip plane is called a kink and a jog (Fig. 1.1.8), respectively. Lateral motion of kinks and jogs, respectively, brings the dislocation line into the next low-energy position to complete glide and climb of the whole dislocation line. The Burgers vector of kinks and jogs is the same as that of their parental dislocation. Using Table 1.1.1, it is easy to prove that kinks on edge and screw dislocations are of screw and edge character, respectively while jogs on edge and screw dislocations are of edge character. For glide motion, nucleation of kinks serves as a rate-limiting process. The lateral motion of kinks is due to stresses and does not increase the line length of dislocations and therefore not the energy of dislocations (Eq. 1.1.4 in Chapter 1.1.1.3). Hence, the lateral motion of kinks should be relatively quick. For climb motion, the lateral motion of jogs is due to emission or absorption of vacancies to jogs. Thus, jogs are sources and sinks for vacancies. The motion of jogs should be much slower than that of kinks because it is diffusion-controlled. Concentration of jogs in a crystal whose stacking fault energy is high is usually assumed to be one [Kohlstedt, 2006]. In such a case, the climb motion of jogs can serve as a rate-limiting process of dislocation motions.

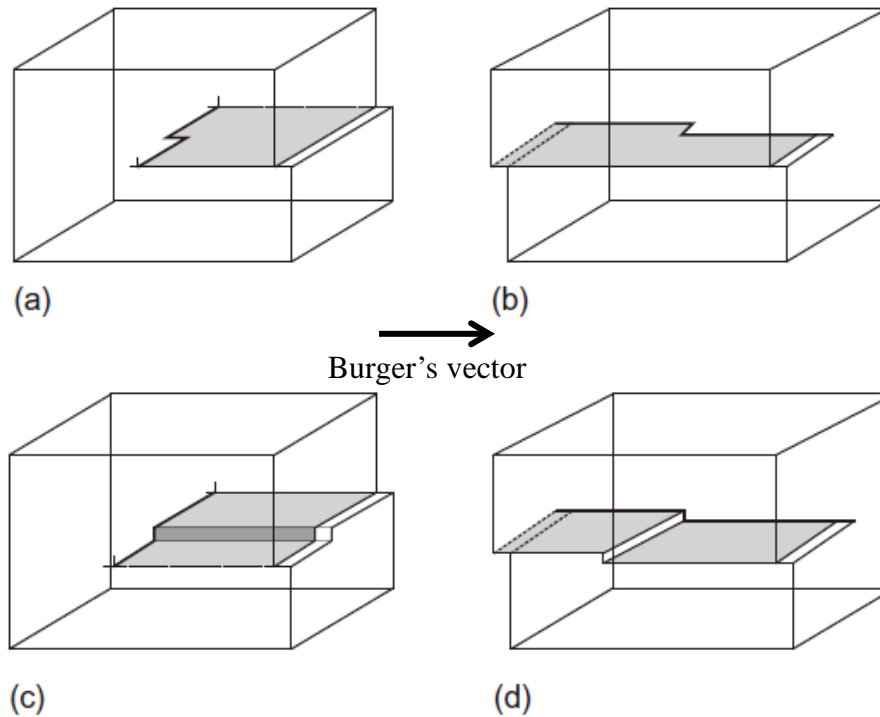


Fig 1.1.8. Kinks (a and b) and jogs (c and d) in edge and screw dislocations (from *Hull and Bacon*, 2011)

1.1.1.3 Force and energy of dislocations

There must be some force (f) that is exerted on dislocations in order to move it. Unlike Newton's second law for macroscopic objects, where force is proportional to the time derivative of velocity (v), force is directly related to velocity itself in microscopic region, i.e

$$v = \bar{\bar{B}}g(f) \quad (1.1.1)$$

$\bar{\bar{B}}$ is the mobility tensor, $g(f)$ is a function of the force. In simple cases, we assume $g(f)$ as the force itself and the equation is usually considered in one dimension. Then Eq. (1.1.1) becomes

$$v = Bf \quad (1.1.2)$$

Therefore, once the force on and mobility of dislocations are known, we can calculate the

velocity of dislocation motions, which is proportional to the strain rate (Chapter 1.1.2)

The force on a unit length of a dislocation is expressed by Peach-Koehler equation [*Peach and Koehler, 1950*]

$$\mathbf{f} = \mathbf{T} \times ((\bar{\sigma}_{ex} + \bar{\sigma}_{in}) \cdot \mathbf{b}) \quad (1.1.3)$$

where $\bar{\sigma}_{ex}$ and $\bar{\sigma}_{in}$ are the stress tensors due to external and internal stresses (caused by other dislocations), respectively. $\bar{\sigma}_{ex}$ is explicitly obtained, and $\bar{\sigma}_{in}$ can be calculated by linear elasticity since the distortion caused by a dislocation is mainly concentrated at dislocation cores and at places far away from cores, the displacements of atoms can be regarded as infinitesimal. Generally, the stress field produced by a dislocation is inverse proportional to the distance from the dislocation [*Hull and Bacon, 2001*].

The existence of strains around a dislocation implies a crystal containing a dislocation is not at its energy minimum state. The strain energy increase due to the introduction of one dislocation in a perfect crystal is called the self-energy of the dislocation (E_{self}). It is composed of energy stored at the dislocation core (E_{core}) and the energy caused by elastic strains at places away from the core ($E_{elastic}$). Since E_{core} is much smaller than $E_{elastic}$, the energy of a dislocation approximates to $E_{elastic}$

$$E_{self} \approx E_{elastic} \propto T G b^2 \quad (1.1.4)$$

where T is length of the dislocation line and G is the shear modulus. From the equation, it can be seen that a dislocation tends to reduce its length and always prefers the shortest Burgers vector to lower the self-energy.

1.1.2 Orowan's equation

Orowan's equation is the most fundamental equation for describing dislocation creep. It is the starting point from which all dislocation creep models are built. It links the microscopic

properties of dislocations and the macroscopic strain rate ($\dot{\epsilon}$) of a crystal

$$\dot{\epsilon} = \rho b \bar{v} \quad (1.1.5)$$

where ρ is the mobile dislocation density. It is defined by the length of mobile dislocations per unit volume. \bar{v} is the average dislocation velocity.

It can be seen from Fig. 1.1.9 that the strain increment is b/H , when one dislocation glides through the slip plane S of a crystal. Therefore, when N dislocations glide through an area ΔS over time Δt , the strain increment is

$$\Delta \epsilon = \frac{b}{H} \sum_{i=1}^N \frac{\Delta S_i}{S} = \frac{b}{H} \sum_{i=1}^N \frac{T_i v_i}{S} \Delta t = b \bar{v} \frac{\sum_{i=1}^N T_i}{SH} \Delta t = b \bar{v} \rho \Delta t \quad (1.1.6)$$

The last equality is from the definition of dislocation density, and the average dislocation velocity \bar{v} is defined by

$$\bar{v} = \frac{\sum T_i v_i}{\sum T_i} \quad (1.1.7)$$

Therefore,

$$\dot{\epsilon} = \frac{\Delta \epsilon}{\Delta t} = \frac{b \bar{v} \rho \Delta t}{\Delta t} = \rho b \bar{v}$$

which is Orowan's equation.

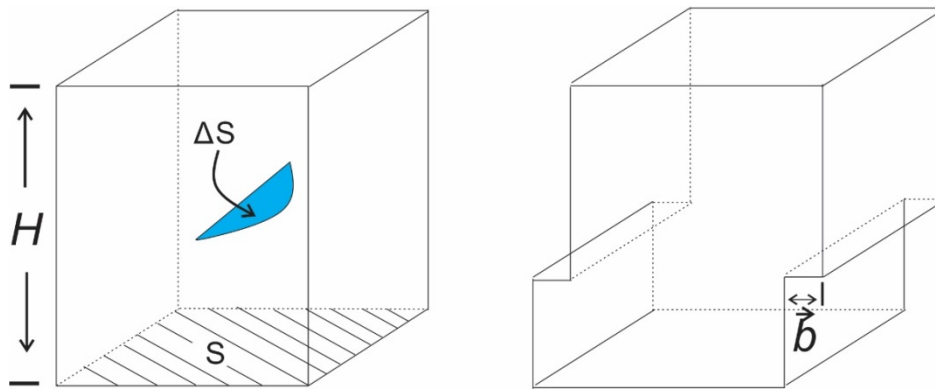


Fig 1.1.9. Glide of a dislocation through the whole slip plane caused a macroscopic strain on the crystal.

Among the parameters in Orowan's equation, b remains nearly constant and ρ is mainly dependent on stress and nearly independent of thermochemical conditions. In contrast, \bar{v} is strongly dependent on thermomechanical conditions. Therefore, the dependence of dislocation creep on thermochemical conditions is controlled by that of dislocation mobility.

1.1.3 Models of dislocation creep

Based on Orowan's equation, a number of models for dislocation creep are proposed. The difference between them is made by different choices of \bar{v} . At low-temperature or in high-stress regimes, the glide velocity represents \bar{v} . At low temperatures, dislocation motions are restricted to glide since thermal energy is not enough for climb to occur. At high stresses, stresses are high enough to help dislocations overcome obstacles that they meet by glide. Therefore, in these two cases, climb is not necessary for dislocation motions. At high temperatures, glide and climb occur in series, and therefore, the velocity of the slowest motion represents \bar{v} . Conventionally, climb is assumed to be the slower one since it needs diffusion. However, if dislocations dissociate, cross-slip of screw dislocations can also be the slower motion [Poirier, 1976].

1.1.3.1 Glide controlled model

This model is suitable for describing low temperature and/or high stress regimes, and the glide velocity represents \bar{v} . Consider a dislocation gliding in the x direction under a total stress τ normal to L . Based on Eq. 1.1.3, the force that exerted on the unit-length dislocation line is τb . During glide from x_1 to x_2 , the dislocation meets an obstacle, which produces a resistance force K on the dislocation line (Fig. 1.1.10), the energy (Helmholtz free energy) to overcome the resistance is

$$\Delta F = \int_{x_1}^{x_2} K dx \quad (1.1.8)$$

Part of this energy can be supplied by the mechanical work done by the stresses, $\tau l b(x_2 - x_1)$, where l is the length of the obstacle. This can be written as τV^* , where V^* is called the activation volume. The remainder of the energy required is the free energy of activation (Gibbs free energy), which is labeled 'thermal' in Fig. 1.1.10a.

$$\Delta G = \Delta F - \tau V^* \quad (1.1.9)$$

The probability where the energy to overcome the obstacle can be supplied by thermal fluctuation at temperature T follows the Boltzmann distribution. Therefore, the number of successful vibrations for a dislocation to overcome an obstacle with vibration frequency ν is $\nu \exp(-\Delta G/kT)$ per second. Thus the glide velocity is

$$v_g = s \nu \exp\left(-\frac{\Delta G}{kT}\right) \quad (1.1.10)$$

where s is the distance of dislocation movement required to overcome the obstacle.

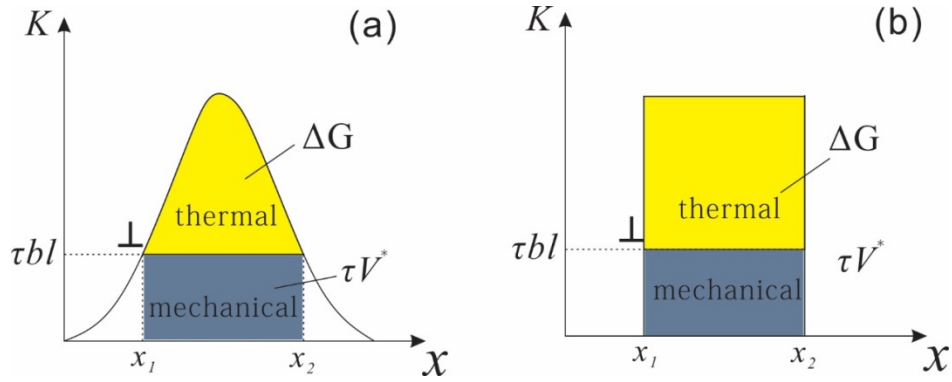


Fig 1.1.10 Profile of resistance force K versus distance x (Modified from *Hull and Bacon*, 2001)

If there is no thermal assistance for dislocation motions, i.e. dislocation glides at $T = 0$, τbl must be equal to the maximum of K . In such a case, τ is called Peierl's stress when K is the lattice resistance.

Suppose that the resistance force is a step function of distance (Fig. 1.1.10b), then

$$\Delta G = \Delta F \left[1 - \frac{\tau(T)}{\tau_{max}} \right] = \Delta F \left[1 - \frac{\tau(T)}{\tau(0)} \right] \quad (1.1.11)$$

In more general situations, this equation is replaced by

$$\Delta G = \Delta F \left[1 - \left(\frac{\tau(T)}{\tau(0)} \right)^p \right]^q \quad (1.1.12)$$

from *Kocks et al.* [1975]. Combine Eq. 1.1.12, Eq. 1.1.10 and Eq. 1.1.5,

$$\dot{\epsilon} = C \rho \exp \left(- \frac{\Delta F}{RT} \left[1 - \left(\frac{\tau(T)}{\tau(0)} \right)^p \right]^q \right) \quad (1.1.13)$$

where C is a constant. The conventional relationship between stress and dislocation density is [*Bailey and Flanagan*, 1967]:

$$\rho \propto \left(\frac{\tau}{Gb}\right)^2 \quad (1.1.14)$$

where G is the shear modulus. The final equation of the glide-controlled model is

$$\dot{\varepsilon} = Ab\left(\frac{\tau}{Gb}\right)^2 \exp\left(-\frac{\Delta F}{RT} \left[1 - \left(\frac{\tau(T)}{\tau(0)}\right)^p\right]^q\right) \quad (1.1.15)$$

where A is a constant.

1.1.3.2 Cross-slip-controlled model

Glide of a screw dislocation out of its formal plane is called cross-slip. Therefore, the equation for cross-slip-controlled model is similar to that of the glide-controlled model. However, when screw dislocations dissociate, partial dislocations have to be recombined in order to cross-slip. This process needs to overcome the stacking fault energy, which is a function of stress [*Poirier and Vergobbi, 1978*] and usually simplified to be a linear function of stress. Therefore, Eq. 1.1.15 is modified to

$$\dot{\varepsilon} = A\left(\frac{\tau}{Bb}\right)^2 \exp\left(-\frac{B-C\tau}{RT}\right) \quad (1.1.16)$$

where B and C are constants.

1.1.3.3 Climb-controlled model

At high temperatures, diffusion occurs, and climb becomes possible for dislocation motions. Since glide and climb occur in series, and climb is usually assumed to be much slower than glide, \bar{v} is usually assumed to be equal to the climb velocity at high temperatures.

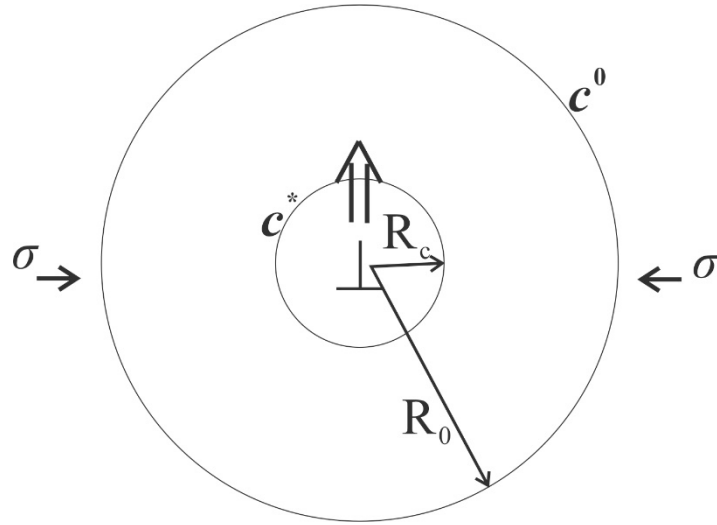


Fig. 1.1.11. Dislocation climbs positively under compression. The vacancy concentration near the dislocation is higher than that far from the dislocation (Modified from *Weertman*, 1999).

The velocity of climb can be calculated from the flux of vacancies to the dislocation. Consider Fig. 1.1.11, compression under stress σ causes a shortening of material in the compression direction, which corresponds to a positive climb. Therefore, the vacancy concentration at the dislocation core (c^*) is higher than the equilibrium value (c^0) at some distance, R_0 , away from the dislocation. If the molar volume of atoms is Ω , the formation energy of the vacancy is modified by $\sigma\Omega$ and the vacancy concentration at the dislocation core is

$$c^* = c_0 \exp\left(-\frac{Q}{RT}\right) \exp\left(\frac{\sigma\Omega}{RT}\right) \quad (1.1.17)$$

which can be approximated as

$$c^* \cong c_0 \exp\left(-\frac{Q}{RT}\right) \left(1 + \frac{\sigma\Omega}{RT}\right) = c^0 \left(1 + \frac{\sigma\Omega}{RT}\right) \quad (1.1.18)$$

at low stress conditions, where Q is the formation energy for the vacancy under no stress

conditions, and $c^0 = c_0 \exp(-\frac{Q}{RT})$. The concentration difference between the dislocation core and equilibrium positions causes a flux of vacancies. Based on Fick's first law

$$J = -D_v \frac{dc}{dr} 2\pi r \quad (1.1.19)$$

where D_v is the diffusivity of vacancy, c is the vacancy concentration and r is the distance from the dislocation. In order to maintain mass conservation, the flux between $r = R_c$ and R_0 must be a constant, i.e.

$$\frac{dc}{dr} 2\pi r = \text{constant} \quad (1.1.20)$$

where R_c is the radius of dislocation core, Solve this equation with the boundary conditions that $c(R_c) = c^*$ and $c(R_0) = c^0$,

$$c = c^0 + (c^* - c^0) \frac{\ln(R_0/r)}{\ln(R_0/R_c)} \quad (1.1.21)$$

Combine Eqs. 1.1.20, 1.1.21 and 1.1.19,

$$J = \frac{2\pi D_v c^0 (\sigma \Omega / RT)}{\ln(R_0/R_c)} \quad (1.1.22)$$

Rewrite this equation with the relationship between diffusivity of vacancy and atom self-diffusion coefficient (D_{sd})

$$D_{sd} = D_v c^0 \Omega \quad (1.1.23)$$

Eq.1.1.22 becomes

$$J = \frac{2\pi D_{sd}(\sigma\Omega/RT)}{\Omega \ln(R_0/R_c)} \quad (1.1.24)$$

The relation between flux and velocity is

$$v = \frac{J\Omega}{d} \quad (1.1.25)$$

where d is the lattice parameter, which can be simplified into the length of Burger's vector, b .

Therefore, the climb velocity is

$$v_c = 2\pi \left(\frac{D_{sd}}{b}\right) \frac{\sigma\Omega/RT}{\ln(R_0/R_c)} \quad (1.1.26)$$

Assuming v_g is much faster than v_c , \bar{v} can be expressed as

$$\bar{v} = \frac{l_g}{l_c} v_c \quad (1.1.27)$$

where l_g and l_c are the glide and climb distances, respectively. Combine Eq. 1.1.5, Eq. 1.1.14, Eq.1.1.26 and Eq. 1.1.27, the equation for the climb-controlled model is

$$\dot{\epsilon} = A \left(\frac{D_{sd}}{b^2}\right) \left(\frac{\sigma}{G}\right)^3 \frac{G\Omega/RT}{\ln(R_0/R_c)} \left(\frac{l_g}{l_c}\right) \quad (1.1.28)$$

where A is a constant.

1.1.4 Other deformation mechanisms

Creep mechanisms other than dislocation creep are diffusion creep and grain boundary sliding. Unlike the grain-size independence of strain rate in dislocation creep, both diffusion

creep and grain boundary sliding are grain-size dependent. Diffusion creep is characterized by the linear dependence of strain rate on stress, which means that the material behaves as a Newtonian fluid. Grain boundary sliding is actually a deformation mechanism intermediate between diffusion and dislocation creep and has some characteristics of both mechanisms.

1.1.4.1 Diffusion creep

Unlike dislocation creep, which is caused by motions of dislocations, diffusion creep results from flux of vacancies that is caused by a vacancy concentration gradient induced by stresses. By the same reasoning as Chapter 1.1.3.3, the vacancy concentration under compression and tension is expressed as:

$$c^* = c^0 \left(1 \pm \frac{\sigma \Omega}{RT} \right) \quad (1.1.29)$$

The plus and minus signs correspond to compress and tension, respectively. Therefore, the vacancy flux goes from tension areas to compression areas (Fig. 1.1.12), resulting in a counter-direction flux of atoms. Depend on whether diffusion is through lattice or grain boundaries, diffusion creep is classified into Nabarro–Herring and Coble creeps, respectively.

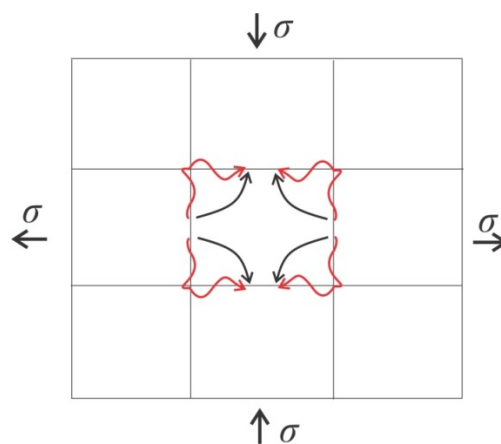


Fig.1.1.12. Crystal deformation by diffusion creep. Vacancies flow from high-stress regions to low-stress regions through the lattice (black) and along grain boundaries (red).

The constitutive equations for Nabarro–Herring and Coble creeps can be deduced by the same reasoning as in Chapter 1.1.3.3. For Nabarro–Herring creep,

$$\dot{\epsilon}_{NH} = \left(\frac{D_{sd}}{L^2}\right)\left(\frac{\sigma\Omega}{RT}\right) \quad (1.1.30)$$

For Coble creep

$$\dot{\epsilon}_{Coble} = \left(\frac{D_{gb}\delta}{L^3}\right)\left(\frac{\sigma\Omega}{RT}\right) \quad (1.1.31)$$

where L is the grain size, D_{gb} is the grain-boundary diffusivity, and δ is the grain boundary width.

1.1.4.2 Grain boundary sliding (GBS)

Grain boundary sliding itself cannot accommodate all strains without deformation of grains (A grain cannot glide relative to another grain infinitely. It has to be stopped by other grains). Therefore, grain-boundary sliding has to be accommodated by either diffusion or dislocation motions inside the grains. The constitutive equation for diffusion accommodated grain boundary sliding is [Poirier, 1985]

$$\dot{\epsilon}_{Dif-GB} = \frac{\alpha}{L^2} D_{sd} \left(1 + \frac{\pi\delta}{\lambda} \frac{D_{gb}}{D_{sd}}\right) \frac{\sigma\Omega}{kT} \quad (1.1.32)$$

where α is a geometry constant and λ is the basic periodicity of grain boundaries. The constitutive equation for dislocation accommodated grain boundary sliding was first systematically investigated by Langdon, 1994. For a large grain size where grains contain subgrains,

$$\dot{\epsilon}_{Dil-GB} = A \frac{D_{sd}Gb}{RT} \left(\frac{b}{L}\right) \left(\frac{\sigma}{G}\right)^3 \quad (1.1.33)$$

and for a small grain size

$$\dot{\epsilon}_{Dil-GB} = B \frac{D_{gb}Gb}{RT} \left(\frac{b}{L}\right)^2 \left(\frac{\sigma}{G}\right)^2 \quad (1.1.34)$$

where A and B are constant.

In summary, constitutive equations for different deformation mechanisms can be generalized into an equation

$$\dot{\epsilon} = A \frac{\sigma^n}{L^p} \exp\left(-\frac{H_{creep}(\sigma,P)}{RT}\right) \quad (1.1.35)$$

where H_{creep} is the activation enthalpy of creep, which is a function of pressure and, depending on the deformation mechanism, stress. Table 1.1.2 summarizes the parameters in equations for different deformation mechanisms.

Table 1.1.2 Summary of different deformation mechanisms

Deformation mechanism		n	p	H
Dislocation creep	Glide model	2	0	$\Delta F \left[1 - \left(\frac{\tau(T)}{\tau(0)} \right)^p \right]^q$
	Cross-slip model	2	0	$B - C\tau$
	climb model	3	0	H for diffusion creep
Diffusion creep	Nabarro–Herring creep	1	2	H of diffusivity of slowest species
	Coble creep	1	3	H of grain boundary diffusivity
Grain boundary sliding	Diffusion accommodated	1	2	Combination of NH and coble creep
	Dislocation accommodated (large grain size)	3	1	H for NH creep
	Dislocation accommodated (small grain size)	2	2	H for coble creep

1.2 Earth's upper mantle rheology

Tectonics indicates that the Earth's mantle, or at least some part of it, is plastically deformed. To understand the mantle rheology, it is important to know the mantle viscosity and the direction of mantle flow. Viscosity of the mantle can be estimated from various geophysical observations, and the direction of mantle flow can be estimated from the knowledge of seismic anisotropy and crystal preferred orientation (CPO)

1.2.1 Viscosity estimation of the upper mantle

One method of estimating the viscosity of the mantle is based on seismic wave attenuation. Seismic wave attenuation is characterized by a Q factor which measures the energy loss during wave propagation. In many cases, attenuation involves thermally activated process and Q^{-1} obeys an Arrhenius equation [e.g. *Gueguen et al.*, 1989; *Jackson et al.*, 2002]

$$Q^{-1} \propto \omega^{-\beta} \exp\left(-\frac{\beta E}{RT}\right) \quad (1.2.1)$$

where β is constant, ω is frequency and E is the activation energy. For olivine, β is 0.2 and E is 440 kJ/mol [*Gueguen et al.*, 1989]. By definition of effective viscosity $\eta = \sigma/2\dot{\epsilon}$ and using Eq. 1.1.35, at constant strain rate

$$\eta \propto \exp\left(\frac{H_{creep}}{nRT}\right) \quad (1.2.2)$$

Combing Eq.1.2.1 and 1.2.2,

$$\log\left(\frac{Q^{-1}/Q_0^{-1}}{\eta/\eta_0}\right) = -n\beta \frac{E}{H_{creep}} \quad (1.2.3)$$

where Q_0^{-1} and η_0 are the seismic wave attenuation and effective viscosity at a reference state.

The similar equation can be obtained at constant stress

$$\log\left(\frac{Q^{-1}/Q_0^{-1}}{\eta/\eta_0}\right) = -\beta \frac{E}{H_{creep}} \quad (1.2.4)$$

The ratio of E and H_{creep} can be regarded as a constant for certain minerals. For olivine, this ratio is 0.8 based on experiments [e.g. *Gueguen et al.*, 1989; *Hirth and Kohlstedt*, 2003; *Jackson et al.*, 2002]. Eq. 1.2.2 and 1.2.3 suggest logarithmic viscosity is inversely proportional to the logarithmic Q . Therefore, the mantle viscosity can be estimated from Q to some extent.

Fig 1.2.1 shows models of Q compiled by *Lawrence and Wysession* [2006]. It indicates a rigid lithosphere (high Q) above a soft asthenosphere (low Q). Below that, Q decreases and therefore, η increases gradually with depth in Earth's upper mantle.

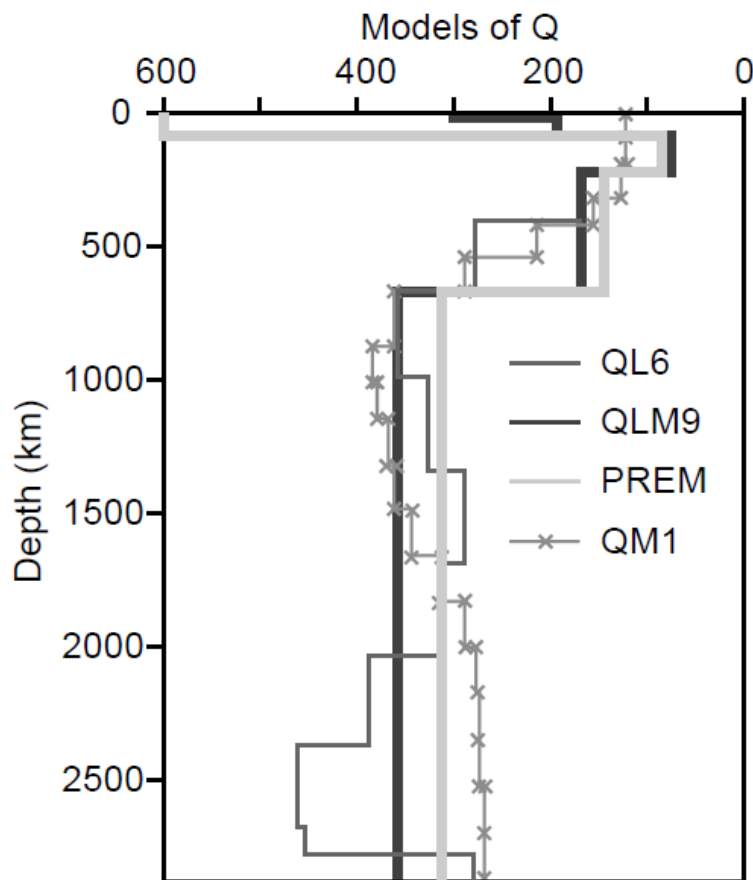


Fig 1.2.1. Q factor for different models. Modified from Lawrence and Wysession (2006).

Another way to estimate mantle viscosity is based on post-glacial rebound. It measures the crustal motions due to the melting of ice sheets. It can give the absolute value of mantle viscosity but the result depends on the pre-assumed viscosity structure in the Earth's mantle. The average viscosity is 3×10^{21} Pa s by assuming that mantle viscosity does not change with depth [Haskell, 1937]. In addition, the rebound results in a change of moment of inertia of Earth, which can be detected by monitoring changes of Earth rotation. These data can be used to evaluate the viscosity of the deep mantle and gave the viscosity of $\sim 10^{22}$ Pa s for deep mantle [e.g. Yuen *et al.*, 1982].

Viscosity of the mantle can also be estimated from geoid anomalies, or dynamic topography. Geoid anomalies are not only caused by density anomalies itself inside the earth but also by the position of the density anomalies. The stresses caused by mantle flow deflect density boundaries and therefore influence the geoid anomalies (Fig. 1.2.2). By changing the pre-assumed viscosity structures of the Earth mantle and combining with the information of density anomalies obtained by seismic studies, one can calculate geoid anomalies and compare them with the measured ones until the assumed viscosity structures best reproduce the observed one. It is clear that only the viscosity contrast between different viscosity layers can be obtained by such studies. This method suggests a significant increase of viscosity from upper to lower mantle [e.g. Hager, 1984].

The one-dimensional viscosity-depth profile is shown in Fig. 1.2.3.

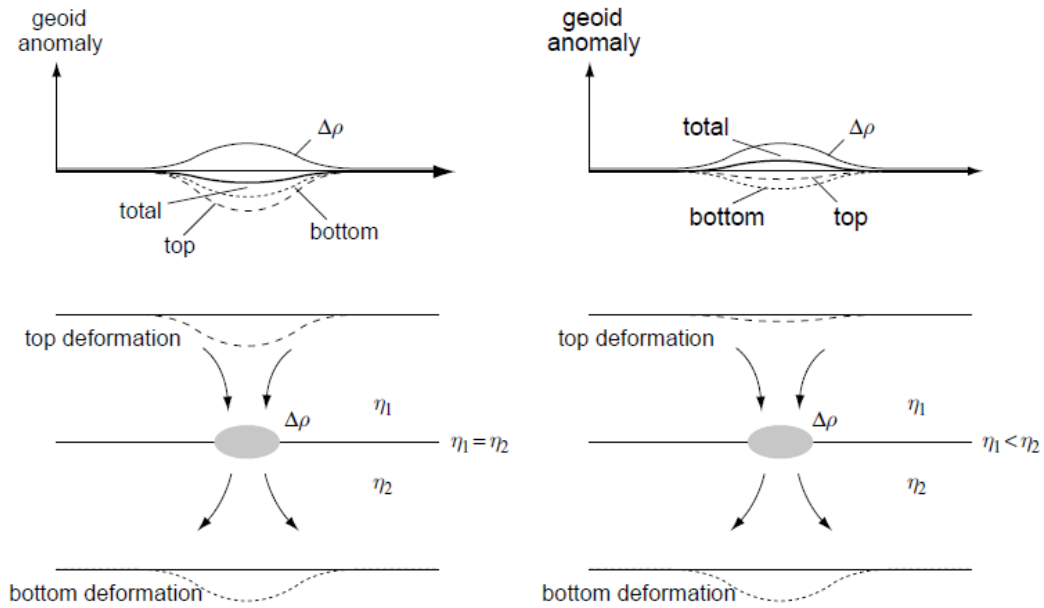


Fig 1.2.2 Schematic diagram which shows the gravity anomalies are not only caused by density anomalies but also by the rheological structure of the investigated region. Depending on viscosity contrast between two layers, the anomalies can be negative (left) or positive (right). From *Karato*, 2012, after Hager, 1984.

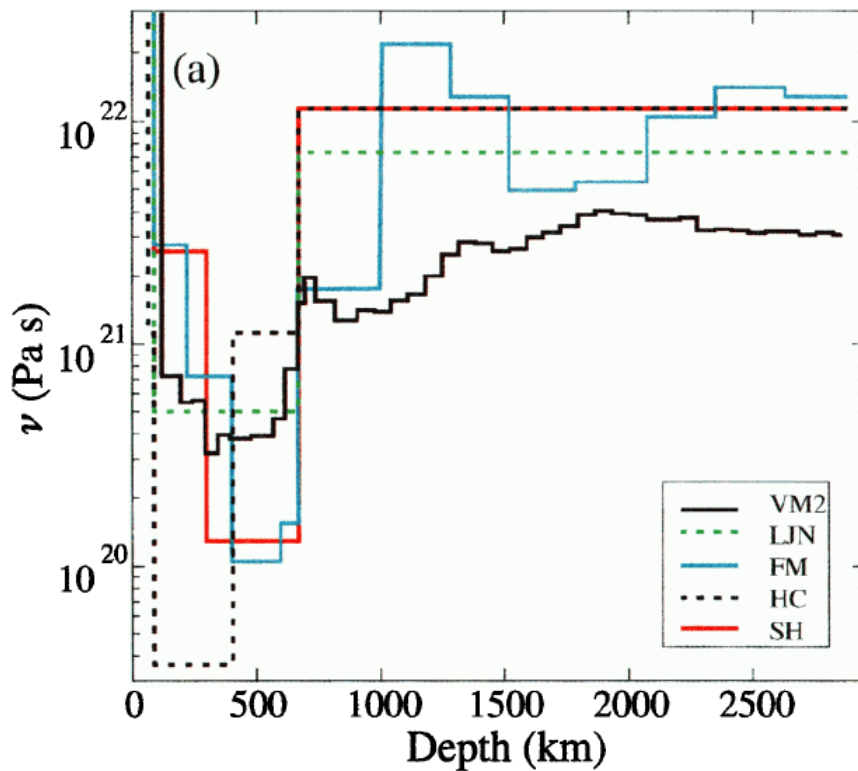


Fig 1.2.3 One-dimensional viscosity-depth profile compiled by *Peltier*, 1998.

1.2.2 Seismic anisotropy in the upper mantle

Velocity of seismic waves depends not only on material that they pass through but also on the propagation and polarization directions. Seismic anisotropy reflects the anisotropy of the elastic properties of rocks, which originate in the stress field of rock deformation. Therefore, it can provide information regarding mantle flow directions.

When seismic waves propagate in different directions, their velocities can be different. This is called azimuthal anisotropy. Both body and surface waves show this kind of anisotropy. It is measured by pairs of sources and receivers that are located on different ray paths through the same target region. It is apparently limited by the number and configurations of seismic stations. In addition, a main shortcoming of this method is that measured anisotropies may come from regions outside the target region but are located on a ray path of the seismic wave.

Polarization anisotropy reflects the dependence of seismic velocity on the polarization direction of S waves. When a S wave passes through an anisotropic region, it decomposes into horizontally polarized (SH) and vertically polarized (SV) waves. This phenomenon is called shear wave splitting. SV and SH arrive at the seismic station at different times since SH and SV have different velocities. This time difference is determined by the thickness of the anisotropic layer and the extent of anisotropy of the layer. One advantage of this method is that the anisotropy can be obtained by a single station, in principle. Like azimuthal anisotropy, however, the location of anisotropy is unclear. There are some methods to constrain the region of anisotropy. For example, one can use S waves formed by P-to-S wave conversion at a discontinuity, whose wave splitting must occur in the region above the discontinuity.

Radial models of the Earth's seismic anisotropy suggested that $V_{SH} > V_{SV}$ in shallow regions of the upper mantle, but this anisotropy becomes weaker with depth, and $V_{SV} > V_{SH}$ at the bottom of upper mantle [e.g. *Dziewonski and Anderson*, 1981; *Gung et al.*, 2003; *Mainprice et al.*, 2000; *Montagner and Kennett*, 1996]. In addition, regional seismic studies suggest that the direction of the faster shear wave is trench-parallel near trenches, while it becomes

perpendicular to the trench away from trenches [e.g. *Nakajima and Hasegawa, 2004*]

1.2.3 Dislocation creep, crystallographic preferred orientation (CPO), mantle flow and seismic anisotropy

Mantle forming minerals are elastically anisotropic and are necessary to explain seismic anisotropy. However, if minerals are randomly distributed in the mantle, the overall properties will be isotropic. Thus, there must be preferred orientations of crystals or fabrics in mantle rocks if seismic anisotropy is observed.

Fabrics originate by different deformation mechanisms. In the case of diffusion creep, there is no gap among grains inside an aggregate since the only constraint for this mechanism is the stress field which must be a continuous function in space. If there was a gap, the stress field there is zero and material would flow to the gap and fill it. Therefore, no grain rotation is needed to accommodate strains and the crystallographic orientations of grains would remain unchanged after deformation. It is noted, however, that grains would have a shape-preferred orientation (SPO). SPO makes little contribution to the seismic anisotropy but can indicate the stress field that grains experienced. On the other hand, gaps should form among grains in the case of dislocation creep, because grains are constrained to deform in slip directions on a slip plane, which are different among neighboring grains. Grain rotations are necessary to fill the gaps (Fig 1.2.4). Therefore, grains would show not only SPO but also crystallographic preferred orientation (CPO) when dislocation creep occurs. Generally, slip directions prefer to align to flow directions. Slip planes prefer to align to the flow plane if they are planar flows. CPO is the main cause of seismic anisotropy

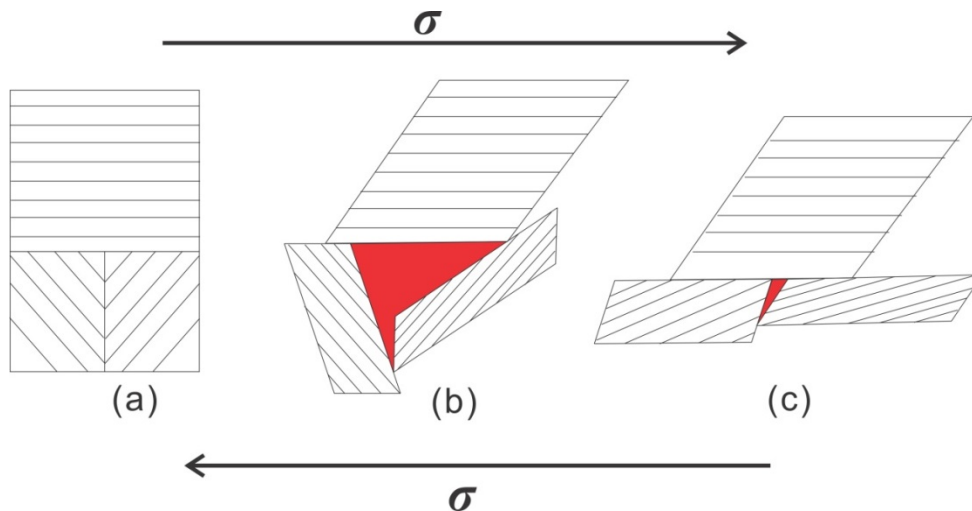


Fig 1.2.4 Grain rotation during dislocation creep. The black lines in each grain indicate slip planes. A gap (red region) forms due to the deformation of individual grains constrained by their slip systems (b). Grains need rotation to reduce the gap (c). Finally, the slip directions and planes in grains prefer to be parallel to the shear direction and shear plane, respectively.

From the above discussion, it is clear that parameters that influence dislocation creep also influence the formation of CPO. Therefore, both stress and thermochemical conditions are important for the development of CPO. The stress fields in the mantle are controlled by the directions and velocity gradients in mantle flow. Once we know the relations between CPO, stress fields and thermochemical conditions, we can use CPO to estimate the geometry of mantle flow. On the other hand, we can estimate mantle thermochemical conditions if we know the geometry of a mantle flow. The relationships among slip systems, CPO and seismic anisotropy are summarized in Fig. 1.2.5.

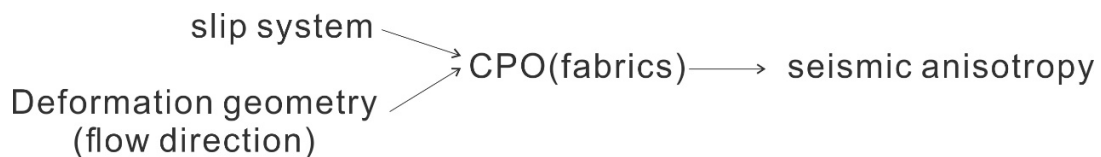


Fig 1.2.5 Diagram shows the relationships among slip system, CPO, and seismic anisotropy.

CPOs developed at different conditions can be investigated from natural samples.

Lineation and foliation are used to estimate the stress fields experienced by natural samples. Distributions of crystallographic axes can be determined by the electron backscatter diffraction (EBSD) method. CPOs of natural olivines are summarized at Table 1.2.1. Relations between thermomechanical conditions and CPOs can also be studied by deformation experiments (Chapter 1.5.1). Whether the listed slip systems actually occur or not have to be determined by TEM. Unfortunately, a limited number of samples with fabrics found in nature have been examined by TEM

Table 1.2.1 CPOs of natural olivine

Name	Lineation direction	Foliation plane	Supposed slip system*
A-type	[100]	(010)	[100](010)
B-type	[001]	(010)	(001)(010)
C-type	[001]	(100)	[001](100)
D-type	[100]	<i>0kl</i>	[100] <i>0kl</i>
E-type	[100]	(001)	[100](001)
AG-type	<i>hOl</i>	(010)	[100](010)+[001](010)

* These are based on the hypothesis that a dominant slip system determines the fabric.

1.3 Mineralogical models of the Earth's mantle

One commonly accepted composition of the Earth's mantle is the pyrolite composition [Ringwood, 1975]. It is a mixture of mid-ocean ridge basalt and peridotite, since it is considered that the former forms by partial melting of the upper-mantle materials and the latter is the residue of partial melting. The mineralogical assemblages in the pyrolite model as a function of depth are shown in Fig. 1.3.1. They are obtained from high-pressure high-temperature experiments. Olivine ($(\text{Mg,Fe})_2\text{SiO}_4$) occupies 60% by volume of the upper mantle. The polymorphs of olivine, namely wadsleyite and ringwoodite, are the dominant minerals in the transition zone. The low mantle mainly consists of bridgemanite. The phase

transitions of olivine into wadsleyite and of ringwoodite into bridgemanite plus ferropericlase in this model correspond to the 410 km and 660 km seismic discontinuities quite well. This model assumes that there is no chemical stratification in the whole mantle, implying whole mantle convection.

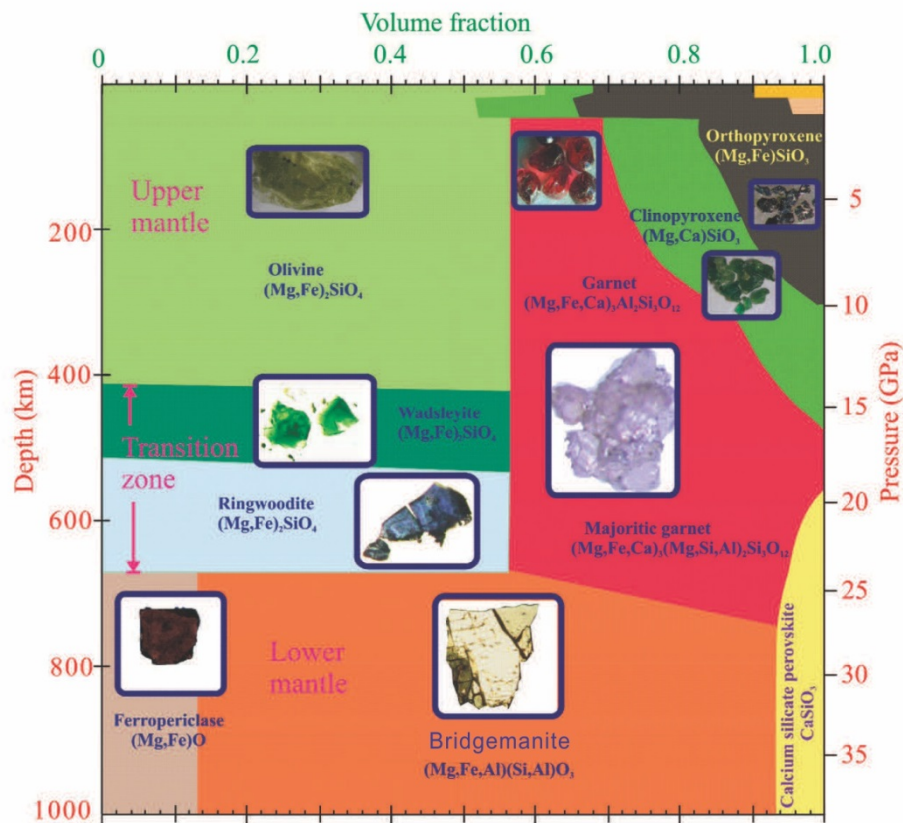


Fig 1.3.1 Pyrolite model of the Earth mantle (modified from *Frost, 2008*)

Another commonly used model for the bulk Earth's composition is the so-called chondrite model. It assumes that the abundances of refractory elements of the bulk Earth are the same as those of type I carbonaceous chondrite (CI chondrite). This assumption is based on the abundances of refractory elements in CI chondrite being the same as those found in the Sun's convective layer, which are estimated from optical spectroscopy. This agreement indicates that the composition of CI chondrite can represent that of a primordial solar system. Under the assumption that the Earth is a product of accretion of materials in a primitive solar system, the CI composition can be a good candidate for the bulk Earth. There is more SiO_2

and less MgO contents in the CI composition compared with those in the pyrolite model. Therefore, this model may indicate layered mantle convection and compositional stratification.

1.4 Experimental techniques to study the upper mantle rheology

The rheology properties of the Earth's upper mantle can be studied through experiments in the laboratory on the Earth forming minerals and then extrapolating results to the Earth mantle conditions. Deformation experiments give direct results on constitutive equations but the stress difference between experimental and mantle conditions may cause a problem during extrapolation. Diffusion experiments focus on the diffusivity of the slowest species in the mineral and link the diffusivity and strain rate by different models mentioned in Chapter 1.1.3 and 1.1.4. Therefore, it can only provide indirect information on the rheological properties of minerals. Dislocation recovery experiments study the dislocation mobility by annealing a pre-deformed sample. It can only be employed to study the dependence of dislocation mobility on thermochemical conditions and cannot give final constitutive equations.

1.4.1 Deformation techniques

In deformation experiments, stresses and strains during deformation must be recorded very accurate. Strains can be determined by measuring displacements of a piston relative to the fixed position of the apparatus or using X-ray imaging to monitor a strain marker in situ. Stresses are determined by various types of force transducers (loading cell) or by X-ray diffraction [*Singh, 1993*]

The easiest way to supply a stress to a sample is dead weight loading in which a mass is put on the top of the sample [e.g. *Kohlstedt and Goetze, 1974*]. The stress is by definition $\sigma = mg/A$, where m is the mass of the loading, g is acceleration due to gravity, A is the sectional

area of the loading. The stress supplied by this method is accurate but the magnitude of stress is limited. In addition, this method is only feasible at room pressure.

The Paterson apparatus [Paterson, 1970] is a deformation apparatus that can generate a deviatoric stress in a gas confining environment. This equipment can be fitted with either a standard axial deformation piston for pure shear deformation or a torsion actuator for simple shear deformation. However, the confining pressure is limited to 0.5 GPa.

The Griggs-type apparatus is a modified piston cylinder high pressure deformation apparatus. It deforms a sample in a soft pressure media (salt or molten salt). The stress is provided by advancing a piston which is close to the sample. The confining pressure is limited to 3 GPa.

Some apparatus were developed to achieve deformation at high pressures and high temperatures. Deformation DIA (D-DIA) [Wang *et al.*, 2003] can deform a sample up to 20 GPa [Kawazoe *et al.*, 2011; Kawazoe *et al.*, 2010]. Compared with the traditional DIA press, two opposing anvils in this apparatus can move independently and therefore deform the sample at constrained strain rate. The other type of the apparatus is the rotational Drickamer apparatus (RDA) [Yamazaki and Karato, 2001]. The stress is provided by rotating one of its anvils and the pressure can be up to 55 GPa by using sinter diamond anvils [Nishiyama *et al.*, 2010].

The deviatoric stress can also be generated by squeezing a sample in an anisotropic way. For example, Bussod *et al.* [1993] developed a way to deform samples in Kawai type multi-anvils. Samples were sandwiched between two alumina pistons which were cut at an angle of 45° for simple shear deformation. Similarly, the axial compression in a diamond anvil cell can be employed to generate deviatoric stress [e.g. Kinsland and Bassett, 1977].

The main problem in deformation experiments is the strain rates (and therefore stresses) are much higher than those in natural conditions. Although using the Paterson/Griggs apparatus can achieve low stresses, confining pressures are limited in these apparatus. The differences in strain rates between laboratory and natural conditions may lead to a transition in deformation mechanisms, which may bias the understandings of the mantle rheology.

This is demonstrated by Fig 1.4.1. At low-stress conditions, when a dislocation meets an obstacle, it absorbs a vacancy and moves out of the slip plane to overcome obstacle. This is called the climb-controlled mechanism. It involves diffusion because the dislocation needs to absorb a vacancy to climb. In the other hand, at high-stress conditions, the dislocation can directly pass the obstacle. This is called the glide-controlled mechanism and does not involve diffusion.

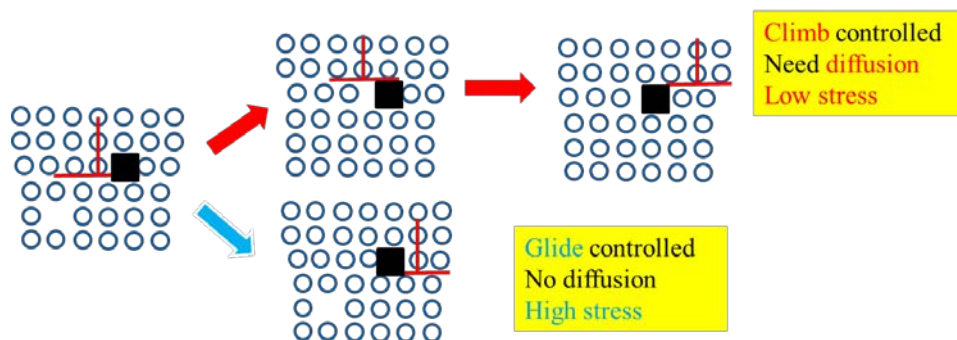


Fig 1.4.1 Dislocation motions controlled by different mechanisms at different stresses conditions

1.4.2 Diffusion techniques

Diffusion experiments can be used to measure the diffusivity of the slowest species in minerals and the validity of applications of results in these experiments into rheology depends on the rheological model that summarized in Chapter 1.1.3 and 1.1.4. In diffusion experiments, a layer with a different isotopic composition, called a diffusion source, is placed on a mineral sample with an otherwise similar composition. This couple is then annealed at target conditions and the isotope composition changes during annealing due to self-diffusion. The diffusion profile of the isotope is determined after annealing and the diffusivity is fitted. The diffusivity is then plugged into appropriate equations listed in Chapter 1.1.3 and 1.1.4 to get the constitutive equations for different deformation mechanisms. Since there is no need to generate deviatoric stresses, such experiments are usually done at hydrostatic conditions and

can provide a much wider range of experiment conditions than that in deformation experiments. However, there are certain differences between diffusion and creep processes. Firstly, the defects involved in these two processes are not always the same. For example, diffusion does not involve dislocations. Secondly, although self-diffusivity of the slowest species is assumed to represent the rate-limiting process during creep, deformation can only occur when the whole unit cell transfers. Therefore, coupled diffusion of the slowest and the fastest species may be important [Jaoul, 1990]. In summary, results from diffusion experiments can only give indirect information on rheology.

1.4.3 Dislocation recovery techniques

Dislocation recovery is one experimental technique to estimate dislocation mobility. In this technique, a sample is first deformed to generate dislocations of a certain type and is then annealed under hydrostatic conditions. Dislocations in the sample move due to internal stresses and dislocations with different signs annihilate with each other, causing a reduction in dislocation density at a rate proportional to the dislocation density, ρ , square, i.e.

$$\frac{d\rho}{dt} = k\rho^2 \quad (1.4.1)$$

where k is the rate constant. By integrating this equation,

$$k = \left(\frac{1}{\rho_f} - \frac{1}{\rho_i}\right)/t \quad (1.4.2)$$

where ρ_i and ρ_f are dislocation densities before and after annealing, respectively, t is the annealing time.

The primary advantage of this technique is that no external stresses, which are many orders of magnitude higher in deformation experiments than in natural conditions, are applied. Hence, the physical environments in annealing experiments are more representative of the

mantle than those in the deformation experiments. In addition, the rate constants are independent of internal stresses [Karato and Ogawa, 1982]. Therefore, the rate constants are not biased by different initial dislocation densities and can be used to represent mobility of dislocations (Eq. 1.1.1). Another advantage of this method is that it allows a much wider range of physical and chemical conditions than those in deformation experiments, making it possible, for example, to precisely determine the dependence of recovery on thermochemical conditions. Strictly speaking, the rate constant is not identical to the dislocation velocity in dislocation creep since we lack the information about the force that corresponds to this mobility (Eq. 1.1.1). However, the rate constant gives the information about the rate-limiting process of dislocation motions since all kinds of motions of dislocations occur during recovery. Moreover, the dependence of dislocation creep and the rate constant on thermochemical conditions are identical as stated in chapter 1.1.2.

The main disadvantage for this method is that it cannot give the strain rate that is caused by dislocation motions. This is because the proportional constant between the dislocation velocity and the mobility is unknown from experiments and is strongly dependent on the distribution of dislocations. For example, the dislocation reduction rate must be quite different in Fig 1.4.2 a and b even we assume each individual dislocation has the same velocity. Therefore, to direct link the reduction rate and velocity is problematic. Thus, direct comparisons of results in recovery experiments and those from deformation experiments or diffusion experiments are not appropriate. Only information about strain rate dependence on thermochemical conditions can be correctly obtained by this method.

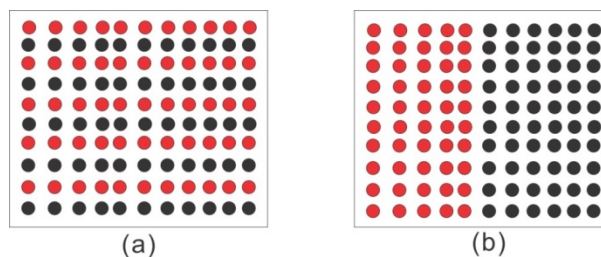


Fig 1.4.2 Two extreme cases for dislocation distribution in two otherwise identical crystals a and b. Red and black circles represent dislocations with different signs.

1.5 Previous studies on rheological properties of olivine

1.5.1 Deformation experiments

The constitutive equation of olivine creep at high temperatures is usually written as follows

$$\dot{\epsilon} = A \frac{\sigma^n}{L^p} f_{O_2}^m C_{H_2O}^r \exp\left(-\frac{E+P\Delta V}{RT}\right) \quad (1.5.1)$$

where E and ΔV are the activation energy and volume, respectively. They reflect the temperature and pressure dependence of creep. The effects of water and oxygen fugacity are reflected through the exponents r and m . There are many deformation experiments that focused on different deformation mechanisms. The values of parameters in the constitutive equation are summarized in Table 1.5.1. It is clear that from the equation 1.5.1 and the discussions in chapter 1.1.3, the climb model is assumed for dislocation creep by previous studies.

Table 1.5.1 Parameters in Eq 1.5.1 from previous deformation experiments

Mechanism*	n	p	r	E (kJ/mol)	ΔV (cm ³ /mol)
Dry diffusion*	1	3	0	375 ± 50	2 - 10
Wet diffusion*	1	3	0.7 - 1	375 ± 75	0 - 20
Dry dislocation*	3.5 ± 0.3	0	0	530 ± 40	1 - 27
Wet dislocation*	3.5 ± 0.3	0	1.2 ± 0.4	520 ± 40	22 ± 11
Dry GBS**	3	0.7 - 1	1.2	420 - 460	17.6 ± 0.8

* From *Hirth and Kohlstedt, 2003*

**From *Hansen et al., 2011* and *Ohuchi et al., 2015*

1.5.1.1 Stress and grain size dependence

These two parameters are keys to identify the deformation mechanism. However, determination of the grain-size exponent p is quite inaccurate. Firstly, the range of grain sizes in deformation experiments is limited, usually a factor of 2 to 3 [Mei and Kohlstedt, 2000a; Mei and Kohlstedt, 2000b]. Secondly, obtaining actual grain sizes is difficult, and different measurement methods render different results [Hansen *et al.*, 2011]. The inaccuracy of p would directly bias the fitted stress exponent n , since n is usually obtained with fixed p .

Judging from values of p and n given in literature, diffusion creep is controlled by grain boundary diffusion, namely it is Coble creep. Therefore, the activation energy of diffusion creep should correspond to that of grain boundary diffusion.

It is noted that the reported stress exponents of dislocation creep of olivine are not 3 as suggested by Eq. 1.1.28 but approximately 3.5. One explanation is that the diffusion process involved in dislocation climb is not lattice diffusion but diffusion through dislocation cores (pipe diffusion) [Hirth and Kohlstedt, 2015]. However, there is a discrepancy in the activation energies between deformation and pipe diffusion. The activation energy of pipe diffusion can be regarded as one half to two thirds that required for lattice diffusion [Shewmon, 2016], which renders a value of 265 – 353 kJ/mol, using the activation energy of lattice diffusion as 529 ± 41 kJ/mol from [Dohmen *et al.*, 2002]. This value is much lower than that in deformation experiments used in Hirth and Kohlstedt [2015] (449 ± 7 kJ/mol).

Another contradiction rises from the values in grain boundary sliding (GBS). Judging from p and n , GBS should be accommodated by dislocation creep. However, n for dislocation creep should be 3.5 based on deformation experiments. It is unreasonable that dislocation motions in dislocation creep regime and GBS regime are controlled by different mechanisms, namely, pipe diffusion and lattice diffusion, respectively. Therefore, either n in GBS or in dislocation creep must be wrongly determined.

1.5.1.2 Activation energy

Reported activation energies of olivine creep rate are listed in table 1.5.1.1, which were obtained at constant oxidation conditions. It is noted that diffusion creep has a lower activation energy (325~450 kJ/mol) in comparison with dislocation creep (480~570 kJ/mol). This fact can be explained by assuming that diffusion creep is controlled by grain boundary diffusion. If so, dislocation creep is not controlled by grain boundary diffusion of Si. Therefore, lattice diffusion and pipe diffusion of Si are two candidates for the rate-limiting process in dislocation creep.

Keefner et al. [2011] measured the activation energy of dislocation creep at constant oxygen fugacity to find 449 ± 7 kJ/mol. They concluded that the apparently high activation energies in previous deformation studies was caused by a change in oxygen fugacity at different T conditions. The oxygen fugacity exponent, m , of dislocation creep obtained in their study was 1/5.

The effect of water on activation energy seems negligible judging from table 1.5.1.1. However, this may be due to fitting data to a wrong equation (see the effect of water chapter). The effect of iron on activation energy is also negligible within the experimental errors [*Durham and Goetze*, 1977; *Ricoult and Kohlstedt*, 1985].

The activation energy of GBS lies between those of dislocation creep and diffusion creep, indicating that, although both lattice and grain boundary diffusion occur in GBS, neither of them dominates as a rate-limiting process. This contradicts with similarity of n and p values of GBS to those of dislocation creep rather than those of diffusion creep, which implies the dominance of dislocation creep in GBS.

1.5.1.3 Activation volume

Activation volume is poorly constrained by deformation experiments, with values ranging from 1 to 30 cm³/mol. The main reason for this inconsistency is due to difficulties to obtain precise relations of stress and strain rate at high pressure. In deformation apparatus in which

stresses are estimated by loads on the pistons that produce deformation, piston loads increase with pressure due to friction, which biases estimation of stresses applied to samples. In deformation apparatus in which stresses are measured by X-ray diffraction, uncertainty of stress estimation is huge, which prevents meaningful determination of activation volume. Very high stress conditions in high-pressure deformation apparatus may lead to different deformation mechanisms in deformation apparatus from in nature. For example, different slip systems may have different activation volumes [e.g. *Raterron et al.*, 2009]. Therefore, the apparent activation volume may have no physical meaning. Besides, the activation volume itself may change with pressure [*Hirth and Kohlstedt*, 2003]. Table 1.5.2 summarizes the activation volumes obtained by different studies. The uncertainties on ΔV render a large variation of the estimated mantle viscosity. For example, ΔV of 1 and 15 cm³/mol would lead to a change of 4 orders of magnitude of the estimated mantle viscosity at depths from 100 to 400 km.

Table 1.5.2 Activation volumes of olivine creep

Sample	ΔV (cm ³ /mol)	P (GPa)	Reference
Aggregate dry	14 (18*)	1 - 2	<i>Karato and Jung</i> , 2003
Aggregate dry	27	0.6 - 2.0	<i>Borch and Green II</i> , 1989
Aggregate dry	13.4 (18*)	0.5 - 1.5	<i>Ross et al.</i> , 1979
Aggregate dry	14	0.3 - 15	<i>Karato and Rubie</i> , 1997
Aggregate wet	24	1 - 2	<i>Karato and Jung</i> , 2003
Aggregate**	12.8	3.8 - 8.1	<i>Bollinger et al.</i> , 2014
[100](010) dry [#]	12	3.5 - 8.5	<i>Raterron et al.</i> , 2009
[001](010) dry [#]	3	3.5 - 8.5	<i>Raterron et al.</i> , 2009

* Corrected for the pressure effect on thermocouple emf [*Hirth and Kohlstedt*, 2003]

** This fits for both dry and wet samples

Single crystal in different slip systems

1.5.1.4 Effect of water on the deformation of olivine

The effect of water is reflected in the exponent r in the equation of 1.5.1.1. However, this equation assumes that the effect of water on olivine creep is made by changing point defect concentrations in the crystal. This is true for diffusion creep since deformation by this mechanism is controlled by the motions of point defects. On the other hand, the validation of this assumption needs to be tested for dislocation creep and GBS. It is valid only when dislocation creep and GBS are controlled by climb. Furthermore, it must also be noted that the power law dependence on water is empirical. For example, one may expect that the incorporation of water may reduce bond strengths in crystals, leading to a reduction in the activation energy of creep, where the effect of water should be included in the Boltzmann factor. Practically, the power-law formalism of Eq. 1.5.1.1 predicts to a zero creep rate at zero water content, which is unreasonable. Although workers assume a switchover from dry to wet constitutive equations at some water content, definition of the switchover of water content is quite arbitrary.

Judging from deformation experiments [compiled by *Hirth and Kohlstedt, 2003*], the exponent r is around 1.2, which indicates a large effect of water. Water content increases from the lithosphere to the asthenosphere [*Hirth and Kohlstedt, 1996*]. Therefore, it could explain the softening of the asthenosphere as demonstrated in Chapter 1.2.1.

1.5.1.5 Fabric transitions in olivine

As discussed in Chapter 1.2.3, different thermomechanical conditions can lead to different fabrics, and fabrics can be recognized by seismic anisotropies. Therefore, if we know thermochemical conditions under which a fabric forms, we could deduce mantle flow geometries from seismic anisotropy (Fig 1.2.5). Moreover, knowledge of conditions of the fabric formation could help to explain the variation of seismic anisotropy in different regions in the mantle because the magnitudes of anisotropy of different fabrics are different (Table 1.5.3). Thus, many deformation experiments aim at determining fabrics under different conditions.

Fig 1.5.1 summarizes the present knowledge of fabric transitions in olivine.

It can be seen that A-type fabric dominates over the B-type at high temperatures, and that fabric changes from A-type to E-type and then to C-type with increasing water content. In addition, B-type fabric dominates at high stresses. These results can be used to explain seismic observations in different mantle regions. The E-type fabric has a lower V_{SV}/V_{SH} seismic anisotropy than the A-type. Therefore, the decrease in V_{SV}/V_{SH} seismic anisotropy with depth can be explained by this A- to E-fabric transition. If the mantle flows in the trench-normal direction, the polarization direction of fast shear wave caused by B- and A-type fabrics are trench-parallel and trench-vertical, respectively. Therefore, the observed change in the polarization directions of fast shear waves across Japan trench [Nakajima and Hasegawa, 2004] can be explained by the A- to B-type fabric transition due to stress decrease away from the trench without introducing trench-parallel mantle flows [e.g. Jung and Karato, 2001].

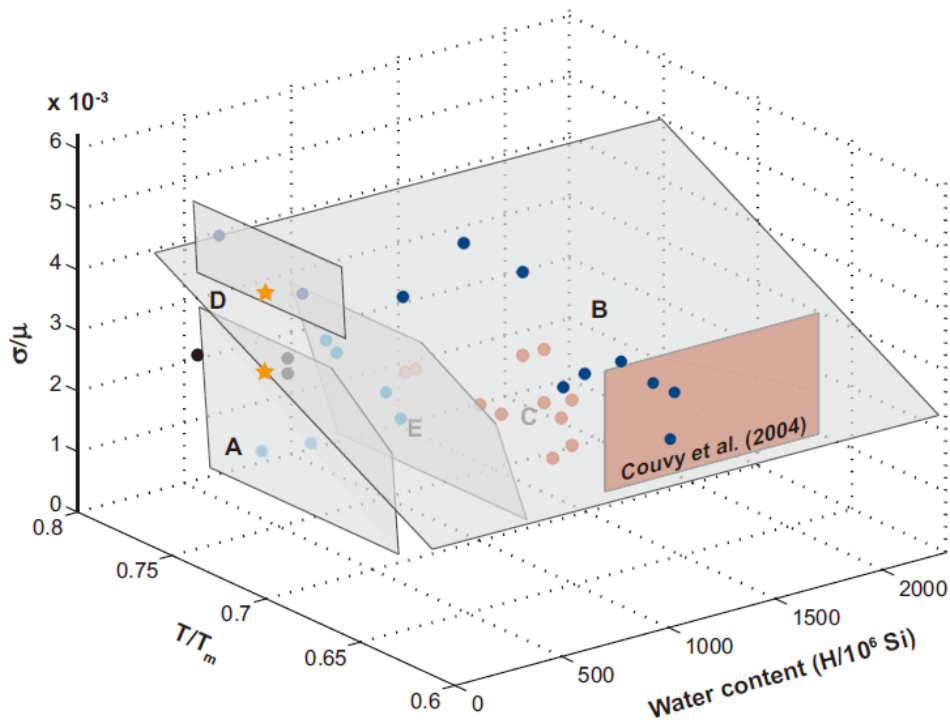


Fig 1.5.1 Olivine fabrics at different conditions [From Karato et al., 2008]

Besides temperature and stress, pressure can also cause the A- to B-type transition, which

was suggested by *Raterron et al.* [2007; 2009; 2011]. They found that the activation volume of the [100](010) slip system was higher than that of the [001](010) slip system, This indicates that the B-type fabric should dominate at high pressures. The transition occurs at pressures around 8 GPa. This can also explain the observed decreases in seismic anisotropy with depth.

It is interesting to note that different fabrics dominate at different conditions indicates that there is no uniform constitutive equation for dislocation creep. Experimental data were usually fitted to one constitutive equation in a limited experimental range. This process neglects contributions of different slip systems to total strain. However, existence of dominant fabric under different conditions indicates that strain rates caused by different slip systems must be different. Therefore, the experimentally obtained constitutive equations should not be extrapolated beyond the experimental ranges in which the data were obtained, because such an extrapolation may over/underestimate the contributions for certain slip systems. An appropriate way to construct a constitutive equation is to obtain such equations for different slip systems and then to sum them together.

Table 1.5.3 Olivine fabrics and corresponding seismic anisotropy information

Shear wave splitting, polarization direction of fast shear wave		
Fabric	Horizontal flow	Vertical planar flow
A-type	Parallel to flow	Small splitting
B-type	Vertical to flow	Parallel to the plane
C-type	Parallel to flow	Vertical to the plane
D-type	Parallel to flow	Small splitting
E-type	Parallel to flow	Small splitting
V_{SH}/V_{SV} anisotropy		
A-type	$V_{SH}/V_{SV} > 1$	$V_{SH}/V_{SV} < 1$
B-type	$V_{SH}/V_{SV} > 1$	$V_{SH}/V_{SV} > 1$ (weak)
C-type	$V_{SH}/V_{SV} < 1$	$V_{SH}/V_{SV} > 1$ (weak)
D-type	$V_{SH}/V_{SV} > 1$	$V_{SH}/V_{SV} < 1$

E-type	$V_{SH}/V_{SV} > 1$ (weak)	$V_{SH}/V_{SV} < 1$
--------	----------------------------	---------------------

1.5.2 Diffusion experiments

The data obtained from diffusion experiments are fitted to an equation

$$D = D_0 f_{O_2}^m C_{H_2O}^r \exp\left(-\frac{E+P\Delta V}{RT}\right) \quad (1.5.2)$$

where E and ΔV are the activation energy and volume for diffusion, respectively. The exponents m and r are applied oxygen fugacity and water content, respectively. Since Si is the slowest diffusion species in olivine, it is expected that rheological properties of olivine are controlled by Si diffusion. There are several studies on Si diffusivity summarized in Table 1.5.4. Si diffusivities from these studies are plotted against the reciprocal temperature in Fig. 1.5.2.

Table 1.5.4 Experimental results for Si lattice and grain boundary (GB) diffusivity

Type	T (K)	P (GPa)	E (kJ/mol)	ΔV (cm ³ /mol)	reference
Lattice*	1600-2000	10 ⁻⁴	368 ± 38	-	Jaoul et al., 1981
Lattice#	1400-1800	10 ⁻⁴	291 ± 15	-	Houlier et al, 1990
Lattice#	1763	4-9	-	0.7 ± 2.3	Bejina et al., 1999
Lattice#	1373-1773	10 ⁻⁴	529 ± 41	-	Dohmen et al., 2002
Lattice##	1473-1623	2	358 ± 28	-	Costa and Chakraborty, 2008
Lattice *	1600, 1800	10 ⁻⁴ -13	410 ± 30	1.7 ± 0.4	Fei et al., 2012
GB*	900-1200	10 ⁻⁴	203 ± 36	-	Farver and Yund, 2000
GB*	1200-1600	10 ⁻⁴ -8	220 ± 30	4.0 ± 0.7	Fei et al., 2016

* Dry forsterite; # Dry olivine; ## Wet olivine

The magnitudes of Si lattice diffusivity ($D_{\text{Si}}^{\text{lattice}}$) vary by around 3 orders of magnitude among different studies (Fig 1.5.2). This may be due to the difficulty of Si diffusivity measurements due to the very low magnitudes of diffusivity. Estimated creep rates from $D_{\text{Si}}^{\text{lattice}}$ are much lower than those shown by deformation experiments. This discrepancy can be explained by introducing pipe diffusion [Hirth and Kohlstedt, 2015]. However, judging from the activation energy discussed in Chapter 1.5.1.1, their explanation is also problematic.

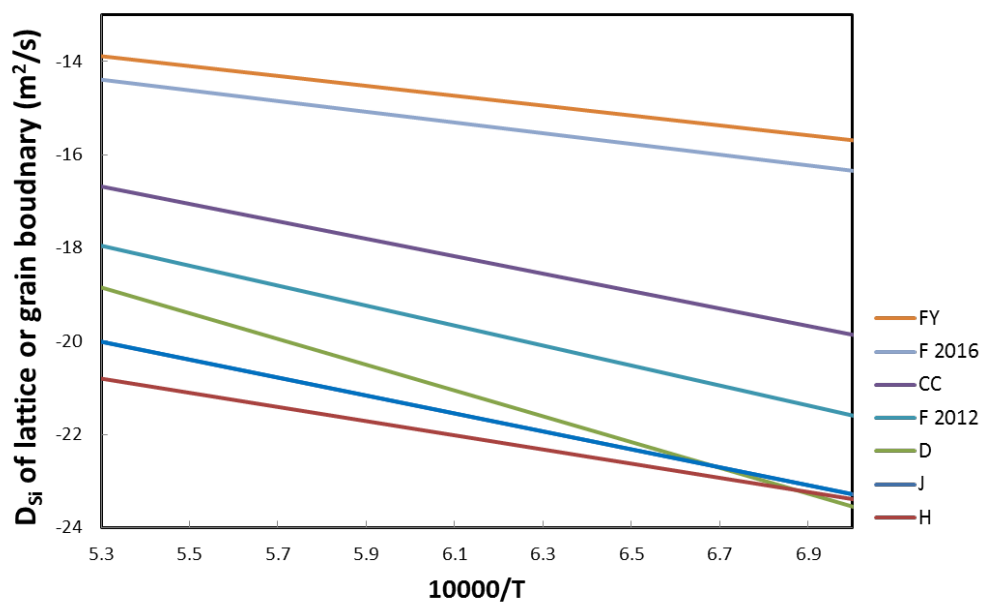


Fig 1.5.2 Diffusivities of Si against the reciprocal temperature from previous studies (Table 1.5.4). The plot of Si grain-boundary diffusivity ($D_{\text{Si}}^{\text{GB}}$) from Fei 2016 is obtained by assuming a grain boundary with ~ 10 nm width. The legends are abbreviations from from Table 1.5.4. For example, FY means Farver and Yund, 2000.

Reported activation energy of Si lattice diffusion ranges from 200 kJ/mol to 530 kJ/mol. Results from *Dohmen et al.* [2002] were obtained at constant oxygen fugacity while the others were obtained at constant oxygen buffer conditions if controlled. The activation energy and volume determined by *Fei et al.* [2012] were obtained simultaneously by fitting their data at two different temperatures and different pressures to Eq. 1.5.2. Namely, they did not design a

temperature-series of experiments to obtain the activation energy. The activation energy of $D_{\text{Si}}^{\text{lattice}}$ generally agrees with that of diffusion creep, implying that diffusion creep might be controlled by the lattice diffusion. This agreement contradicts the conclusion that diffusion creep is controlled by grain-boundary diffusion (Chapter 1.5.1.1). The activation energy of $D_{\text{Si}}^{\text{lattice}}$ is much smaller than that of dislocation creep. This indicates that the creep mechanism in deformation experiments may not be controlled by lattice diffusion. Results from *Dohmen et al.* [2002] rendered a high E . However, the dislocation creep experiments conducted at constant oxygen fugacity [*Keefner et al.*, 2011] gave a lower activation energy around 450 kJ/mol.

The activation energies for $D_{\text{Si}}^{\text{GB}}$ by two studies are consistent and are lower than that in diffusion creep. This also indicates that the diffusion creep is not controlled by grain boundary diffusion of Si.

Results from the studies of ΔV agree with each other. This agreement means that, if olivine creep is controlled by Si lattice diffusion, the pressure dependence of olivine creep must be smaller than the experimentally obtained values. The activation volumes obtained by deformation experiments, are actually much higher than those given by diffusion experiments, although their uncertainties are large. This disagreement regarding pressure dependence also raises a question regarding the assumption that deformation is controlled by diffusion.

The effect of water on $D_{\text{Si}}^{\text{lattice}}$ was investigated by *Costa and Chakraborty* [2008] and *Fei et al.* [2013], who found that the water exponents are 1.2 and 0.3, respectively. *Costa and Chakraborty* [2008] fitted their high-pressure (therefore high water contents) data and room-pressure (therefore low water contents) data to a single constitutive equation. Their different experimental setups may bias their results. In contrast, *Fei et al.* [2013] fitted the data from the experiments with identical setups. Therefore, their results should be more reliable. The effect of water on $D_{\text{Si}}^{\text{GB}}$ [*Fei et al.*, 2016] is as small as that of $D_{\text{Si}}^{\text{lattice}}$ indicated by *Fei et al.* [2013]. Therefore, the effect of water on Si diffusion also contradicts with that from deformation experiments, according to which the water exponent is around 1.

The oxygen fugacity exponent, m , of $D_{\text{Si}}^{\text{lattice}}$ in natural olivine was found to be -1/6 [*Houlier et al.*, 1990], which is also inconsistent with the results from dislocation creep

experiments.

1.5.3 Dislocation recovery experiments

Dislocation recovery experiments on olivine single crystals and aggregates have been performed by several studies, and are summarized in Table 1.5.5. Since dislocation motions are thermally activated processes, the rate constants are fitted by the Arrhenius equation

$$k = k_0 f_{O_2}^m \exp\left(-\frac{E + P\Delta V}{RT}\right) \quad 1.5.1$$

where E and ΔV are the activation energy and volume for recovery, and m is the oxygen-fugacity exponent. The parameters obtained by previous studies are summarized in Table 1.5.6. The rate constants plotted against the reciprocal temperature are in Fig. 1.5.3

The absolute values of k in previous studies varied by one order of magnitude (Fig 1.5.3). This variation is much smaller than those in Si self-diffusion experiments, and the uncertainty for each data point is much smaller than that in the diffusion experiments. The main reason is that the diffusion distance of Si in diffusion experiments is very small, which makes the determination of concentration-distance profiles difficult. The values from *Karato et al.* [1993] are about 0.8 orders of magnitude lower than those from *Karato and Ogawa* [1982]. This is due to the different methods in counting dislocation densities as explained by *Farla et al.* [2011]. The rate constants obtained for single crystals are generally higher than those for aggregates, indicating that grain boundaries may hinder dislocation annihilation. One possibility is that when a single dislocation moves to a grain boundary, it disappears but when one dislocation meets another, two dislocations disappear. Therefore, assuming that grain boundaries and dislocations have the same ability to attract one free dislocation, the density reduction due to dislocation-dislocation annihilation should be higher.

Table 1.5.5 Summary of previous study in dislocation recovery in olivine

Sample	T (K)	P (GPa)	Observation method	Reference
Single	1563-1723	10^{-4}	TEM	<i>Goetze and Kohlstedt, 1973*</i>
Aggregate	1573-1773	10^{-4}	OM	<i>Toriumi and Karato, 1978</i>
Single	1525-1675	$10^{-4}, 0.5$	TEM	<i>Kohlstedt et al., 1980</i>
Single	1613-1788	$10^{-4}, 2$	OM	<i>Karato and Ogawa, 1982</i>
Single**	1673	10^{-4}	OM	<i>Karato and Sato, 1982</i>
Single	1773	10^{-4} -10	SEM	<i>Karato et al., 1993</i>
Aggregate	1373-1723	10^{-4}	SEM	<i>Farlar et al., 2011</i>

* This study did not study dislocation annihilation but collapse of sessile dislocation loop.

** The oxygen partial pressure ranged from 10 to 10^{-6} Pa in this study

Table 1.5.6 Summary of previous results on dislocation recovery of olivine

Reference	E (kJ/mol)	ΔV (cm ³ /mol)	m
<i>Geotze and Kohlstedt, 1973*</i>	565 ± 125	-	-
<i>Toriumi and Karato, 1977</i>	460 ± 40	-	-
<i>Kohlstedt et al., 1980</i>	300 ± 15	11 ± 1	
<i>Karato and Ogawa, 1982</i>	389 ± 59	14 ± 2	
<i>Karato and Sato, 1982</i>	-	-	-1/6
<i>Karato et al., 1993</i>	-	6 ± 1	-
<i>Farla et al., 2011</i>	355 ± 81	-	-

Reported values of the activation energy of annihilation rate constants are between 300 and 450 kJ/mol (Table 1.5.6). These values generally agree with the results from Si lattice diffusion experiments, suggesting that dislocation motions are controlled by diffusion, namely

climb. However, the smaller E of the rate constants compared with that in dislocation creep experiments indicates that dislocation creep in experiments is not controlled by climb. The higher E in *Geotze and Kohlstedt (1973)* was obtained by measuring the collapsing rates of sessile dislocation loops. Although collapse of sessile loops also involves climb, the jog concentration of free dislocations, which influences the rates of dislocation annihilation, and sessile loops may be different. Moreover, dislocation annihilation has to occur during deformation in order to reach a steady state while collapse of sessile loops is not necessary in deformation. Therefore, the E of annihilation rate constants is more relevant to deformation.

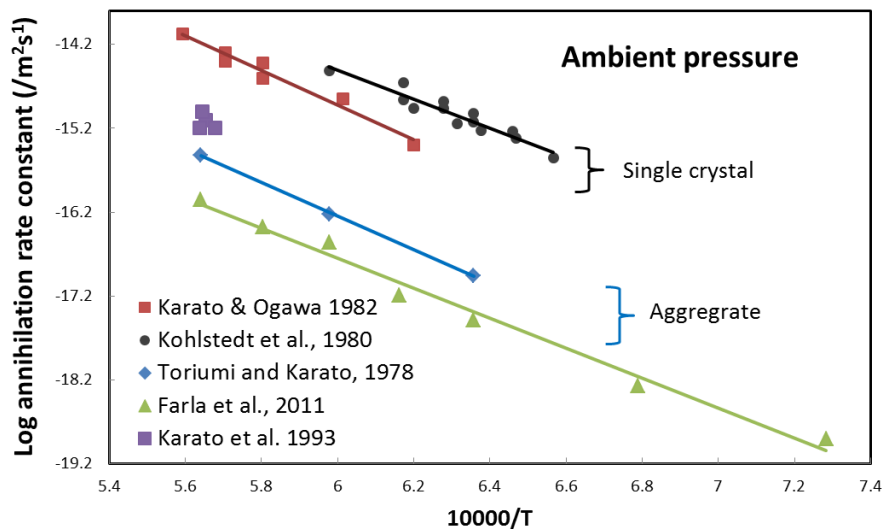


Fig 1.5.3 Rate constants of dislocation recovery in olivine from previous studies (Table 1.5.6)

The activation volumes of rate constants are different by a factor of 3 among previous studies. The activation volumes become smaller if the investigated pressure range is wider. In general, the values obtained in dislocation recovery experiments are smaller than those in dislocation-creep experiments. The smallest reported activation volume is 6 cm³/mol., which was obtained by *Karato et al. (1993)* with a pressure range from 10⁻⁴ to 10 GPa. This value is close to those determined from Si lattice diffusion experiments.

The oxygen fugacity dependence of the rate constants was found with the exponent around -1/6 by *Karato and Sato (1982)*. Again, this value agrees with the results from diffusion

experiments but disagrees to those from dislocation-creep experiments.

1.6 Aims of this study

Olivine is the most abundant and weakest mineral in the Earth's upper mantle. Therefore, creep in the upper mantle is mainly controlled by the rheological properties of olivine. Among various deformation mechanisms, dislocation creep is the main cause of the seismic anisotropy. Although there are many studies that have focused on the dislocation-creep region in olivine, an inherent problem in those experiments (Chapter 1.4.1 and 1.4.2) means that their results should be checked by an independent method. The dislocation recovery method focuses on dislocation motions. The majority of previous studies did not distinguish between different slip systems. Therefore, I adopted the dislocation recovery method to study dislocation motions of different slip systems using olivine single crystals in this study. Moreover, there are various discrepancies between deformation experiments, diffusion and dislocation recovery experiments (Table 1.6.1). It is unclear which mechanism is dominant for olivine creep in the Earth's mantle. For this reason, I also test the possibility of cross-slip as the rate-limiting process in dislocation motions by the recovery method.

Table 1.6.1 Discrepancies among different studies with different techniques

	Deformation exp.	Diffusion	Annihilation
E	~ 530 kJ/mol*	~ 400 kJ/mol [#]	~ 400 kJ/mol [!]
ΔV	>14 cm ³ /mol*	1.7 cm ³ /mol [#]	6 cm ³ /mol ^{¥¥}
f_{O_2} effect	Exponent of $1/5^{\&}$	Exponent of $-1/6^{\text{¥}}$	Exponent of $-1/6^{\&\&}$
Water effect	Exponent of 1.2^*	Exponent of $0.3^{\#}$	-
Isotropy	Different fabrics**	Isotropic ^{##}	-

* *Hirth & Kohlstedt et al.*, 2003; ** *Karato*, 2012; # *Fei et al.*, 2013; & *Keefner et al.*, 2011; && *Karato & Sato*, 1982; ¥ *Houlier et al.*, 1990; ## *Jaoul et al.*, 1981; ! *Karato & Ogawa*, 1982; ¥¥ *Karato et al.*, 1993

1.6.1 Temperature dependence of annihilation rate constants for A-type and B-type dislocations

Deformation experiments suggested that A-type dislocations should dominate at high temperatures, while B-type dislocations dominate at low temperatures (Fig 1.5.1). This indicates that the activation energy of A-type dislocations is higher than that of B-type dislocations. However, there are neither deformation nor recovery experiments to compare dislocation mobility of these two slip systems.

AG-type fabric was found in nature [*Ismail and Mainprice, 1998*; categorized by *Mainprice, 2007*]. This fabric suggests that both A-type and B-type dislocations have similar mobilities. Therefore, in order to understand the temperature dependence of these two slip systems, dislocation recovery experiments were conducted at room pressure with a temperature range of 1473-1773 K at oxygen partial pressure near nickel-nickel oxide (NNO) buffer conditions in a gas mixing furnace using Pakistan olivine.

1.6.2 Pressure dependence of annihilation rate constants for A-type and B-type dislocations

Different studies involving high-pressure deformation experiments have reported significantly different activation volumes, They are generally larger than those determined from diffusion experiments. Reasons for this difference are not understood. Therefore, a better constraint for the activation volume for olivine creep is necessary by using a different method from deformation and diffusion experiments.

Deformation experiments suggested that B-type dislocations dominate at high pressures, while A-type dislocations dominate at low pressures (Chapter 1.5.1.5). If this is the case in natural conditions, it can explain the decreases of seismic anisotropies with depth. Although *Raterron et al. [2009]* studied strain rates caused by A-type and B-type dislocations, their activation volumes for these two slip systems were obtained by fitting their own high-pressure

data and previous low-pressure data from other studies. Different experimental setups may bias the results.

Karato et al. [1993] reported that climb of A-type dislocations has an activation volume of $6 \text{ cm}^3/\text{mol}$. There are no data for the activation volume of B-type dislocations. Therefore, dislocation recovery experiments were conducted for A-type and B-type dislocations from 2 to 12 GPa at 1650 K to obtain better constraints for the activation volumes of these two slip systems.

1.6.3 Water dependence of annihilation rate constants for C-type dislocations

As demonstrated in Chapter 1.5.1.4, water could cause fabric transitions, which were determined by deformation experiments. Namely, A-type dislocations dominate at low water contents while C-type dislocations dominate at high water contents. Like the pressure effect, this fabric transition may explain the decreases of seismic anisotropies with depth, because the C-type fabric has a lower V_{SH}/V_{SV} seismic anisotropy. In addition to the fabric transition, it was also claimed that water incorporation softens olivine. Deformation experiments reported that a hydrous olivine deforms faster than a dry olivine in proportion the water content raised to the power 1.2 (Chapter 1.5.1.3). We know that the asthenosphere is more hydrous than the lithosphere. The softening of the asthenosphere might be explained by the hydrous weakening of olivine if those results are applicable to the natural conditions.

However, *Fei et al.* [2013] demonstrated that the water effect on Si lattice self-diffusion is small. Namely, the diffusivity increases in proportion water content to 0.3 power. Therefore, they expected that the effect of water on dislocation creep is small. They attributed the large water exponent reported by deformation experiments to free water in grain boundaries and high stresses in those experiments. In order to obtain better understanding about the effect of water on olivine dislocation creep, we conducted dislocation annihilation experiments on C-type dislocations at 5 GPa, 1473 K with a water content range from 5 to 100 wt. ppm. Because

C-type fabric was suggested to be dominant at high water contents and the water exponent in dislocation-creep experiments is 1.2, the water exponent for C-type dislocation mobility should be higher than 1.2

1.6.4 TEM study of E-type dislocations at different conditions

Deformation experiments suggested that olivine fabrics change from A-type to E-type then to C-type with increasing water content [Jung and Karato, 2001; Jung *et al.*, 2006; Katayama *et al.*, 2004]. E-type was proposed to be a candidate for the dominant fabric at upper mantle conditions [Karato *et al.*, 2008]. A-type and C-type are well documented both in natural and laboratory deformed samples and the responsible slip systems for these two fabrics are well studied. However, there are a limited number of reports regarding E-type fabrics from natural samples. Moreover, the responsible slip system for this fabric, namely, [100](001) was never confirmed by TEM observations under hydrous conditions. In this study, it was examined whether and at what water content the [100](001) slip system is activated.

Olivine single crystals were first annealed under dry or wet conditions, and then simply sheared in the [100] direction on the (001) plane, trying to activate the target slip system at pressures of 2~5 GPa, temperatures of 1473 and 1600 K under dry or wet conditions. Thin sections parallel to the (001) plane of the deformed samples were prepared, and then argon milled for TEM observations to examine their dislocation structures.

1.6.5 Examination of cross-slip as a controlled mechanism for olivine deformation

The constitutive equation for olivine dislocation creep at high temperatures is based on the climb-controlled model, namely, dislocation motion is rate-limited by diffusion-controlled climb of edge dislocation segments. However, there are many discrepancies between results from deformation experiments and diffusion/recovery experiments (Table 1.6.1), suggesting that the mechanism in olivine dislocation creep may be not controlled by climb. Moreover,

both motions of screw and edge segments are needed for a dislocation loop to produce macroscopic strains. If the rate-limiting process of screw dislocation segments is different from that of edge segments, the rheology of olivine should be reconsidered.

Cross-slip of screw dislocations was proposed as a rate-limiting process by *Poirier et al* [1976] because cross-slip of dissociated screw dislocations needs additional energy to recombine partial dislocations. However, whether cross-slip can be a rate-limiting process for olivine high-temperature creep has never been examined in experimental studies. Therefore, we conducted dislocation recovery experiments on [001](010) screw and edge dislocations to compare their activation energies at room pressure at temperatures ranging from 1473 to 1773 K.

1.7 General techniques in this study

1.7.1 Sample preparation

Samples used in this study are single crystals of natural olivine from Pakistan. The same olivine has been describe by *Gose et al.* [2010] and its major and trace elements, including water content, were reported there, and are shown in Table 1.7.1. Inclusion- and crack-free grains were handpicked under an optical microscope.

Table 1.7.1 Composition of olivine used in this study. The major-element contents are in wt.% while those of the trace-element are in wt. ppm (from *Gose et al.*, 2010).

SiO ₂	MgO	FeO	NiO	MnO					
1.29	49.95	8.79	0.35	0.13					
Li	Be	B	Ca	Sc	Ti	V	Cr	Co	H ₂ O
19	<0.02	37	243	1.9	12	2.1	68	133	35/51

Orientations of single crystals were determined using a single-crystal X-ray diffractometer (Oxford diffraction Xcalibur 2) at the University of Bayreuth. This

diffractometer is equipped with a two-dimensional CCD detector and allows a crystal to rotate in two directions. After obtaining orientation information, the crystals were transferred to a highly precise single-crystal X-ray diffractometer (Huber SMC 9000) operated by SINGLE2014 software [Angel and Finger, 2011] at the University of Bayreuth. One crystallographic plane ((100), (010) or (001)) of the crystals was orientated with a precision of 0.1° parallel to the horizontal plane and then mounted in the epoxy resin. The plane was then polished using diamond powders with a grain size of $0.25\ \mu\text{m}$. The other two planes were determined by means of electron backscattered diffraction (EBSD) in a scanning electron microscope (SEM). Cubes were shaped from the oriented crystals along their crystallographic planes. The orientations of the crystals were checked again by EBSD after shaping the cubes.

1.7.2 Deformation experiments

The purpose of deformation experiments is to produce initial dislocations in the crystals. The orientated crystals were put in MgO slices with a cubic hole at the center, and then sandwiched between two crushable alumina pistons, cut at an angle of 45° for simple shear deformation. Depending on a target slip system, different crystallographic axes were aligned in shear directions. Experiments were conducted in a Kawai-type multi-anvil apparatus at the University of Bayreuth at a pressure of 3 or 5 GPa and a temperature of 1,600 or 1473 K.

Cell assemblies were first pressurized to target pressures, and then temperatures were increased to the target values. After holding them for 15 min to sinter the crushable alumina pistons, the cell assemblies were then further compressed by increasing the press load to deform the samples. After deformation, the samples were quenched by switching off heating power. The cell assemblies were then decompressed to ambient pressure.

After decompression, the pressure media with the samples were polished to expose the shear planes of the crystals. Deviation of the crystallographic axes from shear directions was examined by means of EBSD. Shear directions were assumed to be aligned along the long

axes of the MgO slices.

1.7.3 Dislocation recovery

Room-pressure recovery experiments were conducted in a CO/CO₂ gas-mixing furnace at the University of Bayreuth. Deformed crystals were annealed at temperatures ranging from 1,460 to 1,760 K for 20 min to 24.5 hours. Oxygen partial pressures were controlled at 10⁻⁶ to 10⁻⁸ MPa by changing CO/CO₂ ratio, which were near the NNO-buffer conditions.

High-pressure recovery experiments were conducted in Kawai-type multi-anvil apparatus. Deformed samples were buffered by enstatite to control the silica activity. The oxygen fugacity was controlled by different buffers in different experiments. An undeformed sample was annealed in the same setup to check the stress in such assembly by counting dislocation density increase.

1.7.4 Observations of dislocations

Deformed olivine crystals were examined by TEM to determine whether the target slip systems were activated or not. In addition, characters of dislocations were determined. Samples were polished on both sides parallel to the shear planes until the thicknesses ranges from 23 to 35 μm . Then, Ar ion-milling was used to make the sample thinner, using voltages of 4.5 to 5 kV voltages, at an elevation angle of 4 to 8° from the top and bottom ion-bombardment. Dislocation microstructures were examined by dark field (DF, Bragg condition, deviation parameter, $s = 0$) and weak-beam dark field (WBDF, $s > 0$) imaging and selected area electron diffraction (SAED). We chose appropriate diffraction vectors (g) to identified the Burger's vectors. When $g \cdot b = \text{integer}$, dislocations are visible by diffraction contrast. Since dislocations were observed on the slip planes, they should be screw dislocations if they elongate in the shear direction, and they should be edge dislocations if their elongation direction is perpendicular to the shear direction.

Dislocation densities before and after annealing were measured using the oxidation

decoration technique combined with SEM [Karato, 1987; Kohlstedt *et al.*, 1976]. Samples were first heated at a temperature of 1,170 K for 1 hour in air to oxidize dislocations. The sample surfaces were subsequently polished using 0.25 μm diamond powder to remove the surface Fe-oxide layer, and then observed in back-scattered electron images (BEI) by SEM at around 10-mm working distance, accelerating voltage of 10 kV, and an aperture of 120 μm . Dislocations appeared as bright spots or lines because iron oxides precipitate and grow in dislocation cores. Dislocations were counted on the planes normal to the dislocation lines. On these planes, dislocations intersect orthogonally and appear as bright dots. The dislocation density was calculated from the number of the intersecting dislocations per unit area following Karato *et al.*, [1993].

1.7.5 Data reductions

The rate constant, k , was calculated using Eq. 1.4.2. After obtaining k at different conditions, the results were fitted using the equation

$$k = k_0 C_{\text{H}_2\text{O}}^r \exp\left(-\frac{E+P\Delta V}{RT}\right) \quad (1.7.1)$$

where k_0 is a pre-exponential factor, E and ΔV are the activation energy and volume for the rate constant, respectively, $C_{\text{H}_2\text{O}}$ is the water content in olivine, r is the exponent of water content, T is the absolute temperature, P is the pressure.

1.8 References

- Angel, R., Finger, L., 2011. SINGLE: a program to control single-crystal diffractometers. *Journal of Applied Crystallography* 44, 247-251.
- Bailey, D., Flanagan, W., 1967. The relationship between dislocation density and flow stress in materials deforming by a peierls-nabarro mechanism. *Philosophical Magazine* 15, 43-49.
- Béjina, F., Jaoul, O., Liebermann, R.C., 1999. Activation volume of Si diffusion in San Carlos

- olivine: Implications for upper mantle rheology. *Journal of Geophysical Research: Solid Earth* 104, 25529-25542.
- Bollinger, C., Raterron, P., Cordier, P., Merkel, S., 2014. Polycrystalline olivine rheology in dislocation creep: Revisiting experimental data to 8.1 GPa. *Physics of the Earth and Planetary Interiors* 228, 211-219.
- Borch, R., Green II, H., 1989. Deformation of peridotite at high pressure in a new molten salt cell: Comparison of traditional and homologous temperature treatments. *Physics of the Earth and Planetary Interiors* 55, 269-276.
- Bussod, G., Katsura, T., Rubie, D., 1993. The large volume multi-anvil press as a highP-T deformation apparatus. *PAGEOPH* 141, 579-599.
- Costa, F., Chakraborty, S., 2008. The effect of water on Si and O diffusion rates in olivine and implications for transport properties and processes in the upper mantle. *Physics of the Earth and Planetary Interiors* 166, 11-29.
- Dohmen, R., Chakraborty, S., Becker, H.W., 2002. Si and O diffusion in olivine and implications for characterizing plastic flow in the mantle. *Geophysical research letters* 29.
- Durham, W., Goetze, C., 1977. A comparison of the creep properties of pure forsterite and iron-bearing olivine. *Tectonophysics* 40, T15-T18.
- Dziewonski, A.M., Anderson, D.L., 1981. Preliminary reference Earth model. *Physics of the Earth and Planetary Interiors* 25, 297-356.
- Farla, R.J.M., Kokkonen, H., Fitz Gerald, J.D., Barnhoorn, A., Faul, U.H., Jackson, I., 2011. Dislocation recovery in fine-grained polycrystalline olivine. *Physics and Chemistry of Minerals* 38, 363-377.
- Farver, J.R., Yund, R.A., 2000. Silicon diffusion in forsterite aggregates: Implications for diffusion accommodated creep. *Geophysical Research Letters* 27, 2337-2340.
- Fei, H., Hegoda, C., Yamazaki, D., Wiedenbeck, M., Yurimoto, H., Shcheka, S., Katsura, T., 2012. High silicon self-diffusion coefficient in dry forsterite. *Earth and Planetary Science Letters* 345–348, 95-103.
- Fei, H., Koizumi, S., Sakamoto, N., Hashiguchi, M., Yurimoto, H., Marquardt, K., Miyajima,

- N., Yamazaki, D., Katsura, T., 2016. New constraints on upper mantle creep mechanism inferred from silicon grain-boundary diffusion rates. *Earth and Planetary Science Letters* 433, 350-359.
- Fei, H., Wiedenbeck, M., Yamazaki, D., Katsura, T., 2013. Small effect of water on upper-mantle rheology based on silicon self-diffusion coefficients. *Nature* 498, 213-+.
- Frost, D.J., 2008. The upper mantle and transition zone. *Elements* 4, 171-176.
- Goetze, C., Kohlstedt, D.L., 1973. Laboratory study of dislocation climb and diffusion in olivine. *Journal of Geophysical Research* 78, 5961-5971.
- Gose, J., Schmaedicke, E., Markowitz, M., Beran, A., 2010. OH point defects in olivine from Pakistan. *Mineralogy and Petrology* 99, 105-111.
- Gueguen, Y., Darot, M., Mazot, P., Woïrgard, J., 1989. Q- 1 of forsterite single crystals. *Physics of the earth and planetary interiors* 55, 254-258.
- Gung, Y., Panning, M., Romanowicz, B., 2003. Global anisotropy and the thickness of continents. *Nature* 422, 707-711.
- Hager, B.H., 1984. Subducted slabs and the geoid: Constraints on mantle rheology and flow. *Journal of Geophysical Research: Solid Earth* 89, 6003-6015.
- Hansen, L.N., Zimmerman, M.E., Kohlstedt, D.L., 2011. Grain boundary sliding in San Carlos olivine: Flow law parameters and crystallographic-preferred orientation. *Journal of Geophysical Research: Solid Earth* 116, B08201.
- Haskell, N.A., 1937. The viscosity of the asthenosphere. *Am. J. Sci.*, 22-28.
- Hirth, G., Kohlstedt, D., 2003. Rheology of the Upper Mantle and the Mantle Wedge: A View from the Experimentalists, *Inside the Subduction Factory*. American Geophysical Union, pp. 83-105.
- Hirth, G., Kohlstedt, D., 2015. The stress dependence of olivine creep rate: Implications for extrapolation of lab data and interpretation of recrystallized grain size. *Earth and Planetary Science Letters* 418, 20-26.
- Hirth, G., Kohlstedt, D.L., 1996. Water in the oceanic upper mantle: implications for rheology, melt extraction and the evolution of the lithosphere. *Earth and Planetary Science Letters*

144, 93-108.

- Houlier, B., Cheraghmakani, M., Jaoul, O., 1990. Silicon diffusion in San Carlos olivine. *Physics of the Earth and Planetary Interiors* 62, 329-340.
- Hull, D., Bacon, D.J., 2001. *Introduction to dislocations*. Butterworth-Heinemann.
- Ismail, W.B., Mainprice, D., 1998. An olivine fabric database: an overview of upper mantle fabrics and seismic anisotropy. *Tectonophysics* 296, 145-157.
- Jackson, I., Gerald, F., John, D., Faul, U.H., Tan, B.H., 2002. Grain - size - sensitive seismic wave attenuation in polycrystalline olivine. *Journal of Geophysical Research: Solid Earth* 107.
- Jaoul, O., 1990. Multicomponent diffusion and creep in olivine. *Journal of Geophysical Research: Solid Earth* 95, 17631-17642.
- Jaoul, O., Poumellec, M., Froidevaux, C., Havette, A., 1981. Silicon diffusion in forsterite: a new constraint for understanding mantle deformation. *Anelasticity in the Earth*, 95-100.
- Jung, H., Karato, S.-i., 2001. Water-Induced Fabric Transitions in Olivine. *Science* 293, 1460-1463.
- Jung, H., Katayama, I., Jiang, Z., Hiraga, T., Karato, S., 2006. Effect of water and stress on the lattice-preferred orientation of olivine. *Tectonophysics* 421, 1-22.
- Karato, S.-i., 2012. *Deformation of earth materials: an introduction to the rheology of solid earth*. Cambridge University Press.
- Karato, S.-I., Jung, H., 2003. Effects of pressure on high-temperature dislocation creep in olivine. *Philosophical Magazine* 83, 401-414.
- Karato, S.-i., Jung, H., Katayama, I., Skemer, P., 2008. Geodynamic Significance of Seismic Anisotropy of the Upper Mantle: New Insights from Laboratory Studies. *Annual Review of Earth and Planetary Sciences* 36, 59-95.
- Karato, S.-i., Rubie, D.C., 1997. Toward an experimental study of deep mantle rheology: A new multianvil sample assembly for deformation studies under high pressures and temperatures. *Journal of Geophysical Research: Solid Earth* 102, 20111-20122.
- Karato, S.-I., Rubie, D.C., Yan, H., 1993. Dislocation recovery in olivine under deep upper

- mantle conditions: Implications for creep and diffusion. *Journal of Geophysical Research: Solid Earth* 98, 9761-9768.
- Karato, S.-i., Sato, H., 1982. Effect of oxygen partial pressure on the dislocation recovery in olivine: a new constraint on creep mechanisms. *Physics of the Earth and Planetary Interiors* 28, 312-319.
- Karato, S., 1987. Scanning electron microscope observation of dislocations in olivine. *Physics and Chemistry of Minerals* 14, 245-248.
- Karato, S., Ogawa, M., 1982. High-pressure recovery of olivine: implications for creep mechanisms and creep activation volume. *Physics of the Earth and Planetary Interiors* 28, 102-117.
- Katayama, I., Jung, H., Karato, S.-i., 2004. New type of olivine fabric from deformation experiments at modest water content and low stress. *Geology* 32, 1045-1048.
- Kawazoe, T., Nishihara, Y., Ohuchi, T., Nishiyama, N., Higo, Y., Funakoshi, K.-i., Irifune, T., 2011. In situ stress-strain measurements in a deformation-DIA apparatus at P-T conditions of the upper part of the mantle transition zone. *American Mineralogist* 96, 1665-1672.
- Kawazoe, T., Nishiyama, N., Nishihara, Y., Irifune, T., 2010. Deformation experiment at P-T conditions of the mantle transition zone using D-DIA apparatus. *Physics of the Earth and Planetary Interiors* 183, 190-195.
- Keefner, J., Mackwell, S., Kohlstedt, D., Heidelbach, F., 2011. Dependence of dislocation creep of dunite on oxygen fugacity: implications for viscosity variations in Earth's mantle. *Journal of Geophysical Research: Solid Earth* 116.
- Kinsland, G.L., Bassett, W.A., 1977. Strength of MgO and NaCl polycrystals to confining pressures of 250 kbar at 25 C. *Journal of Applied Physics* 48, 978-985.
- Kocks, U.F., Argon, A.S., Ashby, M., F., 1975. Thermodynamics and kinetics of slip. *Progress in Material Science* 19, 1-291.
- Kohlstedt, D., Nichols, H., Hornack, P., 1980. The effect of pressure on the rate of dislocation recovery in olivine. *Journal of Geophysical Research: Solid Earth (1978–2012)* 85, 3122-3130.

- Kohlstedt, D.L., 2006. The Role of Water in High-Temperature Rock Deformation. *Reviews in Mineralogy and Geochemistry* 62, 377-396.
- Kohlstedt, D.L., Goetze, C., 1974. Low-stress high-temperature creep in olivine single crystals. *Journal of Geophysical Research* 79, 2045-2051.
- Kohlstedt, D.L., Goetze, C., Durham, W.B., Sande, J.V., 1976. New Technique for Decorating Dislocations in Olivine. *Science* 191, 1045-1046.
- Langdon, T., 1994. A unified approach to grain boundary sliding in creep and superplasticity. *Acta Metallurgica et Materialia* 42, 2437-2443.
- Lawrence, J.F., Wysession, M.E., 2006. QLM9: A new radial quality factor (Q_{μ}) model for the lower mantle. *Earth and Planetary Science Letters* 241, 962-971.
- Mainprice, D., 2007. Seismic anisotropy of the deep Earth from a mineral and rock physics perspective. Schubert, G. *Treatise in Geophysics Volume 2* pp437-492. Oxford.
- Mainprice, D., Barruol, G., Ismail, W.B., 2000. The seismic anisotropy of the Earth's mantle: from single crystal to polycrystal. *Earth's Deep Interior: Mineral physics and tomography from the atomic to the global scale*, 237-264.
- Mei, S., Kohlstedt, D., 2000a. Influence of water on plastic deformation of olivine aggregates: 1. Diffusion creep regime. *Journal of Geophysical Research: Solid Earth* 105, 21457-21469.
- Mei, S., Kohlstedt, D.L., 2000b. Influence of water on plastic deformation of olivine aggregates 2. Dislocation creep regime. *Journal of Geophysical Research-Solid Earth* 105, 21471-21481.
- Montagner, J.P., Kennett, B.L.N., 1996. How to reconcile body-wave and normal-mode reference earth models. *Geophys. J. Int.* 125, 229-248.
- Nakajima, J., Hasegawa, A., 2004. Shear-wave polarization anisotropy and subduction-induced flow in the mantle wedge of northeastern Japan. *Earth and Planetary Science Letters* 225, 365-377.
- Nishiyama, N., Maeda, T., Irifune, T., Wada, K., Shinmei, T., Isobe, F., Akatsu, M., 2010. Pressure generation up to 55 GPa using a Drickamer-type apparatus with sintered

- diamond anvils toward use of nano-polycrystalline diamond as anvils, *Journal of Physics: Conference Series*. IOP Publishing, p. 012189.
- Ohuchi, T., Kawazoe, T., Higo, Y., Funakoshi, K.-i., Suzuki, A., Kikegawa, T., Irifune, T., 2015. Dislocation-accommodated grain boundary sliding as the major deformation mechanism of olivine in the Earth's upper mantle. *Science advances* 1, e1500360.
- Paterson, M., 1970. A high-pressure, high-temperature apparatus for rock deformation, *International Journal of Rock Mechanics and Mining Sciences & Geomechanics Abstracts*. Elsevier, pp. 517-526.
- Peach, M., Koehler, J.S., 1950. THE FORCES EXERTED ON DISLOCATIONS AND THE STRESS FIELDS PRODUCED BY THEM. *Physical Review* 80, 436-439.
- Peltier, W., 1998. Postglacial variations in the level of the sea: Implications for climate dynamics and solid - earth geophysics. *Reviews of Geophysics* 36, 603-689.
- Poirier, J.-P., 1985. *Creep of crystals: high-temperature deformation processes in metals, ceramics and minerals*. Cambridge University Press.
- Poirier, J.-P., Vergobbi, B., 1978. Splitting of dislocations in olivine, cross-slip-controlled creep and mantle rheology. *Physics of the Earth and Planetary Interiors* 16, 370-378.
- Poirier, J., 1976. On the symmetrical role of cross-slip of screw dislocations and climb of edge dislocations as recovery processes controlling high-temperature creep. *Revue de Physique Appliquée* 11, 731-738.
- Raterron, P., Amiguet, E., Chen, J., Li, L., Cordier, P., 2009. Experimental deformation of olivine single crystals at mantle pressures and temperatures. *Physics of the Earth and Planetary Interiors* 172, 74-83.
- Raterron, P., Chen, J., Geenen, T., Girard, J., 2011. Pressure effect on forsterite dislocation slip systems: Implications for upper-mantle LPO and low viscosity zone. *Physics of the Earth and Planetary Interiors* 188, 26-36.
- Raterron, P., Chen, J., Li, L., Weidner, D., Cordier, P., 2007. Pressure-induced slip-system transition in forsterite: Single-crystal rheological properties at mantle pressure and temperature. *American Mineralogist* 92, 1436-1445.

- Ricoult, D., Kohlstedt, D., 1985. Experimental evidence for the effect of chemical environment upon the creep rate of olivine. *Point defects in minerals*, 171-184.
- Ringwood, A., 1975. *Composition and Structure of the Earth's Mantle*. McGraw-Hill, New York.
- Ross, J.V., Ave'Lallemant, H.G., Carter, N.L., 1979. Activation volume for creep in the upper mantle. *Science* 203, 261-263.
- Shewmon, P., 2016. *Diffusion in solids*. Springer.
- Singh, A.K., 1993. The lattice strains in a specimen (cubic system) compressed nonhydrostatically in an opposed anvil device. *Journal of Applied Physics* 73, 4278-4286.
- Toriumi, M., Karato, S.-I., 1978. Experimental studies on the recovery process of deformed olivines and the mechanical state of the upper mantle. *Tectonophysics* 49, 79-95.
- Wang, Y., Durham, W.B., Getting, I.C., Weidner, D.J., 2003. The deformation-DIA: A new apparatus for high temperature triaxial deformation to pressures up to 15 GPa. *Review of Scientific Instruments* 74, 3002-3011.
- Weertman, J., 1999. Microstructural mechanisms of creep. *Mechanics and materials: Fundamentals and linkages*, 451-488.
- Yamazaki, D., Karato, S.-i., 2001. High-pressure rotational deformation apparatus to 15 GPa. *Review of Scientific Instruments* 72, 4207-4211.
- Yuen, D.A., Sabadini, R., Boschi, E.V., 1982. Viscosity of the lower mantle as inferred from rotational data. *Journal of Geophysical Research: Solid Earth* 87, 10745-10762.

2. List of manuscripts and statements of author's contribution

1. **Wang, L.**, S. Blaha, Z. Pintér, R. Farla, T. Kawazoe, N. Miyajima, K. Michibayashi, and T. Katsura (2016), Temperature dependence of [100](010) and [001](010) dislocation mobility in natural olivine, *Earth and Planetary Science Letters*, 441, 81-90

In this study, the idea comes from T. Katsura. LW performed all the deformation and annealing experiments. ZP conducted TEM observations under the instruction of NM. LW wrote the manuscript with further improvements of SB, ZP, RF, NM, KM, T. Kawazoe, and T. Katsura

2. **Wang, L.**, S. Blaha, T. Kawazoe, N. Miyajima, and T. Katsura (2017), Identical activation volumes of dislocation mobility in the [100](010) and [001](010) slip systems in natural olivine, *Geophysical Research Letters*, 44, 2687-2692.

In this study, the idea comes from T. Katsura. LW performed all the deformation and annealing experiments. LW wrote the manuscript with further improvements of SB, T. Kawazoe, NM and T. Katsura.

3. **Wang, L.** and T. Katsura (2018), Identical mechanism for the motion of screw and edge dislocations in natural olivine, *Geology*, (under review).

In this study, the idea comes from LW. LW performed all the deformation and annealing experiments. LW wrote the manuscript with further improvements of TK.

4. **Wang, L.**, N. Miyajima, T. Kawazoe, T. Katsura (2018), Activation of [100](001) slip system by water incorporation in olivine, *American Mineralogist*, (submitted).

In this study, the idea comes from T. Katsura. LW performed all the deformation experiments. TEM observations were conducted by LW under the instruction of NM. LW wrote the manuscript with further improvements of T. Kawazoe, NM and T. Katsura.

5. **Wang, L.**, T. Kawazoe, N. Miyajima, and T. Katsura, Small effect of water on olivine dislocation creep (Completed manuscript for submission)

In this study, the idea comes from T. Katsura. LW performed all the deformation and annealing experiments. LW wrote the manuscript with further improvements of T. Kawazoe, NM and T. Katsura.

3. Temperature dependence of [100](010) and [001](010) dislocation mobility in natural olivine

Lin Wang^{a,*}, Stephan Blaha^a, Zsanett Pintér^a, Robert Farla^a, Takaaki Kawazoe^a, Nobuyoshi Miyajima^a, Katsuyoshi Michibayashi^b and Tomoo Katsura

^a Bayerisches Geoinstitut, University of Bayreuth, 95440 Bayreuth, Germany.

^b Institute of Geosciences, Shizuoka University, Shizuoka 422-8529, Japan.

3.1 Abstract

Dislocation recovery experiments were conducted on pre-deformed olivine single crystals at 1,450 to 1,760 K, room pressure, and oxygen partial pressures near the Ni-NiO buffer to determine the annihilation rates for [100] and [001] dislocations on the (010) plane. Olivine single crystals were first deformed to activate the desired slip systems under simple shear geometry and then annealed at target conditions. The edge and screw dislocations with Burgers vectors, \mathbf{b} , of [100] and [001], respectively, both elongated in the [001] direction were produced by the deformation. The dislocation annihilation rate constants of both types of dislocations are identical within 0.3 log unit. The activation energies for both dislocations are also identical, i.e., ~400 kJ/mol, which is also identical to that of the Si self-diffusion coefficient. This correspondence suggests that olivine dislocation creep controlled by a diffusion-controlled process under low-stress and high-temperature conditions. This study offers a potential insight into the formation of AG-type fabric in olivine.

3.2 Introduction

Formation of lattice preferred orientation (LPO) in mantle minerals is a consequence of

the dominant slip systems activated by dislocation creep. Dominant slip system changes depending on chemical and physical conditions (Karato, 2008). Therefore, knowledge of conditions of LPO formation is useful to understand the chemical and physical conditions in the Earth's interior. In addition, LPO causes seismic anisotropy, which provides insight into the direction of upper mantle convective flow by combining observations about seismic anisotropy and conditions of formation of LPO in mantle minerals.

A number of seismic studies have shown seismic anisotropy in the upper mantle (Dziewonski and Anderson, 1981; Montagner and Kennett, 1996; Gung et al., 2003; Nettles and Dziewonski, 2008; Visser et al., 2008). These studies showed that the magnitude of seismic anisotropy decreases with depth. For example, the frequently cited one-dimensional global model, PREM (Dziewonski and Anderson, 1981), demonstrated that anisotropy in V_s and V_p gradually diminishes with depth. Montagner and Kennett (1996) suggested that horizontally polarized S-wave velocity (V_{SH}) is faster than vertically polarized S-wave velocity (V_{SV}) at the shallow part (< 250 km) of the upper mantle, but this difference decreases with depth. Visser et al. (2008) reported similar results.

Since olivine is the most abundant mineral in the Earth's upper mantle, the LPOs of olivine from natural specimens and experimentally deformed samples have been extensively studied (Karato, 1988; Jung et al., 2001; Katayama et al., 2004; Jung et al., 2006; Katayama et al., 2006). An abundance of olivine in peridotite, originating from the deep lithosphere and upper mantle, shows concentrations on the a -axis in the direction of lineation and b -axis in the direction normal to the foliation (e.g., Ben Ismail & Mainprice, 1998; Nicolas et al., 1971; named as A-type fabric after Jung and Karato, 2001). Peridotites from convergent boundaries (e.g., Dobrzhinetskaya et al., 1996; Mizukami et al., 2004; Skemer et al., 2006) show concentrations on the c -axis in the direction of lineation and the b -axis in the direction normal to the foliation (named as B-type fabric after Jung and Karato, 2001). AG-type fabric (Ben Ismail and Mainprice 1998, categorized by Mainprice, 2007), in which the a - and c -axes show a girdle structure parallel to the foliation with concentration on the b -axis normal to the foliation, were also found in upper mantle samples. (Michibayashi and Mainprice, 2004;

Hidas et al, 2007; Satsukawa et al., 2011). These natural olivine fabrics have been reproduced in deformation experiments under different chemical and physical conditions (Jung and Karato, 2001; Holtzman et al., 2003; Karato, 2008). A-type fabric forms under high-temperature conditions and B-type fabric forms under low-temperature and/or high-stress conditions (Jung and Karato, 2001; Karato, 2008). AG-type fabric forms with coexistence of melt (Holtzman et al., 2003).

However, we note that olivine LPO fabrics obtained in the laboratory generally formed under higher stresses and many orders of magnitude higher strain rates (Hirth and Kohlstedt, 2003). Competition between dislocation glide and climb and slip system activation under those conditions may not be the same as under low stress, moderate to high temperature conditions in the Earth. Therefore, it is necessary to investigate the origin of these fabrics using a different strategy.

Orowan's equation (Hull and Bacon, 2005) is a simple formula to describe dislocation creep, in which the dislocation creep rate is a product of the Burgers vector, average mobile dislocation density, and average mobile dislocation velocity. Generally, the average mobile dislocation velocity is the product of average dislocation mobility, which is independent of force, and a function of force acting on dislocations per unit length. Therefore, compared with dislocation velocity, dislocation mobility is more representative to express the rheology property of a material. This study focuses on variations in climb mobility in edge dislocation and cross slip mobility in screw dislocations, among different slip systems as function of temperature. Although glide velocity contribute much larger to the total strain, the climb/cross slip velocity is typically much slower than glide velocity. Therefore, dislocation climb/cross slip are the rate limiting process for olivine deformation (Poirier and Vergobbi, 1977) and should control the temperature and pressure dependence of strain rate. Thus, whether temperature and pressure can cause fabric transition is determined by the temperature and pressure dependences of climb/cross slip in different slip systems. Since climb and cross slip are controlled by thermal activated processes, we investigate the temperature dependence of them in two different slip systems. Hereafter, we use dislocation mobility to refer dislocation

climb/cross slip mobility and use dislocation motion to refer climb in edge dislocation and cross slip in screw dislocation.

Dislocation recovery is one experimental technique to estimate dislocation mobility. In this technique, a sample containing a certain dislocation density is annealed under hydrostatic conditions, causing a reduction in dislocation density due to annihilation. The rate constant of dislocation annihilation should be proportional to the dislocation mobility. The primary advantage of this technique is that no external stresses, which are many orders of magnitude higher in deformation experiments than in natural conditions, are applied. Hence, the physical environment in annealing experiments is more representative of the mantle than those in the deformation experiments. Another advantage of this method is that it allows much wider physical and chemical conditions than the deformation experiments, making it possible, for example, to precisely determine temperature dependence. Strictly speaking, the dislocation annihilation rate is not identical to the dislocation velocity in dislocation creep, because the driving force of dislocation annihilation is the internal stress field created by dislocations themselves, whereas the dislocation motion in dislocation creep is driven by external stresses. However, we assume that the temperature derivatives over their absolute values are identical between the dislocation motions by annihilation and the creep. In other words, the activation energies are identical for these two cases.

The A-, B-, and AG-type fabrics are the most common fabrics in nature and should be produced by the [100](010) slip system, which is called *a*-slip in this study, and/or the [001](010) slip system, which is called *c*-slip in this study. Therefore, we conducted dislocation recovery experiments on oriented single crystal olivine deformed producing *a*- and *c*-slips at ambient pressure and temperatures of 1,455 to 1,763 K. The experimental results obtained in this study provide information on the temperature dependence of dislocation mobility for the most important olivine slip systems. They also offer insights into the nature of dislocation motion under low-stress conditions. Although there are many studies on dislocation recovery of olivine at high temperatures and pressures (Goetze and Kohlstedt, 1973; Kohlstedt et al., 1980; Karato and Ogawa, 1982; Karato et al., 1993; Farla et al., 2011),

there is currently no study to compare dislocation annihilation rates and their temperature dependences between *a*- and *c*-slip systems. Therefore, this study provides unique data to investigate dislocation processes in the upper mantle rheology.

3.3 Experimental Procedures

Sample Preparation

The samples used in this study are single crystals of natural olivine from Pakistan. The same olivine has been describe by Gose et al., (2010) and the major and trace element, including water content, of the olivine has been reported there. The b-axis orientation of each crystal was determined using a Huber single-crystal diffractometer operated by SINGLE2014 (Angel et al. 2011). The oriented olivine crystals were mounted in epoxy resin with the (010) plane exposed to the surface and then polished using diamond powder with a grain size of 0.25 μm . The [100] and [001] directions were determined via electron backscattered diffraction (EBSD) in the scanning electron microscope (SEM). Cubes with 1.5 mm edge length were shaped from the oriented crystal along its crystallographic planes. The orientations of the crystals were checked again by EBSD after shaping the crystals. For the next step, inclusion- and crack-free cubes were handpicked under an optical microscope.

Production of high dislocation densities

High dislocation densities with dislocations of either [100] or [001] Burgers vector on the (010) plane were produced by experimental deformation in a Kawai-type multi-anvil apparatus at a pressure of 3 GPa and a temperature of 1,600 K. Fig. 1 shows the experimental setup. A cubic hole was made at the center of an MgO slice to accommodate the cubic olivine crystal in a unique orientation. The MgO slice with the olivine crystal was sandwiched between two crushable alumina pistons, cut at an angle of 45° for simple shear deformation of the olivine single crystal. The shear geometry was in the [100] or [001] direction on the (010) plane for

producing dislocations from the *a*- or *c*-slips, respectively. The sample and pistons were placed in a Pt tube, and another two columns of crushable alumina were placed on both ends of the inner crushable alumina pistons. Tungsten carbide anvils with 17 mm truncated edge lengths were used to generate high pressure together with a Cr₂O₃-doped MgO octahedron with a 25 mm edge length as a pressure medium. The furnace comprises a stepped cylindrical graphite heater and a ZrO₂ thermal insulator. Sample pressures were estimated from the hydraulic oil pressure based on calibrations using the phase transitions of Bi and Mg₂SiO₄ polymorphs. Temperatures were measured using a W97%Re3%-W75%Re25% thermocouple whose junction was located near the end of one of the alumina pistons.

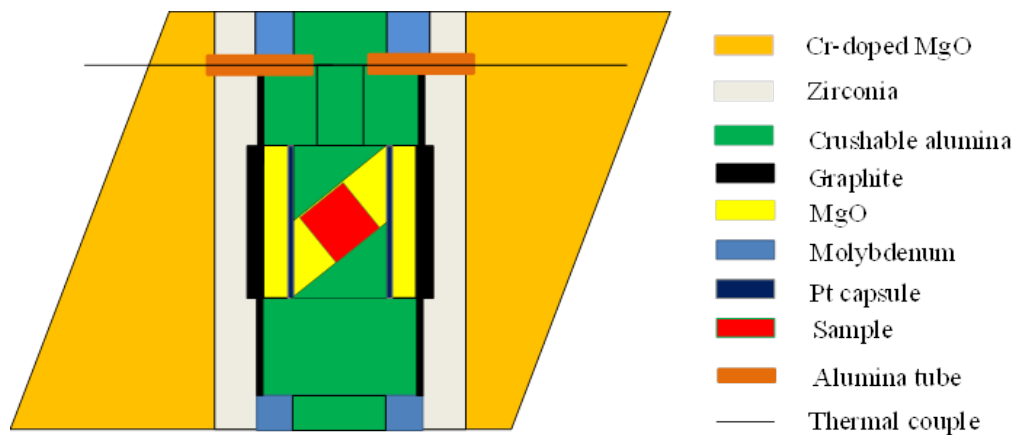


Figure 1. The sample assembly used in the multi-anvil high-pressure deformation experiments.

The cell assembly was first pressurized to 3 GPa using a press load of 3.7 MN at ambient temperature for 2 hours. The temperature was then increased to 1,600 K for 15 min. The target temperature and press load were kept constant for 15 min to sinter the crushable alumina. The sample was then further compressed to a press load of 3.9 MN for 15 min to deform the sample. After deformation, the sample was quenched by switching off the heating power, and then decompressed to ambient pressure for more than 16 hours.

After decompression, the pressure medium with the sample was polished to expose the (010) plane of the olivine crystal to examine the deviation of the crystallographic orientation from the shear direction via EBSD. The shear direction was determined using the

long axis of the MgO slice. The deviations were found to be less than 3° (Fig. 2).

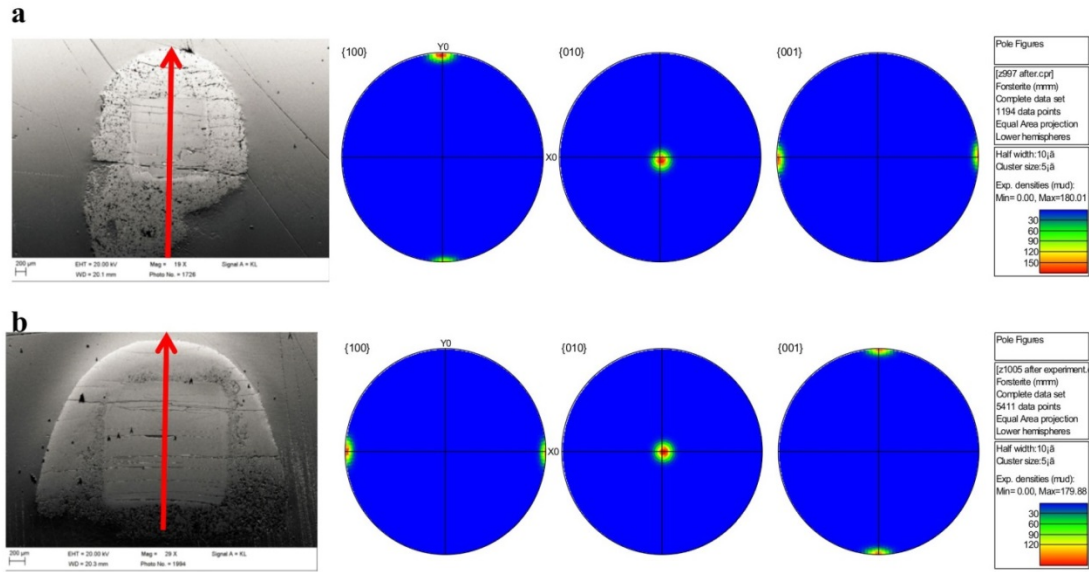


Figure 2. Relations between the crystallographic orientation and shear direction for (a) a-deformed olivine and (b) c-deformed olivine. The red arrows show the shear direction. The deviations in crystallographic orientation from the shear directions are less than 3° .

Dislocation annihilation by annealing

Each deformed olivine crystal was cut into eight cubic pieces. At early stages of this study, one of them was used to determine the initial dislocation density and the others were used for annealing experiments. Later, in order to minimize the uncertainty in annihilation rate constant caused by heterogeneous distribution of initial dislocations, four pairs were made from the eight pieces, where each piece shared a common (001) plane. One piece from each pair was used to determine the initial dislocation density, while the other was used to determine it after the annealing. The annealing experiment was conducted at ambient pressure and temperatures of 1,460-1,760 K for 20 min to 24.5 hours using a gas mixing furnace. Oxygen partial pressure was controlled at 10^{-6} - 10^{-8} MPa, which was near the Ni-NiO buffer, using a CO-CO₂ gas mixture. Table 1 summarizes the conditions of the annealing experiment.

Measurement of dislocation density

Dislocations were observed using the oxidation decoration technique (Kohlstedt et al., 1976; Karato, 1987). For this method, the samples were first heated at a temperature of 1,170 K for 1 hour in air to oxidize dislocations. The sample surface was subsequently polished using 0.25 μm diamond powder to remove the surface Fe-oxide layer, and then observed in back-scattered electron images (BEI) by SEM at around 10 mm working distance, accelerating voltage of 10 kV, and aperture of 120 μm . Dislocations appeared as bright spots or lines by concentration of ferric iron produced by the oxidation in dislocation cores. For the paired sample, the corresponding areas in the initial and annealed pieces were observed to determine change in dislocation density caused by the annealing. We counted the [100](010) edge dislocations and [001](010) screw dislocations in *a*- and *c*-slip sample, respectively on (001) plane. On this plane, these dislocations intersect orthogonally and appear as dot contrast. The dislocation density was calculated from the number of intersecting dislocations per area following Karato et al. (1993). This method allows us to avoid the geometrical complications of dislocation density measurements taken as cumulative line lengths per unit volume. The number of dots was determined using ImageJ image processing software (<http://rsbweb.nih.gov/ij/>). We applied a contrast threshold and then automatically counted the number of particles/dislocations per area. If the raw images were not sharp enough for the software to identify the dislocations as individual particles, we manually counted the number of dislocations.

TEM observation

In order to identify the nature of the dislocations produced by *a*- and *c*-slips, two additional deformation runs were conducted (Z1031 and Z1054), and analyzed via transmission electron microscopy (TEM). The samples were double side polished with thicknesses ranging from 23 to 35 μm and fixed on glass slides. After removing the selected olivine grains from the glass slide, an Ar ion-milling method was used to make the sample

thinner, using 4.5-5 kV voltages, 4-8° angles from top and bottom ion-bombardment, and total thinning times varying between 14 to 25 hours depending on the thicknesses and size of each sample. TEM observations were performed using Philips CM20FEG TEM, operating at 200 kV. Dislocation microstructures were examined by dark field (DF, Bragg condition, deviation parameter, $s = 0$) and weak-beam dark field (WBDF, $s > 0$) imaging and selected area electron diffraction (SAED). We chose diffraction vectors with $\mathbf{g} = 400$ and 004 to observe dislocations with Burgers vectors $\mathbf{b} = [100]$ and $[001]$ on the (010) plane, respectively. When $\mathbf{g} \cdot \mathbf{b} = \text{integer}$, dislocations are visible by diffraction contrast.

Data reduction

Because dislocation annihilation should occur through coalescence of two dislocations with opposite signs, the dislocation annihilation rate is expected to be proportional to the dislocation density squared (Li, 1966; Toriumi and Karato, 1978). The fundamental equation for the dislocation annihilation is therefore:

$$\frac{d\rho}{dt} = -k \cdot \rho^2 \quad (1)$$

where ρ is the dislocation density, $d\rho/dt$ is annihilation rate, k is the annihilation rate constant.

By solving this equation, we have

$$k = \frac{\frac{1}{\rho_f} - \frac{1}{\rho_i}}{t}, \quad (2)$$

where ρ_f and ρ_i are the dislocation density after and before annealing, respectively, and t is the annealing time. Because of the thermally activated process, the dislocation annihilation rate constant follows an Arrhenius relationship:

$$k = k_0 \exp\left(-\frac{E}{RT}\right) \quad (3)$$

where k_0 is a constant, E is the activation energy of the dislocation annihilation, T is the temperature, and R is the gas constant. As mentioned previously, E is also considered identical to the activation energy of the dislocation climb/cross slip.

3.4 Results

Table 1 shows the experimental results together with the annealing conditions. Figure 3 shows BEIs of the decorated dislocations after deformation and before annealing. These images show that dislocations appear mainly as dots on the (001) plane and mainly as lines on the (100) plane in both slip directions. That is, the dislocation lines are elongated in the [001] direction in both slip systems. For this reason, the dislocation densities are counted using the images on the (001) plane in both kinds of samples. Because the slip directions are [100] and [001] in the *a*- and *c*-slips, respectively, the dislocations produced by these slip systems should be [100] edge and [001] screw dislocations, respectively. Hereafter, the dislocations produced by the *a*- and *c*-slips are called *a*- and *c*-dislocations, respectively.

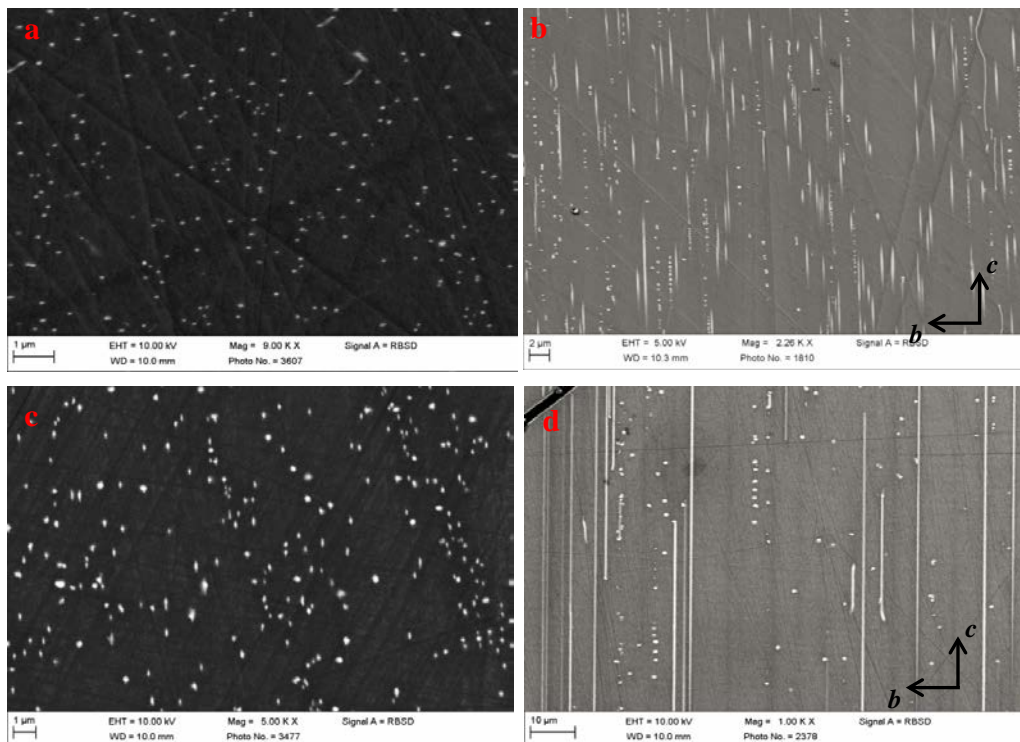


Figure 3. BEIs showing the initial dislocation structures. The crystallographic axes are shown by arrows in b) and d). a) *a*-deformed sample on the (001) plane. b) *a*-deformed sample on the (100) plane. c) *c*-deformed sample on the (001) plane. d) *c*-deformed sample on the (100) plane.

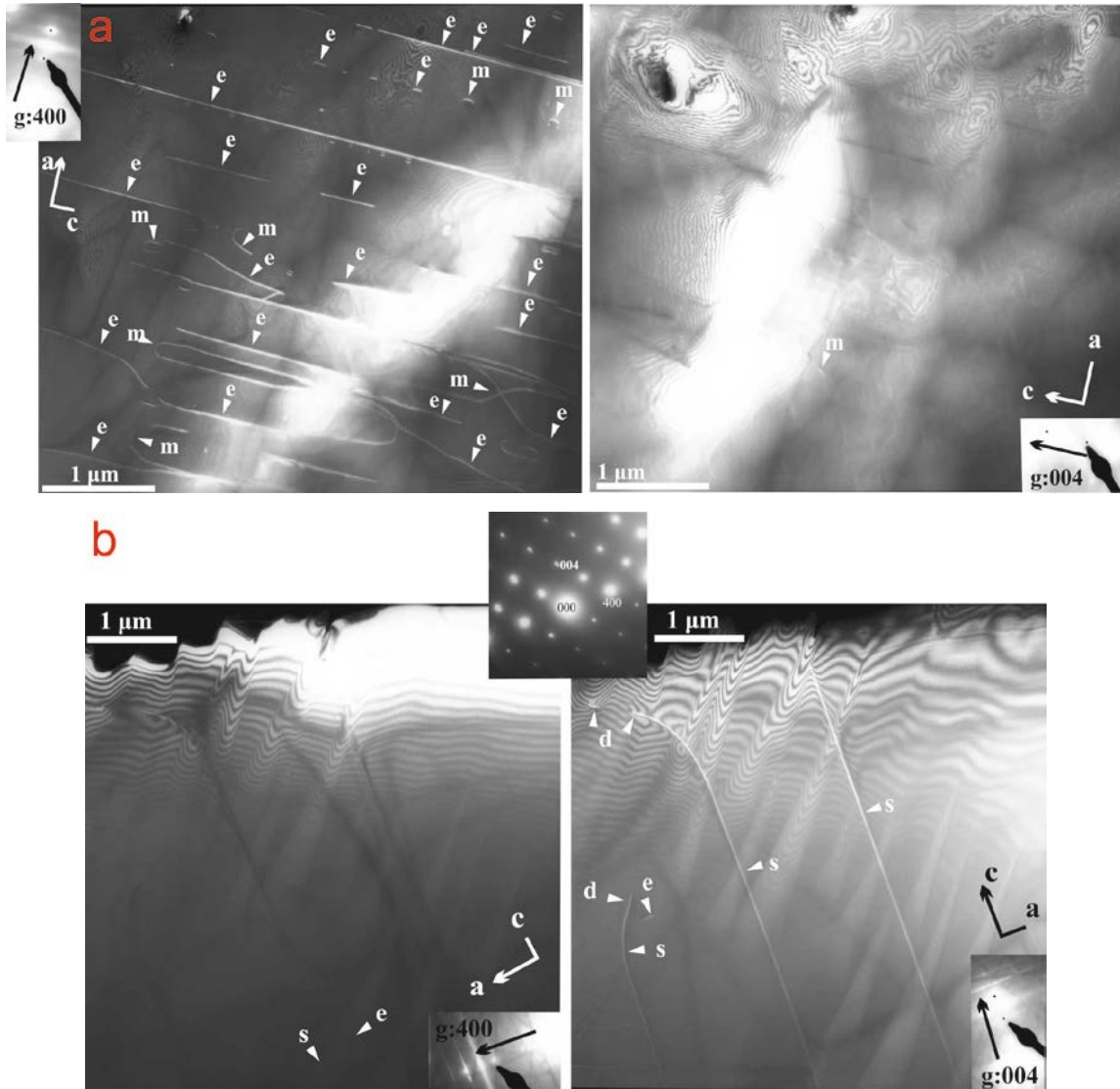


Figure 4. TEM images showing the initial dislocation structures. a) WBDF images with $g = 400$ (left) and $g = 004$ (right) showing microstructures of a-slip sample (Z1054). Insets are SAED patterns showing the diffraction condition and the main axes (top left and bottom right) in the WBDF conditions. e: edge, m: mixed, s: screw dislocations. b) WBDF image with $g = 400$ (left) and $g = 004$ (right) showing microstructures of c-slip sample (Z1031). Insets are SAED patterns showing the nearest zone axis (on top) and the diffraction conditions with the principal crystal axes (bottom right) in each WBDF image.

TEM observations confirmed the presence of mainly *a*- or *c*-dislocations in the crystals deformed in the $[100]$ or $[001]$ shear directions, respectively (Fig. 4). We measured the length of edge and screw dislocations and assuming the thickness of the TEM foil as 100 nm to

calculate the dislocation density. We also use Ham's (1961) method to measure the density of edge and screw dislocation. For the *a*-slip sample (Z1054), 93% of the dislocations were found to have Burgers vector in the [100] direction, 74% of which were edge dislocations (Fig. 4b) with the dislocation density as $1.4\mu\text{m}^{-2}$ (using total length of the edge dislocation divided by volume) and $1.6\mu\text{m}^{-2}$ (using Ham, 1961 method). For the *c*-slip sample (Z1031), 94% of the dislocations were found to have Burgers vector of [001], 57% of which were screw dislocations (Fig. 4a), with the dislocation density as $0.12\mu\text{m}^{-2}$ (using total length of the screw dislocation divided by volume) and $0.26\mu\text{m}^{-2}$ (using Ham, 1961 method).

The water content of olivine after deformation is below the detection limit by infrared spectroscopy. We didn't determine the water content after annealing, expecting it is nearly zeros since the annealing was held at room pressure and high temperature.

Fig. 5 shows the decorated dislocations after annealing. The decrease in dislocation density and formation of dislocation arrays were observed after annealing (Fig 5a). Changes in dislocation density in areas away from the dislocation arrays were measured to prevent the formation of the dislocation arrays from influencing the dislocation annihilation. The curved dislocation structures after annealing suggest that dislocation climb occurred during recovery for edge dislocations (Fig. 5b). The bent dislocation lines (Fig. 5c) indicate that cross slip occurred during recovery of screw dislocations.

Figure 6 plots the logarithmic of rate constant of dislocation annihilation against the reciprocal temperature. The results from the previous dislocation recovery experiments on olivine single crystal are also plotted in this figure. The dislocation annihilation rate constant of *a*-dislocations and *c*-dislocations are comparable, but those for the *c*-dislocations are half an order of magnitude higher than those for the *a*-dislocations. The temperature dependences of the dislocation annihilation rate constants for the *a*- and *c*-dislocations are identical. The activation energies calculated for the dislocation annihilation rate constant, which in this study are considered identical to those of the dislocation mobility, are $E_a = 400 \pm 20$ and $E_c = 400 \pm 30$ kJ/mol for *a*- and *c*-dislocations, respectively.

Table 1. Summary of experiment results.

[100](010) edge dislocation						
Sample	T (K)	Annealing time (h)	$\log(f_{O_2}, 10^{-5}$ Pa)	ρ_i (μm^{-2})	ρ_f (μm^{-2})	$\log(k, \text{m}^2\text{s}^{-1})$
Z1238-1 [#]	1763	0.4	-4.9	0.23±0.08	0.15±0.01	-14.8±0.3
Z997-1*	1748	0.3	-4.9	2.13±0.25	0.79±0.19	-15.2±0.2
Z1238-2 [#]	1673	2.5	-5.7	0.19±0.03	0.15±0.03	-15.8±0.5
Z1238-3 [#]	1573	11.5	-6.6	0.21±0.05	0.17±0.04	-16.5±0.7
Z997-2*	1553	1.3	-6.6	2.13±0.25	1.81±0.15	-16.8±0.4
Z997-3*	1455	24.5	-7.7	2.13±0.25	1.17±0.05	-17.4±0.1
[001](010) screw dislocation						
Sample	T (K)	Annealing time (h)	$\log(f_{O_2}, 10^{-5}$ Pa)	ρ_i (μm^{-2})	ρ_f (μm^{-2})	$\log(k, \text{m}^2\text{s}^{-1})$
Z1240-1 [#]	1763	0.4	-4.9	0.19±0.06	0.08±0.02	-14.3±0.2
Z1005-1*	1748	0.5	-4.9	0.76±0.07	0.15±0.04	-14.6±0.1
Z1240-2 [#]	1673	2.5	-5.7	0.36±0.18	0.07±0.02	-14.9±0.1
Z1005-2*	1648	3	-5.7	0.76±0.07	0.10±0.04	-15.1±0.2
Z1240-3 [#]	1573	11.5	-6.6	0.31±0.06	0.12±0.03	-15.9±0.2
Z1240-4 [#]	1473	25	-7.7	0.31±0.19	0.21±0.03	-16.8±0.6
Z1005-3*	1455	24	-6.6	0.76±0.07	0.33±0.07	-16.7±0.2

* The experimental runs from which one of the deformed piece was used to determine the initial dislocation density while others used to determine the dislocation density after annealing.

[#] The experimental runs from which one a pair of deformed pieces with common (001) plane were used to determine initial and annealed dislocation density. Explanation see text.

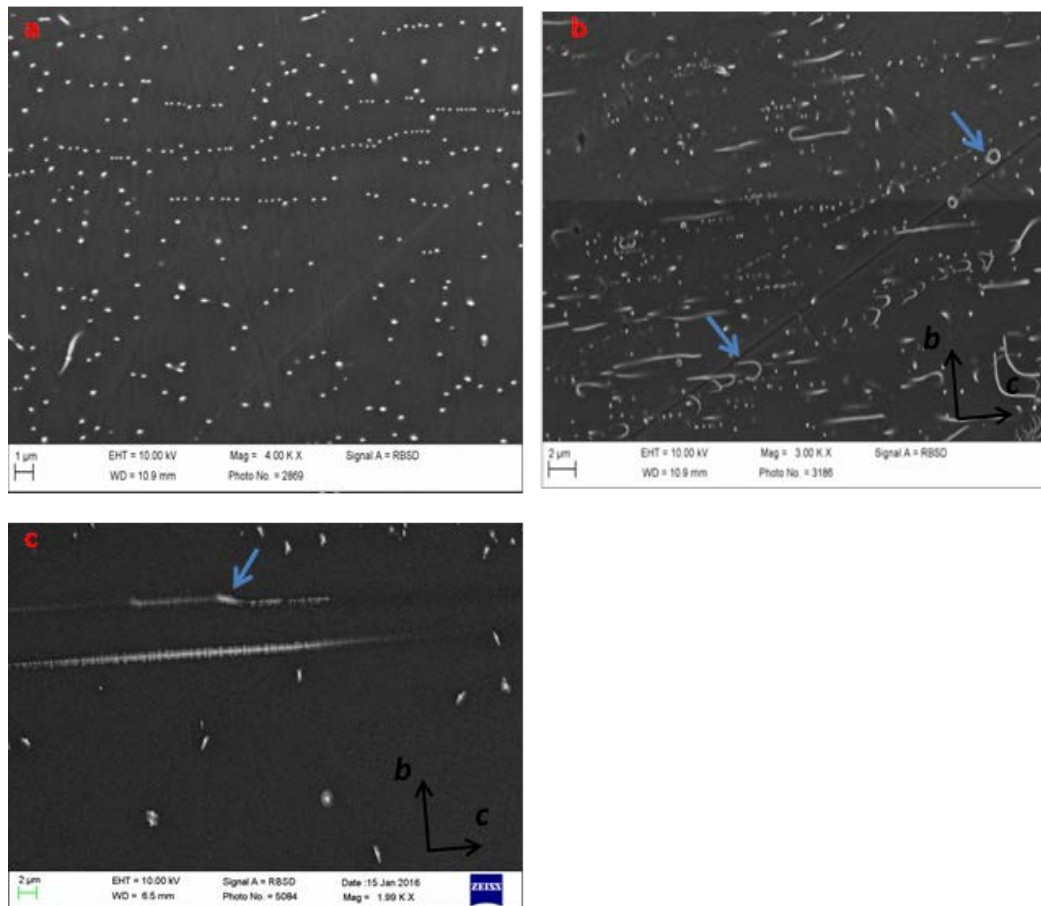


Figure 5. BEIs showing the dislocation structures after annealing. a) a-deformed sample annealed at 1,748 K for 20 min on the (001) plane. Alignment of edge dislocations occurred. b) a-deformed sample annealed at 1,400 °C for 20 min observed on the (100) plane. Larger arrows indicate curved dislocation and dislocation loop. The crystallographic axes are shown by smaller arrows in b). c) c-deformed sample annealed at 1,490 °C for 25 min observed on the (100) plane. The arrow points to a bent dislocation line indicating cross slip occurred during annealing. The crystallographic axes are shown.

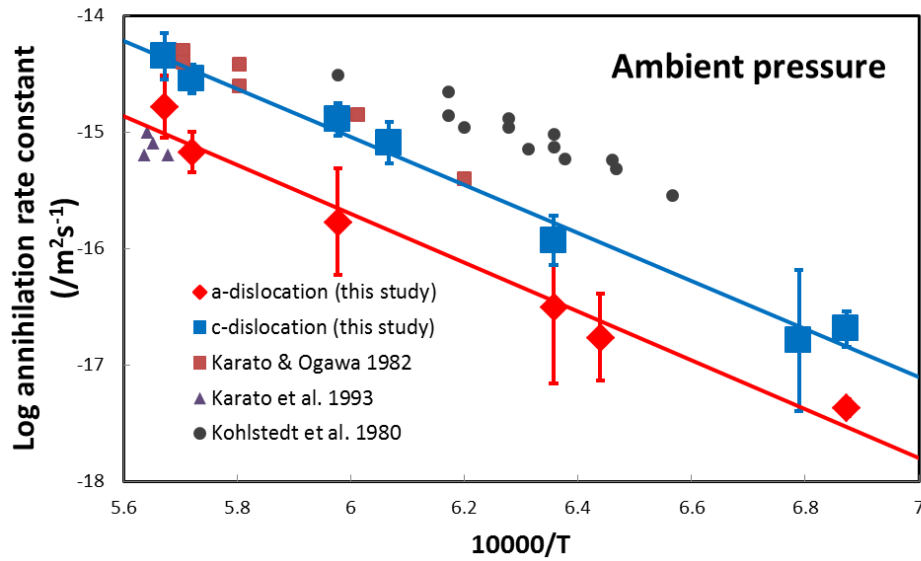


Figure 6. Logarithmic dislocation annihilation rate constant of *a*- and *c*-dislocations (red diamonds and blue squares, respectively) versus the reciprocal temperature. No transition between *a*- and *c*-slip dislocation mobility occurs. Black circles: Kohlstedt et al. (1980); brown squares: Karato and Ogawa (1982); violet triangles: Karato et al. (1992).

3.5 Discussion

Comparison with previous studies

Karato and Ogawa (1982) obtained an activation energy of 400 ± 60 kJ/mol for the dislocation annihilation rate constant. This value is reproduced in this study. The experiment by Kohlstedt et al. (1980) gave an activation energy of 300 ± 15 kJ/mol for the annihilation rate constant of natural and deformed olivine single crystal. However, we notice that the temperature range in Kohlstedt et al. (1980) was only 150 K. Karato et al. (1993) studied the pressure dependence of dislocation mobility, in which they adopted a similar activation energy (290 kJ/mol) to correct the difference in temperature conditions for their data points. Farla et al. (2011) gave an activation energy of 355 ± 81 kJ/mol for annihilation rate constant on San Carlos olivine polycrystals, which also agree to the present results within the margin of error.

The rate constants of *a*-dislocations from this study are comparable with those from

Karato et al. (1993), which used the same technique to study the recovery of *a*-dislocations. The results from Kohlstedt et al. (1980) and Karato and Ogawa (1982) are similar to or slightly higher than the rate constants of *c*-dislocations in this study. Although the dislocation characters were not characterized in these studies, both *a*- and *c*-dislocations should be present because their samples were deformed in the $[101]_c$ direction. Therefore, the values of previous single crystal work should reflect the average rate constant for both slip systems. The somewhat larger rate constants may be due to the different techniques employed to observe dislocations in their studies (TEM by Kohlstedt, 1980, optical microscopy by Karato and Ogawa 1982). The TEM method is restricted by the limited sampling area, which cannot give a statistical average when calculating dislocation density. Optical microscopy potentially underestimates dislocation density when it is high, which applies equally to the initial and annealed dislocation densities, resulting in a lower annihilation rate constant through Eq. 2 (Farla et al., 2011). The rate constants obtained from polycrystalline olivine by Farla et al. (2011) are two orders of magnitude lower than those in this study. This might be due to pinning the dislocation on grain boundaries and tangling dislocations of different types in their experiments.

The olivine single crystal starting material used in this study is not mantle origin and the trace element abundance is somewhat different from mantle derived olivine (Gose et al., 2010). However, the similar annihilation rate constant of our study and Karato et al, 1993 (See our Fig.6) indicate dislocation interactions and annihilation, which is defect assisted, does not change significantly between Pakistan olivine and San Carlos olivine. In addition, the water content after deformation is below the detect limit of infrared spectrometry. Therefore, we do not think the composition difference between the olivine we used and mantle derived olivine alter the results.

Comparison of results with other techniques

The microstructures of dislocation after annealing indicate climb occurred for edge dislocation and cross slip occurred for screw dislocation. In addition, since they are the slower

process compared to dislocation glide, we think the activation energy we obtain for annihilation represent that of dislocation climb for *a*-dislocation and cross slip for *c*-dislocation. The activation energies obtained in this study are identical to that for the Si self-diffusion given by Fei et al. (2012) (410 ± 30 kJ/mol), within the margin of error. The identical activation energies for dislocation mobility and Si diffusion suggest that the dislocation climb in edge dislocation and cross slip in screw dislocation in dislocation recovery are controlled by Si self-diffusion. The identical activation energies for both *a*- and *c*-dislocations also support this idea.

In contrast, deformation experiments on dry polycrystalline olivine typically yield higher activation energies, namely about 500 kJ/mol (Goetze, 1978; Karato and Jung, 2003; Hirth and Kohlstedt, 2003), than those of dislocation mobility (this study; Kohlstedt, 1980; Karato and Ogawa, 1982; Karato et al., 1993; Farla et al., 2011). This discrepancy suggests that dislocation creep in the deformation experiments is likely driven by a combination of mechanisms. The stress levels in the deformation experiment are generally higher, in the order of 100 MPa to 1 GPa, and the deformation mechanism in such experiments is at the boundary of Peierls mechanism and the dislocation power law creep (e.g., Jung and Karato, 2001; Karato and Jung, 2003). Therefore, dislocation glide should be a significant component in the deformation experiments, but not in the dislocation recovery experiments.

Geophysics application

Whether temperature can cause the fabric transition between A- and B- type is determined by the activation energy of creep caused by *a*-dislocation and *c*-dislocation, which are constrained by the rate limiting process of *a*- and *c*-dislocation movement, i.e. climb or cross-slip. We found the same activation energy for the annihilation rate of *a*- and *c*-dislocation and think they represent the activation energy of dislocation climb and cross slip for *a*- and *c*-dislocations. Therefore, the fabric transition between A- and B-type cannot be caused by temperature.

In order to investigate the strain rate caused by *a*- and *c*-dislocations, we need to know the relationship between the dislocation climb (cross slip) velocity and the average dislocation velocity. The function of force ($f(force)$) which acting on the dislocation per unit length is also need to link the dislocation climb (cross slip) mobility (k), which is investigated in this study, and climb (cross slip) velocity (v), since

$$v = k \cdot f(force) \quad (4)$$

Recent work on simulation of dislocation movement in olivine (Boioli et al, 2015) suggested a constant ratio between dislocation glide velocity and average mobile dislocation velocity. However, we noticed that at low stress condition (less than 5 MPa in their Fig. 9), their average mobile dislocation velocity is nearly the same as climb velocity. Therefore, we can use dislocation climb velocity to represent average mobile dislocation velocity at low stress conditions when climb is the rate limiting process for creep. If we assume that dislocation cross slip velocity is also similar to the average mobile dislocation velocity at low stress conditions when cross slip is the rate limiting process for creep, and the force function is the same for climb and cross slip process, the strain rate produced by *a*- and *c*-dislocation would be same. Therefore, at such conditions, we can use our result to infer the creep caused by *a*- and *c*-dislocations at low stress conditions. Here, we emphasize that only when the two assumptions are met, 1) dislocation cross slip velocity is similar to the average mobile dislocation velocity at low stress conditions when cross slip is the rate limiting process for creep. 2) The force functions are the same for climb and cross slip are the same, can we use our result to infer the strain rate caused by these two slip systems.

In low-stress regions, such as oceanic mantle (0.1 to 1 MPa, Hirth and Kohlstedt, 2003), we assume that the two assumptions mentioned above are met and then the strain rate caused by *a*- and *c*-slips should be comparable mobile in the deformation of olivine in oceanic mantle and, accordingly, the AG-type fabric could dominate. Indeed, some natural mantle rocks, such as olivine from the Hilti mantle section (Michibayashi & Mainprice, 2004) and olivine from the

Pannonian Basin (Hidas et al., 2007), show AG-fabric. Recently, Tommasi and Vauchez compiled the LPOs of natural olivine and showed a considerable amount of AG-fabric (Tommasi and Vauchez, 2015). This further confirms the existence of the AG-type fabric. Such fabric could be formed by the non-coaxial flow in the lithospheric mantle, close to Moho (Hilti mantle section after Michibayashi and Mainprice, 2004) or at the fossil lithospheric-asthenospheric boundary (Pannonian Basin, Hidas et al., 2007) or related to the type of strain (Higgins and Tommasi, 2012). The present results, however, provide a new insight to the formation of AG-type, i.e. it is due to the comparable dislocation mobility in the *a*- and *c*-slips at low stresses.

The dominance of AG-type fabric in the oceanic asthenosphere is also suggested by the seismic studies. The oceanic asthenosphere is not only characterized by azimuthal S wave anisotropy but also by stronger P wave and S wave radial anisotropy (e.g. Gung et al., 2003; Nettles and Dziewonski, 2008). However, none of the fabric shown in deformation experiment reproduces the comparably stronger radial anisotropy than azimuthal anisotropy (Song and Kawakatsu, 2012). Instead, the AG type olivine fabric can produce such character since the strong alignment of [010] axis and the diffusive distribution of [100] and [001] axis in the (010) plane. Assuming the elastic tensor of orthorhombic symmetry in the subducting oceanic asthenosphere, which can be produced by AG-type olivine fabric, the SKS splitting patterns across the fore-arc in central Alaska are well explained (Song and Kawakatsu, 2013). Although existing of horizontal melt layer in asthenosphere could enhance the radial anisotropy (e.g. Kawakatsu et al, 2009), these layer might solidify during subduction. Therefore, AG-type olivine fabric might be a potential candidate to explain the seismic anisotropy in the oceanic asthenosphere.

In high stress region, such as lithosphere and convergent boundaries, the average mobile dislocation velocity deviates a lot from dislocation climb velocity (Boioli et al., 2015) and we cannot use dislocation climb (cross-slip) velocity to represent average mobile dislocation velocity dislocation. Since glide contributes considerably to deformation, as in the deformation experiments, A- and B-type fabrics form.

The change from A- or B-type fabric to AG-type fabric with decreasing stress may provide a new explanation for the decrease in seismic anisotropy with depth. AG-type fabric produces weaker seismic anisotropy than A- or B-type fabric. Olivine has the highest P-wave velocity in the a -direction. For S waves, the highest velocity occurs when oscillation is in the a -direction. Therefore, A- or B-type fabric should produce strong P-wave azimuthal anisotropy. On the other hand, the AG-type fabric produces no or weak P-wave azimuthal anisotropy, because the direction of the a -axis is not concentrated, but distributed on the flow plane. A similar situation exists for S-wave anisotropy. Therefore, the decrease in seismic anisotropy with depth in the upper mantle down to 300 km depth might be caused by transition of olivine from A- or B-type to AG-type, due to decrease in stress with depth.

Finally, we must emphasize that our explanation about the origin of AG-type fabric is based on the two assumptions mentioned above, which need to be tested in the future. In addition, our result is based on the experiments conducted on the single crystal. The results might change in the case of polycrystalline material, which dislocation mobility might be influenced by grain boundary.

3.6 Conclusion

The present study shows that the dislocation annihilation rates for the [100](010) edge dislocation are slightly smaller than those for the [001](010) screw dislocation. The temperature dependences of climb in [100] edge dislocation and cross slip in [001] screw dislocations are identical: their activation energies are both 400 kJ/mol. Therefore, fabric transition due to temperature is unlikely. The identical activation energies of dislocation movement and Si self-diffusion suggest that the dislocation climb/cross slip is controlled by Si diffusion. The discrepancy between the activation energies for the deformation experiment and recovery experiment may be due to high stresses in deformation experiments. Under certain assumptions, we can use our result to infer the creep caused by a - and c -dislocations at low stress conditions. If so, under low-stress conditions, like the oceanic mantle, the AG-type fabric may dominate, while A- or B-type fabric forms under high-stress conditions, like the

lithosphere and convergent boundaries. The transition from A- or B-type fabric to AG-type fabric with decreasing stress may be the reason for the decrease in seismic anisotropy with depth.

3.7 Acknowledgements

We acknowledge F. Heidelbach and P. O'Brien for providing the olivine single crystals and T. Boffa-Ballaran for instructing the single crystal X-ray diffractometry. We thank technicians in BGI for the sample and assembly preparation. This research was supported by DFG grants to TK (KA3434/3-1, KA3434/7-1, KA3434/8-1 and KA3434/9-1) and by the annual budget of BGI.

3.8 References

- Angel, R. J., and L. W. Finger (2011), SINGLE: A program to control single-crystal diffractometers, *Journal of Applied Crystallography*, 44(1), 247-251.
- Ben Ismail W., Mainprice D., 1998. An overview of upper mantle fabrics and seismic anisotropy. *Tectonophysics* 296, 145–157.
- Boioli, F., Carrez, P., Cordier, P., Devincere, B., and Marquille, M. (2015) Modeling the creep properties of olivine by 2.5-dimensional dislocation dynamics simulations. *Physical Review B*, 92(1)
- Bussod, G. Y., Katsura, T., and Rubie, D.C., 1993. The large volume multi-anvil press as a high P-T deformation apparatus. *Pure Appl. Geophys.*, 141,579-599.
- Dobrzhinetskaya, L., Green II, H. W., & Wang, S. (1996). Alpe Arami: a peridotite massif from depths of more than 300 kilometers. *Science*, 271(5257), 1841.
- Dziewonski, A. M., & Anderson, D. L. 1981. Preliminary reference Earth model. *Physics of the earth and planetary interiors*, 25(4), 297-356.
- Farla, R.J.M., Kokkonen, H.K., Fitz Gerald, J.D., Barnhoorn, A., Faul, U.H., Jackson, J., 2011. Dislocation recovery in fine-grained polycrystalline olivine. *Phys. Chem. Minerals*. 38,

363-377.

- Fei, H., Hegoda, C., Yamazaki, D., Wiedenbeck, M., Yurimoto, H., Shcheka, S., Katsura, T., 2012. High silicon self-diffusion coefficient in dry forsterite. *Earth Planet. Sci. Lett.* 345, 95-103.
- Goetze, C., 1978. Mechanisms of creep in olivine. *Philos Trans R Soc Lond* 288(1350), 99-119.
- Goetze, G., Kohlstedt, D.L., 1973. Laboratory Study of Dislocation Climb and Diffusion in Olivine. *J. Geophys. Res.* 78, 5962-5970.
- Goetze, C., & Poirier, J. P. 1978. The mechanisms of creep in olivine and discussion. *Philosophical Transactions of the Royal Society of London. Series A, Mathematical and Physical Sciences*, 288(1350), 99-119.
- Gung, Y., Panning, M., & Romanowicz, B. 2003. Global anisotropy and the thickness of continents. *Nature*, 422(6933), 707-711
- Ham, R. K. 1961. The determination of dislocation densities in thin films. *Philosophical Magazine*, 6(69), 1183-1184.
- Hidas, K., Falus, Gy., Szabó, Cs., Szabó, P. J., Kovács, I. & Földes, T. 2007. Geodynamic implications of flattened tabular equigranular textured peridotites from the Bakony-Balaton Highland Volcanic Field (Western Hungary). *Journal of Geodynamics*, 43 (4-5), 484-503.
- Higgie, K., & Tommasi, A. 2012. Feedbacks between deformation and melt distribution in the crust–mantle transition zone of the Oman ophiolite. *Earth and Planetary Science Letters*, 359, 61-72.
- Holtzman, B. K., Kohlstedt, D. L., Zimmerman, M. E., Heidelbach, F., Hiraga, T., & Hustoft, J. 2003. Melt segregation and strain partitioning: implications for seismic anisotropy and mantle flow. *Science*, 301(5637), 1227-1230.
- Houlier, B., Cheraghmakani, M., & Jaoul, O. (1990). Silicon diffusion in San Carlos olivine. *Physics of the Earth and Planetary Interiors*, 62(3), 329-340.
- Jung, H., & Karato, S. I. 2001. Water-induced fabric transitions in olivine. *Science*, 293(5534),

1460-1463.

- Jung, H., Katayama, I., Jiang, Z., Hiraga, T., & Karato, S. I. 2006. Effect of water and stress on the lattice-preferred orientation of olivine. *Tectonophysics*, 421(1), 1-22.
- Jaoul, O., Poumellec, M., Froidevaux, C., & Havette, A. (1981). Silicon diffusion in forsterite: a new constraint for understanding mantle deformation. *Anelasticity in the Earth*, 95-100.
- Karato, S., 1987. Scanning electron microscope observation of dislocations in olivine. *Phys. Chem. Miner.* 14, 245–248.
- Karato, S., 2008. *Deformation of Earth Materials: Introduction to the Rheology of the Solid Earth*. Cambridge, UK: Cambridge Univ. Press. 462 pp.
- Karato, S., Jung, H., Katayama, I., Skemer, P., 2008. Geodynamic significance of seismic anisotropy of the upper mantle: new insights from laboratory studies. *Annu. Rev. Earth Planet. Sci.* 36, 59-95.
- Karato, S., Rubie, D.C., Yan, H., 1993. Dislocation recovery in olivine under deep upper mantle conditions: Implications for creep and diffusion. *J. Geophys. Res.* 98, 9761-9768.
- Karato, S., Sato, H., 1982. Effect of oxygen partial-pressure on the dislocation recovery in olivine—a new constraint on creep mechanisms. *Phys Earth Planet Inter* 28, 312–319.
- Karato, S., Wu, P., 1993. Rheology of the upper mantle: a synthesis. *Science* 260, 771–775.
- Karato S., Ogawa M., 1982. High-pressure recovery of olivine: implications for creep mechanisms and creep activation volume. *Phys. Earth. Planet Inter.* 28,102–117.
- Katayama, I., Jung, H., & Karato, S. I. 2004. New type of olivine fabric from deformation experiments at modest water content and low stress. *Geology*, 32(12), 1045-1048.
- Kawakatsu, H., Kumar, P., Takei, Y., Shinohara, M., Kanazawa, T., Araki, E., & Suyehiro, K. 2009. Seismic evidence for sharp lithosphere-asthenosphere boundaries of oceanic plates. *Science*, 324(5926), 499-502.
- Kohlstedt, D. L., Nichols, H. P. K., & Hornack, P. 1980. The effect of pressure on the rate of dislocation recovery in olivine. *Journal of Geophysical Research: Solid Earth* (1978–2012), 85(B6), 3122-3130.
- Kohlstedt, D.L., Evans, B., Mackwell, S.J., 1995. Strength of the lithosphere: constraints

- imposed by laboratory experiments. *J. Geophys. Res.* 100, 17587–17602.
- Kohlstedt, D. L., & Goetze, C. (1974). Low-stress high-temperature creep in olivine single crystals. *J. geophys. Res.*, 79(14), 2045-2051.
- Kohlstedt, D.L., Goetze, C., Durham, W.B., Vandersande, J., 1976. New technique for decorating dislocations in olivine. *Science*. 191, 1045–1046.
- Kohlstedt, D.L., Nichols, H.P.K., Hornack, P., 1980. The effect of pressure on the rate of dislocation recovery in olivine. *J. Geophys. Res.* 85, 3122-3130.
- Li, J.C.M., 1966. Recovery processes in metals, In: *Recrystallization, Grain Growth and Textures*. Am. Sot. Metals: 45-63.
- Mainprice, D. 2007. Seismic anisotropy of the deep Earth from a mineral and rock physics perspective. In: Schubert, G. (ed.) *Treatise on Geophysics*. Oxford: Elsevier, pp. 437–492.
- Michibayashi, K., Mainprice, D., 2004. The role of pre-existing mechanical anisotropy on shear zone development within oceanic mantle lithosphere: an example from the Oman ophiolite, *J. Petrol.* 45 (2), 405-414.
- Mizukami, T., Wallis, S. R., & Yamamoto, J. (2004). Natural examples of olivine lattice preferred orientation patterns with a flow-normal a-axis maximum. *Nature*, 427(6973), 432-436.
- Montagner, J. P., & Kennett, B. L. N. 1996. How to reconcile body-wave and normal-mode reference Earth models. *Geophysical Journal International*, 125(1), 229-248.
- Nettles, M., & Dziewoński, A. M. 2008. Radially anisotropic shear velocity structure of the upper mantle globally and beneath North America. *Journal of Geophysical Research: Solid Earth* (1978–2012), 113(B2).
- Nicolas, A., Bouchez, J.L., Boudier, F., Mercier, J-CC., 1971. Textures, structures and fabrics due to solid state flow in some European lherzolites. *Tectonophysics* 12, 55-86.
- Ohuchi, T., Kawazoe, T., Nishihara, Y., Nishiyama, N., & Irifune, T. 2011. High pressure and temperature fabric transitions in olivine and variations in upper mantle seismic anisotropy. *Earth and Planetary Science Letters*, 304(1), 55-63.
- Poirier, J. P., & Vergobbi, B. 1978. Splitting of dislocations in olivine, cross slip-controlled

- creep and mantle rheology. *Physics of the Earth and Planetary Interiors*, 16(4), 370-378.
- Ringwood, A.E., 1991. Phase-transformations and their bearing on the constitution and dynamics of the mantle. *Geochim. Cosmochim. Acta* 55 (8), 2083-2110.
- Satsukawa, T., Michibayashi, K., Anthony, E. Y., Stern, R. J., Gao, S. S., & Liu, K. H. 2011. Seismic anisotropy of the uppermost mantle beneath the Rio Grande rift: Evidence from Kilbourne Hole peridotite xenoliths, New Mexico. *Earth and Planetary Science Letters*, 311(1), 172-181.
- Skemer, P., Katayama, I., & Karato, S. I. (2006). Deformation fabrics of the Cima di Gagnone peridotite massif, Central Alps, Switzerland: evidence of deformation at low temperatures in the presence of water. *Contributions to Mineralogy and Petrology*, 152(1), 43-51.
- Song, T. R. A., & Kawakatsu, H. 2012. Subduction of oceanic asthenosphere: Evidence from sub - slab seismic anisotropy. *Geophysical Research Letters*, 39(17).
- Song, T. R. A., & Kawakatsu, H. 2013. Subduction of oceanic asthenosphere: A critical appraisal in central Alaska. *Earth and Planetary Science Letters*, 367, 82-94.
- Tommasi, A., & Vauchez, A. 2015. Heterogeneity and anisotropy in the lithospheric mantle. *Tectonophysics*.
- Toriumi, M., & Karato, S. I. 1978. Experimental studies on the recovery process of deformed olivines and the mechanical state of the upper mantle. *Tectonophysics*, 49(1), 79-95.
- Zhang, S., & Karato, S. I. 1995. Lattice preferred orientation of olivine aggregates deformed in simple shear. *Nature*, 375(6534), 774-777

4. Identical activation volumes of dislocation mobility in the [100](010) and [001](010) slip systems in natural olivine

Lin Wang*, Stephan Blaha, Takaaki Kawazoe, Nobuyoshi Miyajima and Tomoo Katsura

Bayerisches Geoinstitut, University of Bayreuth, 95440 Bayreuth, Germany.

4.1 Abstract

Dislocation recovery experiments were performed on pre-deformed olivine single crystals at pressures of 2, 7 and 12 GPa and a constant temperature of 1650 K to determine the pressure dependence of the annihilation rate constants for [100](010) edge dislocation (*a*-dislocation) and [001](010) screw dislocation (*c*-dislocation). The constants of both types of dislocations are comparable within 0.3 orders of magnitude. The activation volumes of *a*- and *c*-dislocations are small and identical within error: 2.7 ± 0.2 and 2.5 ± 0.9 cm³/mol, respectively. These values are slightly larger and smaller than those of Si lattice and grain-boundary diffusions in olivine, respectively. The small and identical activation volumes for the *a*- and *c*-dislocations suggest that the pressure-induced fabric transition is unlikely in the asthenosphere. The decrease in seismic anisotropy with depth down in the asthenosphere may be caused by the fabric transition from A-type or B-type to AG-type with decreasing stress with depth.

4.2 Introduction

A number of seismological studies showed anisotropy in seismic wave velocity in the Earth's upper mantle [Dziewonski and Anderson, 1981; Montagner and Kennett, 1996; Gung *et al.*, 2003; Nettles and Dziewonski, 2008; Visser *et al.*, 2008]. The upper-mantle seismic

anisotropy is interpreted by the lattice preferred orientations (LPO) and elastic anisotropy of olivine [e.g. *Karato*, 2012]. Some studies [e.g. *Gung et al.*, 2003; *Visser et al.*, 2008] depicted that the seismic anisotropy quickly decreases with increasing depth down to 300 km. The origin of this decrease is an issue of debate [e.g. *Karato* 1992; *Mainprice et al.*, 2005; *Raterron et al.*, 2009]. Since elastic anisotropy of minerals is essentially independent from physical and chemical conditions, the decrease in seismic anisotropy should be resulted from weakening or change in LPO patterns (i.e. fabric transition).

Formation of LPO is a consequence of movement of dislocations of the dominant slip system(s) in dislocation creep. Therefore, if the decrease in seismic anisotropy with depth is caused by the change in LPO pattern, the dominant slip system should change with pressure. Several deformation experiments [*Couvy et al.*, 2004; *Raterron et al.*, 2007, 2009; *Jung et al.*, 2009; *Raterron et al.*, 2011; *Ohuchi et al.*, 2011] showed that, although the transition pressure is under debate, the olivine fabric changes from A-type to B-type with increasing pressure. . These results imply that the dominant slip system would change from [100](010) to [001](010), which are hereafter called *a*- and *c*-slips, respectively, with depth. These articles explained the decrease in seismic anisotropy by this fabric transition. However, further investigation is necessary to verify this hypothesis because the stress magnitude in their deformation experiments are by many orders of magnitude higher than that in asthenospheric conditions [*Hirth and Kohlstedt*, 2003], which may change the rate-limiting process of dislocation creep [*Wang et al.*, 2016].

Our previous study [*Wang et al.*, 2016] provided a different explanation. We reported identical dislocation mobility between *a*- and *c*-dislocations in the recovery process in olivine along elevating temperatures at an ambient pressure. The result indicates that there is no clear dominance between these two slip systems under low-stress conditions. Based on these observations, we proposed a new hypothesis that the decrease in seismic anisotropy by the fabric transition from A- or B-type to AG-type with decreasing stress.

If the dislocation mobility of *a*- and *c*-slips has strong and different pressure dependence, *Wang et al.*'s [2016] hypothesis for the origin of the decrease in seismic anisotropy should be

reconsidered. Therefore, the pressure dependence of dislocation mobility of the *a*- and *c*-slip systems must be investigated. In this study, we conducted dislocation recovery experiments for *a*- and *c*-dislocations at various pressures and a constant temperature by a similar method to that of Wang *et al.* [2016] and determined the activation volumes of the annihilation rate constants for these two dislocations. As was the case in Wang *et al.* [2016], it is assumed that the average dislocation velocity is proportional to the dislocation mobility, which is proportional to the dislocation annihilation rate constant. Therefore, we can estimate the pressure dependences of the dislocation average velocity from those of dislocation annihilation rate constants. Our results show that the activation volumes are small and identical, and therefore, pressure cannot induce the fabric transition.

4.3 Experimental Procedures

The experimental procedure adopted in this study is similar to that of Wang *et al.* [2016] except two differences. One is that annealing was performed at high pressures of 2, 7 and 12 GPa and a constant temperature of 1650 K using a multi-anvil press, whose sample assembly is shown in Fig. 1. Two olivine single crystals in which *a*- and *c*-dislocations were activated respectively in preceding simple shear deformation experiments were loaded together in a Ni capsule. The simple shear deformation experiment setup and procedure can be found on Wang *et al.* [2016]. The dominance of *a*- and *c*-dislocation in the deformed sample were confirmed by previous study (Wang *et al.*, 2016). The deformed samples were surrounded by a mixture of Ni and enstatite powders with a volume ratio of 1:1 to produce a quasi-hydrostatic condition and fix the oxygen fugacity at the Ni-NiO buffer and the SiO₂ activity of $a_{\text{opx}} = 1$. In order to test the effect of cold compression to the dislocation multiplication, we check the dislocation density increase of an undeformed sample which was cold compressed in the same experimental setup to 12 GPa. The H₂O contents in the samples were measured vertically to the (001) plane by unpolarized FTIR spectroscopy before and after annealing based on the Paterson's (1982) calibration. The other difference is that paired olivine crystals, each of which shared a common (001) plane, were used to precisely determine change in dislocation density by annealing. One

piece from each pair was used to determine the initial dislocation density (as-crept piece), while the other was used to determine it after annealing (annealed piece). We counted dislocations in the corresponding areas of the paired as-crept and annealed pieces from the same group.

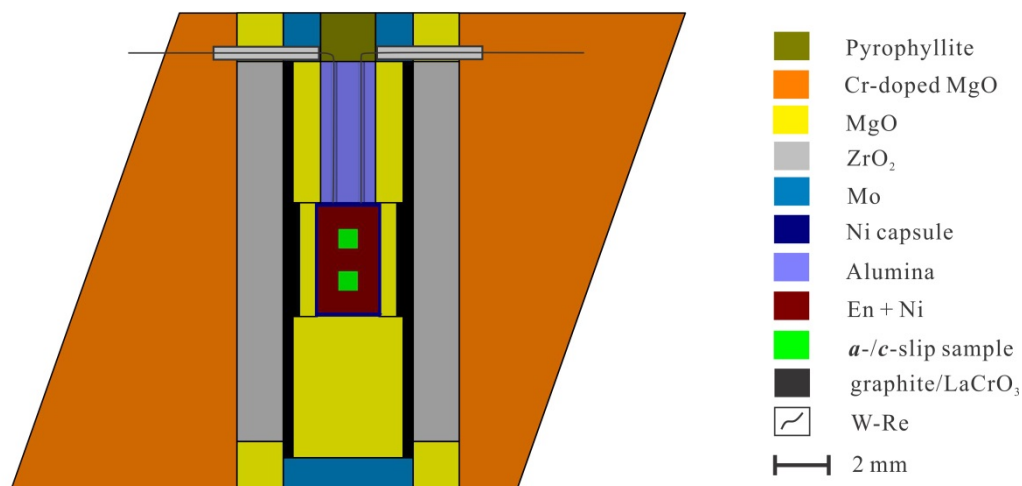


Figure 1. The sample assembly used in the multi-anvil high-pressure annealing experiments.

4.4 Results

Table 1 shows experimental results together with the annealing conditions. The dislocation density of the undeformed olivine cold compressed to 12 GPa is $0.03 \mu\text{m}^{-2}$, which is much smaller than the dislocation density of *a*- and *c*-sample after annealing. Therefore, the effect of cold compression is negligible. Figure 2 shows backscattered electron images (BEI) of the oxidation-decorated dislocations before and after annealing. We measured water contents of three samples before and after annealing at 2 and 12 GPa, which are 13 ± 6 wt. ppm. Because of small difference in water contents between low- and high-pressure annealed samples, the effects of water on dislocation annihilation are ignored in this study.

Table 1. Summary of experimental conditions and results.

[100](010) edge dislocation						
Sample	P (GPa)	Annealing time (h)	area	ρ_i^* (μm^{-2})	ρ_f^{**} (μm^{-2})	$\log(k, \text{m}^2\text{s}^{-1})^\#$
H3998-1	12	23.7	1	0.85 ± 0.25	0.48 ± 0.10	-17.2 ± 0.4
			2	2.47 ± 0.41	0.85 ± 0.19	-17.0 ± 0.2
H3998-2	7	10.7	1	1.22 ± 0.29	0.60 ± 0.14	-16.7 ± 0.2
			2	0.86 ± 0.30	0.54 ± 0.14	-16.8 ± 0.4
H3998-3	2	5.1	1	0.55 ± 0.10	0.33 ± 0.10	-16.2 ± 0.3
Z1253-1	2	6.0	1	2.28 ± 0.05	0.66 ± 0.15	-16.3 ± 0.1
[001](010) screw dislocation						
Sample	P (GPa)	Annealing time (h)	area	ρ_i (μm^{-2})	ρ_f (μm^{-2})	$\log(k, \text{m}^2\text{s}^{-1})$
Z1160-1	12	23.7	1	0.52 ± 0.17	0.24 ± 0.09	-16.6 ± 0.3
			2	2.01 ± 0.19	0.67 ± 0.14	-16.9 ± 0.1
Z1160-2	7	10.7	1	0.66 ± 0.07	0.47 ± 0.09	-16.8 ± 0.3
			2	0.79 ± 0.11	0.40 ± 0.10	-16.5 ± 0.2
Z1160-3	2	5.1	1	0.70 ± 0.17	0.46 ± 0.10	-16.4 ± 0.3
Z1247-1	2	6	1	0.16 ± 0.03	0.09 ± 0.04	-15.6 ± 0.5
Z1247-2	2	6	1	0.13 ± 0.01	0.10 ± 0.01	-16.0 ± 0.3

* Dislocation density before annealing

** Dislocation density after annealing

$$\# k = \frac{1}{\rho_f} - \frac{1}{\rho_i}$$

Figure 3 plots the logarithm of the annihilation rate constants against pressure. The results from previous studies about dislocation recovery on olivine single crystals [Kohlstedt *et al.*, 1980; Karato and Ogawa, 1982; Karato *et al.*, 1993] are also plotted after temperature

correction to 1650 K with an activation energy of 400 kJ/mol and activation volume of 2.7 cm³/mol. The annihilation rate constants of *a*- and *c*-dislocations are comparable, but those for the *c*-dislocations are by 0.3 orders of magnitude higher than those for the *a*-dislocations. The activation volumes of dislocation annihilation rate constants in these two slip systems are both small and identical within the error: $V_a = 2.7 \pm 0.2$ and $V_c = 2.5 \pm 0.9$ cm³/mol for *a*- and *c*-dislocations, respectively.

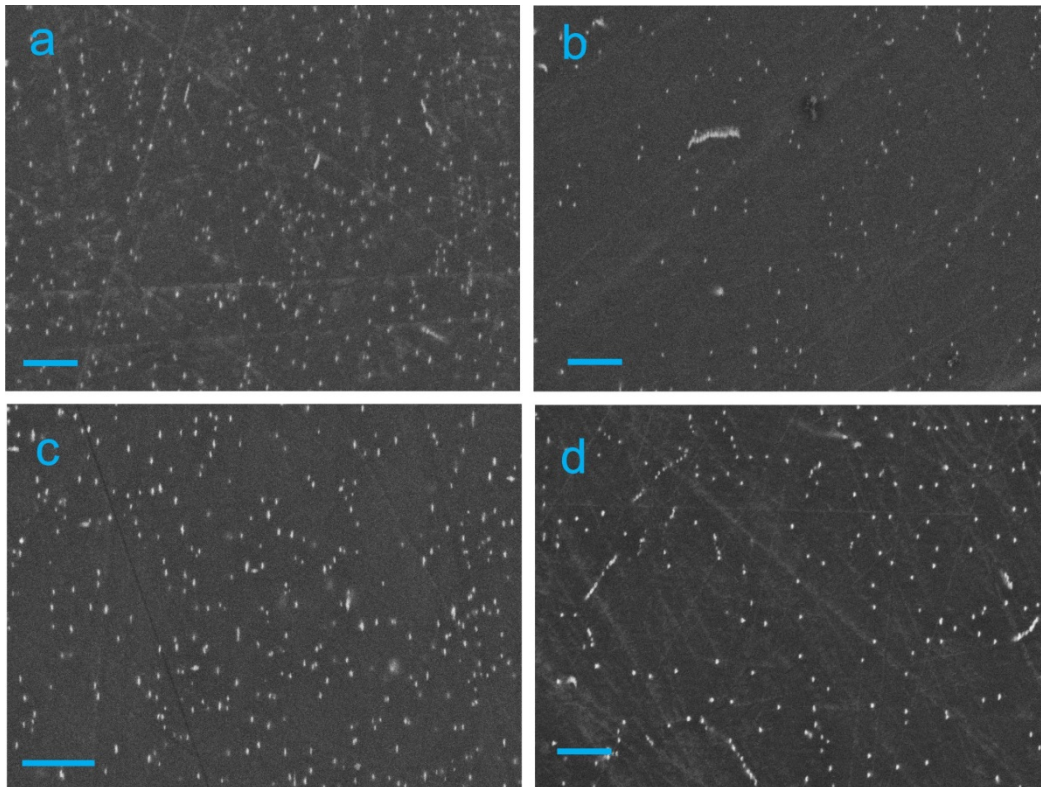


Figure 2. BEIs showing the dislocation density before and after annealing at 12 GPa for 24 h. The images were taken on the (001) plane. a) *a*-slip sample before annealing. b) *a*-slip sample after annealing. c) *c*-slip sample before annealing. d) *c*-slip sample after annealing. The scale bar shown represents 2 μm

dislocation annihilation rate constants of olivine. Furthermore, Jaoul et al. [1981] demonstrated that the Si lattice diffusion is isotropic in forsterite. These facts reinforce that the rate-limiting process of dislocation recovery process is Si diffusion, as already discussed by Wang *et al.* [2016].

Comparison with previous studies

The activation volumes obtained in this study are considerably smaller than those by previous studies, namely $11 \pm 1 \text{ cm}^3/\text{mol}$ by Kohlstedt *et al.* [1980], $14 \pm 2 \text{ cm}^3/\text{mol}$ by Karato and Ogawa [1982], and $6 \pm 1 \text{ cm}^3/\text{mol}$ by Karato *et al.* [1993]. In Kohlstedt *et al.*, [1980] and Karato and Ogawa [1982], the pressure range is only 0.5 and 2 GPa respectively, which is too narrow to give accurate activation volume. In Karato *et al.*, [1993], their activation volumes were obtained by comparing high-pressure data with ambient-pressure ones. The differences in their experimental setups between high-pressure and ambient-pressure experiments could cause some discrepancy in obtained values, which might have biased the pressure dependence in these studies. On the other hand, the annihilation rate constants were obtained in the same experimental setup over the wide pressure interval of 10 GPa in this study, which allows robust estimation of the activation volumes. The rate constants of *a*-dislocation from this study are slightly higher than the high-pressure data of Karato *et al.* [1993], which used the same technique as the present study to investigate the annihilation of *a*-dislocation. The rate constants from Kohlstedt *et al.* [1980] and Karato and Ogawa [1982] are higher than those of *c*-dislocation in this study. This may be due to different technique in counting dislocations. Kohlstedt *et al.* [1980] conducted TEM observation in restricted sample areas, which made it difficult to obtain statistical averages when calculating dislocation annihilation rate constant. Optical microscopy [Karato and Ogawa, 1982] may underestimate dislocation density when it is high, and was applied equally to obtain both initial and annealed dislocation density, which could have given higher annihilation rate constants.

Comparison with other techniques

Although we argued that the activation volumes of the dislocation annihilation rate constants in this study are comparable with that of Si self-diffusion given by *Fei et al.* [2012] ($1.7 \pm 0.4 \text{ cm}^3/\text{mol}$) in forsterite, they are slightly higher. On the other hand, the activation volume of the Si grain-boundary diffusion in forsterite is $4.0 \pm 0.4 \text{ cm}^3/\text{mol}$ [*Fei et al.*, 2016], which is higher than those of the dislocation annihilation and Si lattice diffusion. The lattice diffusion, dislocation climb and grain-boundary diffusion are interactions between atoms and vacancy, dislocation and grain-boundary, respectively. Accordingly, it seems that the activation volume increases with increasing defect dimension. The higher-dimensional defect should have more loose structure, which may cause the larger activation volumes.

Deformation experiments on olivine single crystal by Raterron et al. [2009] yielded different activation volumes for *a*- and *c*-slip samples (12 ± 4 and $3 \pm 4 \text{ cm}^3/\text{mol}$, respectively). This may be due to the large uncertainty of stress conditions in their experiments and fitting the results from their own high-pressure data and *Bai et al.*'s [1991] room-pressure data. Although both studies deformed olivine single crystals in the same orientations, their different experimental setups may have biased the result. Moreover, since both *a*- and *c*-dislocations elongate in the [001] direction and move in the same directions during glide and climb/cross-slip, the activation volumes should be identical, as is shown by this study. Deformation experiments on olivine aggregate [*Karato and Rubie*, 1997; *Karato and Jung*, 2003; *Kawazoe et al.*, 2009] showed that the activation volume for olivine creep is larger than $10 \text{ cm}^3/\text{mol}$. However, the stress conditions in these experiments are about 1 GPa, which is much higher than those in asthenospheric mantle. Therefore, the mechanism of olivine creep in such experiments may not be applicable to low-stress conditions [*Wang et al.*, 2016]. *Couvy et al.* [2004] suggested that C- or B-type olivine fabric should be dominant at a pressure of 11 GPa and a temperature of 1400 °C. However, we note that their olivine fabrics at high temperature were developed during stress relaxation from cold compression which produced dislocations only with the [001] Burgers vector at stresses about 1.5 GPa. Such experiments do

not allow to prove dominance of the dislocations with the [001] Burgers vector at 1400 °C and 11 GPa in the low-stress mantle conditions.

Geophysical application

The identical activation volumes of the *a*- and *c*-dislocations motion lead to the same pressure dependence of olivine creep caused by *a*- and *c*-dislocations. Therefore, our results suggest that the pressure-induced LPO transition by these two types of dislocations is unlikely in asthenospheric mantle, on the assumption that dislocation creep and dislocation recovery are rate limited by the same physical mechanisms in the low-stress mantle conditions. Moreover, the small activation volumes suggest that the pressure effects on creep are small. For example, 10 GPa increase of pressure only causes decrease of creep rate by a factor of 5 at 1650 K by using activation energy of 400 kJ/mol [Wang *et al.*, 2016].

The comparable rate constants, the identical activation energy and volumes [this study and Wang *et al.*, 2016] of *a*- and *c*-dislocation recovery indicate that the rate-limiting process of these two dislocations have similar mobilities under low-stress conditions. Under such conditions, the free dislocation velocity should be equal to the velocity of dislocation motion in the rate-limiting process [Boioli *et al.*, 2015; Wang *et al.*, 2016] and AG-type fabric should be dominant [Wang *et al.*, 2016]. Therefore, the decrease in seismic anisotropy with depth may be explained by the olivine LPO transition from A- or B-type to AG-type by decrease in stress with depth [Wang *et al.*, 2016].

Finally, we note that the effects of water and grain/phase boundary on dislocation mobility are necessary to be investigated in order to provide a better explanation for the LPO development in the Earth's mantle.

4.6 Acknowledgements

The data used are listed in the table 1 and references. We acknowledge F. Heidelbach and

P. O'Brien for providing the olivine single crystals and T. Boffa Ballaran for instructing the single crystal X-ray diffractometry. We thank technical assistance in BGI for the sample and assembly preparation. This research was supported by DFG grants to TK (KA3434/3-1, KA3434/7-1, KA3434/8-1 and KA3434/9-1) and by the annual budget of BGI.

4.7 References

- Boioli, F., P. Carrez, P. Cordier, B. Devincere, and M. Marquille (2015), Modeling the creep properties of olivine by 2.5-dimensional dislocation dynamics simulations, *Physical Review B*, 92(1).
- Couvy, H., D. J. Frost, F. Heidelbach, K. Nyilas, T. Ungar, S. Mackwell, and P. Cordier (2004), Shear deformation experiments of forsterite at 11 GPa-1400 C in the multianvil apparatus, *European Journal of Mineralogy*, 16(6), 877-889.
- Dziewonski, A. M., and D. L. Anderson (1981), Preliminary reference Earth model, *Physics of the Earth and Planetary Interiors*, 25(4), 297-356.
- Ohuchi, T., T. Kawazoe, Y. Nishihara, N. Nishiyama, and T. Irifune (2011), High pressure and temperature fabric transitions in olivine and variations in upper mantle seismic anisotropy, *Earth and Planetary Science Letters*, 304(1-2), 55-63.
- Otsuka, K., and S. I. Karato (2011), Control of the water fugacity at high pressures and temperatures: Applications to the incorporation mechanisms of water in olivine, *Physics of the Earth and Planetary Interiors*, 189(1-2), 27-33.
- Fei, H., C. Hegoda, D. Yamazaki, M. Wiedenbeck, H. Yurimoto, S. Shcheka, and T. Katsura (2012), High silicon self-diffusion coefficient in dry forsterite, *Earth and Planetary Science Letters*, 345-348(0), 95-103.
- Fei, H., S. Koizumi, N. Sakamoto, M. Hashiguchi, H. Yurimoto, K. Marquardt, N. Miyajima, D. Yamazaki, and T. Katsura (2016), New constraints on upper mantle creep mechanism inferred from silicon grain-boundary diffusion rates, *Earth and Planetary Science Letters*, 433, 350-359.
- Gung, Y., M. Panning, and B. Romanowicz (2003), Global anisotropy and the thickness of

- continents, *Nature*, 422(6933), 707-711.
- Hirth, G., and D. Kohlstedt (2003), Rheology of the Upper Mantle and the Mantle Wedge: A View from the Experimentalists, in *Inside the Subduction Factory*, edited, pp. 83-105, American Geophysical Union.
- Jaoul, O., M. Poumellec, C. Froidevaux, and A. Havette (1981), Silicon diffusion in forsterite: a new constraint for understanding mantle deformation, *Anelasticity in the Earth*, 95-100.
- Jung, H., W. Mo, and H. W. Green (2009), Upper mantle seismic anisotropy resulting from pressure-induced slip transition in olivine, *Nature Geosci*, 2(1), 73-77.
- Karato, S. i. (1992), On the Lehmann discontinuity, *Geophysical Research Letters*, 19(22), 2255-2258.
- Karato, S.-i. (2012), *Deformation of earth materials: an introduction to the rheology of solid earth*, Cambridge University Press.
- Karato, S.-I., D. C. Rubie, and H. Yan (1993), Dislocation recovery in olivine under deep upper mantle conditions: Implications for creep and diffusion, *Journal of Geophysical Research: Solid Earth*, 98(B6), 9761-9768.
- Karato, S.-i., and D. C. Rubie (1997), Toward an experimental study of deep mantle rheology: A new multianvil sample assembly for deformation studies under high pressures and temperatures, *Journal of Geophysical Research: Solid Earth*, 102(B9), 20111-20122.
- Karato, S.-I., and H. Jung (2003), Effects of pressure on high-temperature dislocation creep in olivine, *Philosophical Magazine*, 83(3), 401-414.
- Karato, S., and M. Ogawa (1982), High-pressure recovery of olivine: implications for creep mechanisms and creep activation volume, *Physics of the Earth and Planetary Interiors*, 28(2), 102-117.
- Kawazoe, T., S.-i. Karato, K. Otsuka, Z. Jing, M. Mookherjee (2009), Shear deformation of dry polycrystalline olivine under deep upper mantle conditions using a rotational Drickamer apparatus (RDA), *Phys. Earth Planet. Inter.*, 174, 128
- Kohlstedt, D., H. Nichols, and P. Hornack (1980), The effect of pressure on the rate of dislocation recovery in olivine, *Journal of Geophysical Research: Solid Earth*, 85(B6),

3122-3130.

- Kumazawa, M., and O. L. Anderson (1969), Elastic moduli, pressure derivatives, and temperature derivatives of single-crystal olivine and single-crystal forsterite, *Journal of Geophysical Research*, 74(25), 5961-5972.
- Mainprice, D., A. Tommasi, H. Couvy, P. Cordier, and D. J. Frost (2005), Pressure sensitivity of olivine slip systems and seismic anisotropy of Earth's upper mantle, *Nature*, 433(7027), 731-733.
- Montagner, J. P., and B. L. N. Kennett (1996), How to reconcile body-wave and normal-mode reference earth models, *Geophysical Journal International*, 125(1), 229-248.
- Nettles, M., and A. M. Dziewonski (2008), Radially anisotropic shear velocity structure of the upper mantle globally and beneath North America, *Journal of Geophysical Research-Solid Earth*, 113(B2), 27.
- Ohuchi, T., T. Kawazoe, Y. Nishihara, N. Nishiyama, T. Irifune (2001), High pressure and temperature fabric transitions in olivine and variations in upper mantle seismic anisotropy, *Earth Planet. Sci. Lett.*, 304, 55
- Paterson, M. (1982), The determination of hydroxyl by infrared absorption in quartz, silicate glasses, and similar materials, *Bulletin de la Societe Francaise de Mineralogie*, 105, 20-29.
- Raterron, P., J. Chen, T. Geenen, and J. Girard (2011), Pressure effect on forsterite dislocation slip systems: Implications for upper-mantle LPO and low viscosity zone, *Physics of the Earth and Planetary Interiors*, 188(1-2), 26-36.
- Raterron, P., E. Amiguet, J. Chen, L. Li, and P. Cordier (2009), Experimental deformation of olivine single crystals at mantle pressures and temperatures, *Physics of the Earth and Planetary Interiors*, 172(1-2), 74-83.
- Ringwood, A. E. (1991), Phase transformations and their bearing on the constitution and dynamics of the mantle, *Geochimica et Cosmochimica Acta*, 55(8), 2083-2110.
- Visser, K., J. Trampert, S. Lebedev, and B. L. N. Kennett (2008), Probability of radial anisotropy in the deep mantle, *Earth and Planetary Science Letters*, 270(3-4), 241-250.

Wang, L., S. Blaha, Z. Pintér, R. Farla, T. Kawazoe, N. Miyajima, K. Michibayashi, and T. Katsura (2016), Temperature dependence of [100](010) and [001](010) dislocation mobility in natural olivine, *Earth and Planetary Science Letters*, 441, 81-90.

5. Identical mechanism for the motion of screw and edge dislocations in natural olivine

Lin Wang^{a,*} and Tomoo Katsura^a

^a Bayerisches Geoinstitut, University of Bayreuth, 95440 Bayreuth, Germany.

5.1 Abstract

Dislocation recovery experiments were conducted on pre-deformed olivine single crystals at temperatures of 1,450 to 1,760 K, room pressure, and oxygen partial pressures near the Ni-NiO buffer to determine the annihilation rates constants for [001] (010) edge dislocations. The obtained annihilation rate constants were comparable with those for previously determined [001] screw dislocations. The activation energies for the motion of both dislocations are identical, i.e., ~400 kJ/mol. These suggest that the motion of screw dislocations in olivine is not controlled by cross-slip but by the same rate-limiting process of the motion of edge dislocations, i.e. climb, under low-stress and high-temperature conditions. Therefore, the conventional climb-controlled model for olivine should be applicable to the motions of not only edge but also screw dislocations. The softening of the asthenosphere cannot be explained by cross-slip as the rate-limiting process of dislocation creep.

5.2 Introduction

Geophysical observations suggested that a soft asthenosphere underlies a rigid lithosphere based on analysis of the geoid (e.g. Hager, 1991) and post-glacial rebound (e.g. Peltier, 1998). The geodynamic modellings (e.g. Becker, 2017; Craig and McKenzie, 1986) also suggested the same result. The reason for the softening of the asthenosphere is under debate. The simplest explanation is softening of materials due to temperature increase from

the lithosphere to the asthenosphere, but results of deformation experiments on dry peridotite implied that high temperature is insufficient to explain softness of the asthenosphere (Hirth and Kohlstedt, 2003). A popular explanation is hydrous weakening of olivine, but is doubted by recent Si self-diffusion experiments (Fei et al., 2016; Fei et al., 2013) based on the assumption that dislocation creep is controlled by climb of edge dislocations. However, motion of screw dislocations is not considered to involve climb. Therefore, the results of diffusion experiments cannot be applied to dislocation creep if it is controlled by motion of screw dislocations. Moreover, Poirier and Vergobbi (1978) suggested that, if cross-slip of dissociated screw dislocations controls olivine dislocation creep, the estimated upper mantle viscosity would be one order of magnitude lower than that predicted by the climb-controlled model in the stress range from 10 to 100 MPa. This potentially explains the softening of the asthenosphere. Therefore, it is essential to know the rate-limiting process for screw dislocations.

However, both diffusion and deformation experiments cannot solve this problem. Diffusion does not involve motion of dislocations. The stress ranges in deformation experiments are too narrow to constrain the rate-limiting process of dislocation motions, although in theory it could be determined by checking the stress dependence of creep rates (e.g. Karato, 2012; Poirier, 1985). Hirth and Kohlstedt (2003) compiled deformation data from their previous studies, and concluded that the stress dependence of creep rates has an exponent of 3.5, suggesting a climb-controlled model. However, the stress range of their dislocation creep tests is 100 to 224 MPa, which is too narrow to determine the change in the stress exponent with stress. Actually, Kohlstedt and Goetze (1974) conducted deformation experiments on olivine single crystals at stresses from 5 to 150 MPa, and found that $d \log \dot{\epsilon} / d \log \sigma$, where $\dot{\epsilon}$ is the strain rate and σ is the stress, gradually decreases with decreasing stress. Poirier (1985) found that different deformation experiments on olivine single crystals under different stress conditions give different stress exponents.

In this study, we conducted dislocation recovery experiments for edge dislocations in the [001](010) slip system (hereafter called *c*-edge dislocation) at various temperatures and room

pressure by the same method as that of Wang et al. (2016). We have compared the rate constants and activation energy with those from Wang et al. (2016) for screw dislocations in the same slip system (hereafter called c -screw dislocation). It is important to compare mobility of edge and screw dislocations in the same system, because the activation energy may be different among different slip systems (Bai et al., 1991). The similar densities for edge and screw dislocations in this slip system (Bai and Kohlstedt, 1992; Wang et al., 2016) make it ideal to examine the rate-limiting processes for both kinds of dislocations. During dislocation recovery, dislocations move under the influence of internal stress, which is a function of dislocation density. Since dislocation motions on the slip plane (glide) and out of the slip plane (climb, cross-slip) occur successively during recovery, the activation energy determined by this method represents that of the rate-limiting process of dislocation motions. Our results show the identical activation energy of c -edge and c -screw dislocations, i.e. 400 kJ/mol. Therefore, the motion of screw dislocations has the same rate-limiting process as that of edge dislocations, and therefore softening of the asthenosphere cannot be explained by cross-slip as the rate-limiting process of dislocation motions.

5.3 Experimental Procedures

The same Pakistan olivine and sample preparation procedure as those of Wang et al. (2016) were employed in this study. The composition of olivine was reported by Gose et al. (2010). The olivine single crystal was orientated by X-ray diffraction and electron backscattered diffraction (EBSD), and then placed in the cell assembly such that the [001] direction is parallel to the shear direction and the (010) plane is parallel to the shear plane (Fig. 1).

High-density dislocations with the [001] Burgers vector on the (010) plane were produced by experimental deformation using a Kawai-type multi-anvil apparatus at University of Bayreuth. The sample assembly was first pressurized to 3 GPa using a press load of 3.7 MN, and then heated to a temperature of 1,600 K and held for 15 min to sinter crushable alumina. After that, the assembly was further compressed to a press load of 3.9 MN

for 15 min to deform the sample. After the deformation, the sample was quenched by switching off the heating power, and then decompressed to room pressure for more than 16 hours. Transmission electronic microscopy (TEM) by Wang et al. (2016) found $[001](010)$ slip system was successfully activated and dominant by this procedure. The ratio of screw to edge dislocations was 3:2, as reported by Wang et al. (2016).

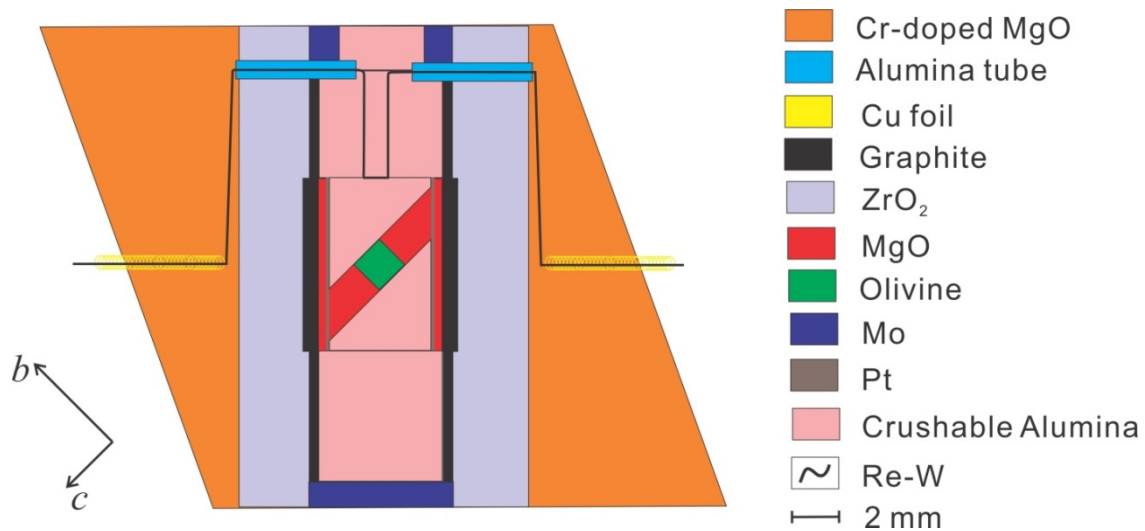


Figure 1. Deformation setup used to generate c -dislocations. The crystallographic axes of olivine are shown in the left bottom.

The deformed olivine crystals were cut into eight cubic pieces, and paired into four groups, in which the two pieces in each group shared a common (100) plane. One piece from each pair was used to determine the initial dislocation density, while the other was used to determine dislocation density after the annealing. The annealing experiments were conducted at ambient pressure and temperatures of 1,460 to 1,760 K for 35 min to 24 hours using a gas mixing furnace. The oxygen partial pressure was controlled at 10^{-6} - 10^{-8} MPa, which is near the Ni-NiO buffer, using a CO-CO₂ gas mixture. Table 1 summarizes conditions of the annealing experiments.

Dislocations were observed using the same oxidation decoration technique as Wang et al. (2016). The corresponding areas away from subgrain boundaries on the common (100) plane in the initial and annealed pieces from the same group were observed to determine the change

in dislocation densities before and after annealing.

The annihilation rate constants were calculated using the second-order dislocation recovery kinetics (Karato and Ogawa, 1982; Kohlstedt et al., 1980; Wang et al., 2016)

$$k = \frac{\frac{1}{\rho_f} - \frac{1}{\rho_i}}{t}, \quad (2)$$

where ρ_f and ρ_i are the dislocation densities after and before annealing, respectively, and t is the annealing time. Because of the thermally activated process, the dislocation annihilation rate constant is assumed to follow the Arrhenius relationship:

$$k = k_0 \exp\left(-\frac{E}{RT}\right) \quad (3)$$

where k_0 is a constant, E is the activation energy of dislocation annihilation, T is the temperature, and R is the gas constant. As discussed above, this activation energy should represent that of the rate-limiting process of dislocation motions.

5.4 Results

Table 1 shows experimental results together with the annealing conditions. Dislocation density in the samples before deformation is less than $0.0004 \mu\text{m}^{-2}$, which is negligible in comparison with dislocation density after deformation (Table 1). Figure 2 shows back-scattered electron images of decorated dislocations in the corresponding areas in the samples from the same pair before and after annealing. The c -screw dislocations appear as lines and the c -edge dislocations as dots on the (100) plane due to their geometries. A jog on screw dislocations is indicated by the red arrow in Figure 2. Decrease in dislocation density was observed by comparing the images before and after annealing. The water contents in the samples before and after annealing were below the detection limit of infrared spectroscopy. The transmission electron microscope images of the dislocation structures after deformation

were given in Fig. 4 in Wang et al. (2016).

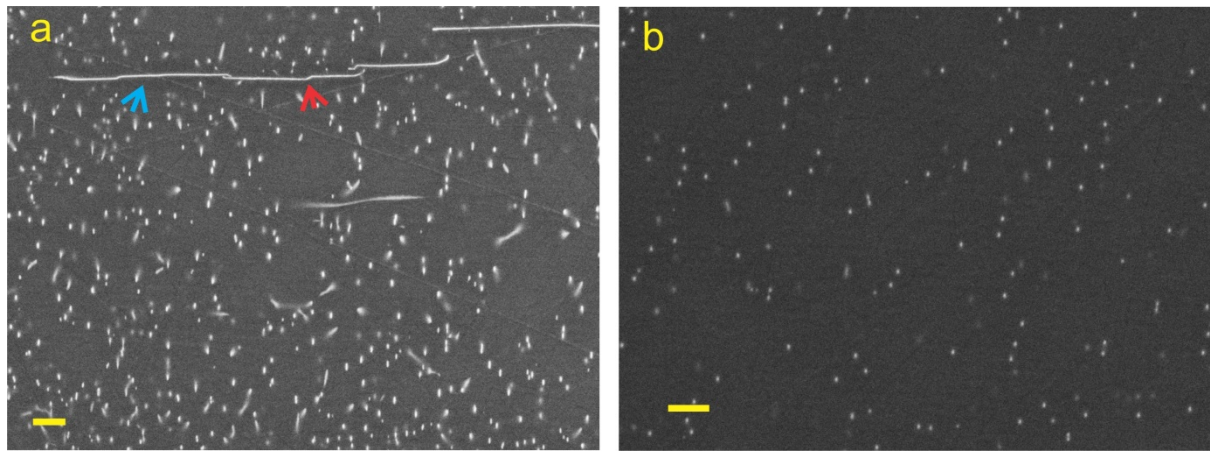


Figure 2. BEIs showing the dislocation density (a) before and (b) after annealing at 1760 K for 35 minutes. The images were taken on the (100) plane. Screw and edge dislocations are lines and dots, respectively, due to the geometries of their dislocation lines. The blue arrow indicates a part of a screw dislocation without jogs and the red arrow indicates a jog on screw dislocation. The yellow scale bar represents 2 μm .

Table 1. Summary of experimental conditions and results*.

[001](010) edge dislocation						
Sample	T (K)	Annealing time (h)	$\log(f_{O_2}, 10^5 \text{ Pa})$	$\rho_i (\mu\text{m}^{-2})$	$\rho_f (\mu\text{m}^{-2})$	$\log(k, \text{m}^2\text{s}^{-1})$
Z1643-1	1763	0.58	-4.9	1.60 ± 0.13	0.29 ± 0.01	-14.87 ± 0.03
				0.97 ± 0.13	0.22 ± 0.01	-14.77 ± 0.03
Z1643-2	1673	2.5	-5.7	1.49 ± 0.04	0.36 ± 0.06	-15.63 ± 0.09
				1.13 ± 0.12	0.31 ± 0.03	-15.58 ± 0.05
Z1643-3	1473	24	-7.7	1.33 ± 0.15	0.73 ± 0.05	-17.14 ± 0.09
				0.35 ± 0.03	0.29 ± 0.01	-17.22 ± 0.27

* different ρ_i and ρ_f in each sample correspond to different areas

Figure 3 plots the logarithmic rate constants of c -edge dislocations annihilation against

the reciprocal temperature. The results from the previous dislocation recovery experiments on c -screw dislocations (Wang et al., 2016) are also plotted in this figure. The dislocation annihilation rate constants of c -edge and c -screw dislocations are comparable, but those of the c -screw are about half an order of magnitude higher than those of the c -edge. The temperature dependences for these two dislocations are identical. Their activation energies are found $E_{c\text{-edge}} = 400 \pm 20$ kJ/mol and $E_{c\text{-screw}} = 400 \pm 30$ kJ/mol for the c -edge and c -screw, respectively.

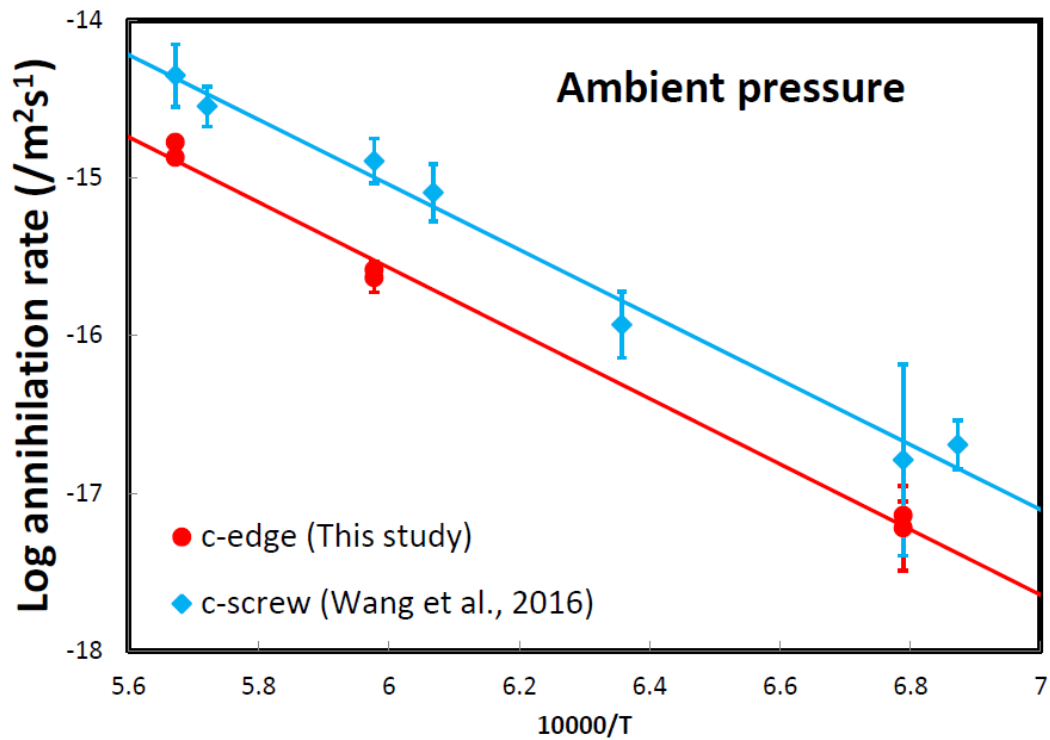


Figure 3. Logarithmic dislocation annihilation rate constants of c -edge dislocations versus reciprocal temperature. Together plotted are the annihilation rate constants of c -screw dislocations from previous study. The activation energies for both dislocations are identical, i.e. 400 kJ/mol.

5.5 Discussion

The annihilation rate constants of the c -edge and c -screw are comparable and their

activation energies are identical with each other, indicating that the motions of edge and screw dislocations are both controlled by the same mechanism. The motion of edge dislocations is controlled by climb at high temperatures and low stresses (e.g. Hull and Bacon, 2001; Kohlstedt, 2006), in which diffusion is involved. Point defects need to be absorbed to or emitted from dislocations, rendering dislocations to move out of the slip planes. However, motion of a pure screw dislocation does not involve climb because screw segments have no specific slip plane (Hull and Bacon, 2001). Therefore, the motion of pure screw segments cannot be rate-limited by climb. In order to explain the same mechanism for the motions of both edge and screw dislocations, a climb-controlled model for the motion of screw dislocations is proposed below (Fig. 4).

A screw dislocation forms a jog by cross-slips (Fig. 2 and 4) to overcome obstacles that it meets during glide from A to B in Figure 4. The jogs have the same Burgers vector (\mathbf{b}) as their parental dislocations (the x direction in Fig. 4), but the dislocation line of the jog (\mathbf{J}) (red segments in Fig. 4, parallel to z direction) is normal to the direction of the Burgers vector \mathbf{b} . This is different from its parental screw dislocation, whose line direction (\mathbf{L}) is parallel to the direction of \mathbf{b} . Therefore, the jog on the screw dislocation has an edge character. The slip plane of the jog is defined by its dislocation line (\mathbf{J}) and the Burgers vector (\mathbf{b}), indicated by the yellow plane in Fig. 4. The screw dislocation glides in the y direction in Fig. 4 and therefore, the jog in the screw dislocation needs climb motion also in the y direction to move along with their parental dislocation so that the screw dislocation can go through the obstacle. This climb of the jog should serve as the rate-limiting process of the screw dislocation motions.

The activation energy of motion of screw dislocations might be attributed to that of the cross-slip due to recombination of partial dislocations and the agreement of the activation energies of motions between c -edge and c -screw dislocations could be accidental. However, this possibility is unlikely because of the following reasoning. If cross-slip served as a rate-limiting process, the activation energy of dislocation motion should be a function of stress (Poirier, 1976). The rate constants of c -screw dislocations are obtained at different ρ_i ,

i.e. different internal stresses in our studies. The internal stresses drive dislocations to move during annealing. If the activation energy of dislocation motion is stress-dependent, the rate constant must have a correlation with the dislocation density ρ_i at a given temperature. However, we did not find such a correlation by judging from table 1 from Wang et al., (2016). Therefore, the activation energy of screw dislocation motions is not that of cross-slip.

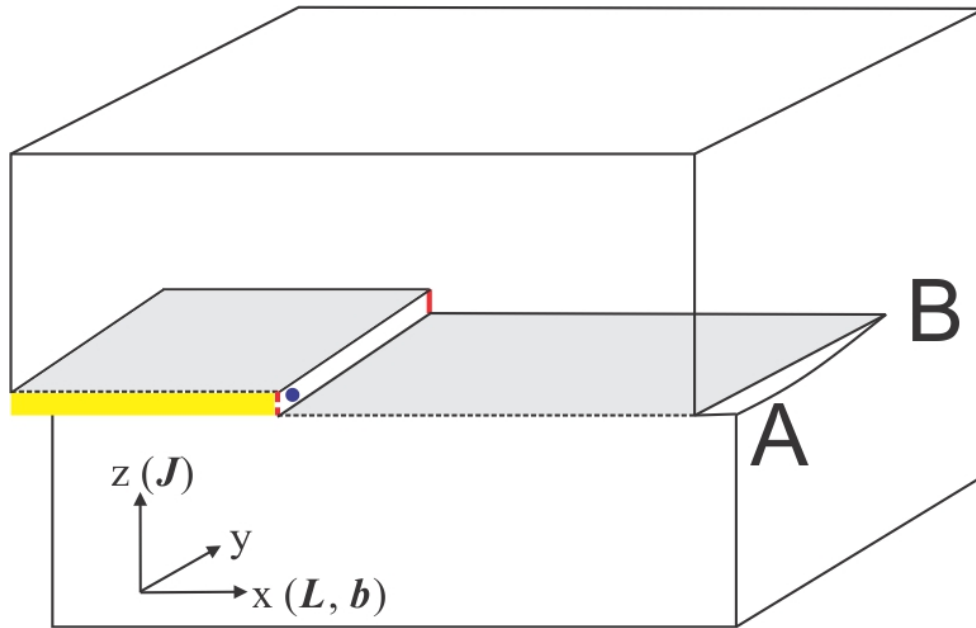


Figure 4. A schematic diagram showing the jog-climb controlled motion of a screw dislocation. The screw dislocation is elongated in the x direction, which is parallel to its Burgers vector \mathbf{b} , and glides in the y direction from A to B. The blue dot represents the obstacle that the screw dislocation meets during glide. A jog (red segment) elongated in the z direction is produced on the screw dislocation in order to overcome the obstacle. This jog has an edge nature with the same Burgers vector \mathbf{b} as the parental screw dislocation. The yellow area indicates the glide plane of the jog, which is normal to the y direction. The jog has to climb out of its glide plane in order to move along with its parental screw dislocation.

5.6 Implications

The present study improves the applicability of the climb-controlled model for olivine dislocation creep. The climb-controlled model assumes that climb of edge dislocations is a

rate-limiting process of dislocation motions (Weertman, 1955), which implies the edge dislocations move much slower than screw dislocations. However, studies on dislocation structures (Bai and Kohlstedt, 1992; Wang et al., 2016) suggested that edge and screw dislocations have similar velocity at least for [001](010) slip system. Therefore, the role of screw dislocations in dislocation creep must be taken into account. The present study demonstrates that motion of screw dislocations is also controlled by climb. This indicates that the climb-controlled model can be used in olivine dislocation creep regardless of dislocation characters. Moreover, because climb is controlled by diffusion, diffusion results are applicable to dislocation creep as long as a diffusion coefficient of an appropriate species is chosen.

The softening of asthenosphere cannot be explained by the model in which dislocation creep is controlled by cross-slip of screw dislocations. Poirier and Vergobbi (1978) proposed the cross-slip controlled model for olivine creep and suggested that viscosity of the Earth's upper mantle is about one order of magnitude lower than that predicted by the climb-controlled model in the stress range from 10 to 100 MPa. In this model, cross-slip is assumed to be controlled by recombination of partial screw dislocations. The dissociation of screw dislocations were confirmed by transmission electron microscopy in olivine (Fujino et al., 1993; Vander Sande and Kohlstedt, 1976). Therefore, this model potentially explains the softening of the asthenosphere. However, the rate-limiting process for motion of screw dislocations is never tested before. The present study suggests that both edge and screw dislocations have the same rate-limiting mechanism of motions, i.e. climb, demonstrating that the cross-slip model cannot be applied to the olivine dislocation creep.

The softening of asthenosphere may be explained by existence of melt in the asthenosphere to some extent (e.g. Hirth and Kohlstedt 2003). We also emphasize that water could be still a reason, at least partly, for softening of the asthenosphere although diffusion studies disprove this hypothesis (Fei et al., 2016; Fei et al., 2013). This study proves that climb is the rate-limiting process of dislocation motions, but the diffusion process which controls climb is still under debate. Hirth and Kohlstedt (2015) suggested that climb in

olivine may be controlled by pipe diffusion rather than lattice diffusion. Further studies on relations between dislocation climb and diffusion are needed to solve this problem.

5.7 Acknowledgements

We thank H. Fischer, R. Njul in BGI for the sample and assembly preparation. This research was supported by DFG grants to TK (KA3434-3/1, KA3434-7/1 and KA3434-8/1) and by the annual budget of BGI.

5.8 References

- Bai, Q., and Kohlstedt, D. L., 1992, High-temperature creep of olivine single crystals, 2. dislocation structures: *Tectonophysics*, v. 206, no. 1–2, p. 1-29.
- Bai, Q., Mackwell, S. J., and Kohlstedt, D. L., 1991, High-temperature creep of olivine single crystals 1. Mechanical results for buffered samples: *Journal of Geophysical Research: Solid Earth*, v. 96, no. B2, p. 2441-2463.
- Becker, T. W., 2017, Superweak asthenosphere in light of upper mantle seismic anisotropy: *Geochemistry, Geophysics, Geosystems*.
- Craig, C. H., and McKenzie, D., 1986, The existence of a thin low-viscosity layer beneath the lithosphere: *Earth and Planetary Science Letters*, v. 78, no. 4, p. 420-426.
- Fei, H., Koizumi, S., Sakamoto, N., Hashiguchi, M., Yurimoto, H., Marquardt, K., Miyajima, N., Yamazaki, D., and Katsura, T., 2016, New constraints on upper mantle creep mechanism inferred from silicon grain-boundary diffusion rates: *Earth and Planetary Science Letters*, v. 433, p. 350-359.
- Fei, H., Wiedenbeck, M., Yamazaki, D., and Katsura, T., 2013, Small effect of water on upper-mantle rheology based on silicon self-diffusion coefficients: *Nature*, v. 498, no. 7453, p. 213-+.
- Fujino, K., Nakazaki, H., Momoi, H., Karato, S.-i., and Kohlstedt, D. L., 1993, TEM observation of dissociated dislocations with $b=[010]$ in naturally deformed olivine:

- Physics of the earth and planetary interiors, v. 78, no. 1-2, p. 131-137.
- Gose, J., Schmaedicke, E., Markowitz, M., and Beran, A., 2010, OH point defects in olivine from Pakistan: *Mineralogy and Petrology*, v. 99, no. 1-2, p. 105-111.
- Hager, B. H., 1991, Mantle viscosity: A comparison of models from postglacial rebound and from the geoid, plate driving forces, and advected heat flux, *Glacial isostasy, sea-level and mantle rheology*, Springer, p. 493-513.
- Hirth, G., and Kohlstedt, D., 2003, Rheology of the Upper Mantle and the Mantle Wedge: A View from the Experimentalists, *Inside the Subduction Factory*, American Geophysical Union, p. 83-105.
- Hirth, G., and Kohlstedt, D., 2015, The stress dependence of olivine creep rate: Implications for extrapolation of lab data and interpretation of recrystallized grain size: *Earth and Planetary Science Letters*, v. 418, p. 20-26.
- Hull, D., and Bacon, D. J., 2001, *Introduction to dislocations*, Butterworth-Heinemann. P.257
- Karato, S.-i., 2012, *Deformation of earth materials: an introduction to the rheology of solid earth*, Cambridge University Press. P.463
- Karato, S., and Ogawa, M., 1982, High-pressure recovery of olivine: implications for creep mechanisms and creep activation volume: *Physics of the Earth and Planetary Interiors*, v. 28, no. 2, p. 102-117.
- Kohlstedt, D., Nichols, H., and Hornack, P., 1980, The effect of pressure on the rate of dislocation recovery in olivine: *Journal of Geophysical Research: Solid Earth (1978–2012)*, v. 85, no. B6, p. 3122-3130.
- Kohlstedt, D. L., 2006, The Role of Water in High-Temperature Rock Deformation: *Reviews in Mineralogy and Geochemistry*, v. 62, no. 1, p. 377-396.
- Kohlstedt, D. L., and Goetze, C., 1974, Low-stress high-temperature creep in olivine single crystals: *Journal of Geophysical Research*, v. 79, no. 14, p. 2045-2051.
- Peltier, W., 1998, Postglacial variations in the level of the sea: Implications for climate dynamics and solid - earth geophysics: *Reviews of Geophysics*, v. 36, no. 4, p. 603-689.
- Poirier, J.-P., 1985, *Creep of crystals: high-temperature deformation processes in metals*,

ceramics and minerals, Cambridge University Press.

Poirier, J.-P., and Vergobbi, B., 1978, Splitting of dislocations in olivine, cross-slip-controlled creep and mantle rheology: *Physics of the Earth and Planetary Interiors*, v. 16, no. 4, p. 370-378.

Poirier, J., 1976, On the symmetrical role of cross-slip of screw dislocations and climb of edge dislocations as recovery processes controlling high-temperature creep: *Revue de Physique Appliquée*, v. 11, no. 6, p. 731-738.

Vander Sande, J., and Kohlstedt, D., 1976, Observation of dissociated dislocations in deformed olivine: *Philosophical Magazine*, v. 34, no. 4, p. 653-658.

Wang, L., Blaha, S., Pintér, Z., Farla, R., Kawazoe, T., Miyajima, N., Michibayashi, K., and Katsura, T., 2016, Temperature dependence of [100](010) and [001](010) dislocation mobility in natural olivine: *Earth and Planetary Science Letters*, v. 441, p. 81-90.

Weertman, J., 1955, Theory of Steady - State Creep Based on Dislocation Climb: *Journal of Applied Physics*, v. 26, no. 10, p. 1213-1217.

6. Activation of [100](001) slip system by water incorporation in olivine

Lin Wang^{a,*}, Nobuyoshi Miyajima^a, Takaaki Kawazoe^b, and Tomoo Katsura^a

^a Bayerisches Geoinstitut, University of Bayreuth, 95440 Bayreuth, Germany.

^b Department of Earth and Planetary Systems Science, Hiroshima University, Japan

6.1 Abstract

The origin of E-type fabric of olivine is investigated. A natural olivine was first hydrated at 5 GPa and 1473 K or dehydrated at room pressure at 1473 K at oxygen fugacity near enstatite-magnesite-olivine-graphite (EMOG) buffer conditions. The hydrated/dehydrated olivine was then sheared in the [100] direction on the (001) plane at pressures of 2 to 5 GPa and temperatures of 1473 or 1573 K. The deformed samples contained 4 – 60 wt. ppm water based on Paterson calibration. The deformed samples were observed by transmission electron microscopy (TEM) on the (001) plane to determine whether the [100](001) slip system was activated or not. Only c -elongated [100] dislocations were observed for the anhydrous samples, while [100](001) dislocations dominated in the hydrous samples. The dislocation structure of the [100](001) slip system developed under hydrous and relatively low-temperature conditions is different from that under anhydrous and high-temperature conditions in previous studies. We conclude that the incorporation of water into olivine helps activate the [100](001) slip system by reducing its Peierls stress. This supports the idea that E-type fabric can exist under hydrous conditions.

6.2 Introduction

Lattice preferred orientation (LPO), or fabric, of olivine is essential to interpret the seismic anisotropy in the Earth's upper mantle (Karato et al., 2008), because olivine is the most abundant mineral in the upper mantle (Ringwood, 1991), and is elastically anisotropic (Kumazawa and Anderson, 1969). Olivine fabrics change according to physical and chemical environments, as suggested by observations of natural samples and laboratory deformation experiments. Therefore, knowledge of conditions of fabric formation can be used to understand physical and chemical conditions in the Earth's interior. Moreover, mantle flow geometry can be inferred by combining observations of seismic anisotropy with knowledge of fabric formation of mantle minerals.

A number of seismic studies have shown that seismic anisotropy in the upper mantle becomes weaker with depth. One-dimensional global models, PREM (Dziewonski and Anderson, 1981) and SP6-F (Montagner and Kennett, 1996), suggested that horizontally polarized S-wave velocity (V_{SH}) is faster than vertically polarized S-wave velocity (V_{SV}) in the uppermost mantle, but this difference decreases with depth. The V_{SH}/V_{SV} ratio obtained from shear wave tomography (Gung et al., 2003) and surface wave analyses (Visser et al., 2008) reached identical conclusions. The decrease in seismic anisotropy may reflect a change of olivine LPO due to different thermomechanical conditions.

Conditions of formation of different fabrics in olivine aggregates have been studied by both petrography and experiments. Lineation and foliation of peridotite are believed to represent the shear direction and shear plane of mantle flow, respectively. By this assumption, olivine fabrics can be identified for natural samples. Mainprice (2007) categorized olivine LPO types to six different groups (A, B, C, D, E, AG) using dataset from Ismail and Mainprice (1998) and found that most peridotite samples from ophiolites and the continental lithosphere show A-type olivine fabrics. Tommasi and Vauchez (2015) used enlarged dataset and found that the E-type fabric has been observed only in harzburgite and dunite deformed under hydrous conditions. These investigations suggested that water can cause A- to E-type

fabric transition. This idea is also supported by Michibayashi et al. (2016). They demonstrated that the E-type fabrics were not found in ridge peridotites, by investigating their recently compiled dataset. The V_{SH}/V_{SV} ratios produced by the E-type fabric are smaller than by those formed by the A-type fabric (Karato et al., 2008). Since asthenosphere contains more water than lithosphere (Hirth and Kohlstedt, 1996), the possible water-induced A- to E-type fabric transition can explain why the seismic anisotropy decreases with depth.

Laboratory deformation experiments also suggested water-induced fabric transitions. Jung and Karato (2001) suggested that the olivine fabric changes from A- to C-type with increasing water content. Katayama et al. (2004) suggested that E-type fabric dominates at moderate water content between the A- and C-type fabrics. They reported that the boundaries between A- and E-type fabrics and between E- and C-type fabrics are located at water contents of 200 and of 500 to ~1100 ppm H/Si, respectively. They also suggested that the water content for the E- to C-type transition decreases with increasing stress.

Formation of LPO in mantle minerals is a consequence of the dominant slip systems in dislocation creep. The water-induced fabric transitions of olivine indicate that different slip systems dominate at different water contents. The A-, C-, E-type fabrics are assumed to be caused by the dominant activities of [100](010), [001](100) and [100](001) slip systems, respectively (Mainprice, 2007). Transmission electron microscopy (TEM) studies of natural (Goetze and Kohlstedt, 1973) and laboratory deformed samples (Darot and Gueguen, 1981; Durham and Goetze, 1977; Durham et al., 1977; Kohlstedt and Goetze, 1974; Ohuchi et al., 2015; Phakey et al., 1972) confirmed the existence of [100](010) slip system under anhydrous conditions. The [001](100) slip system has been observed in laboratory deformed samples at high (>1523 K, Durham et al., 1977; Bai and Kohlstedt, 1992) or low temperatures (<1523 K, Gaboriaud et al., 1981; Mussi et al., 2014; Ohuchi et al., 2015; Phakey et al., 1972) under anhydrous conditions and low temperatures under hydrous conditions (Jung et al., 2006) by TEM or oxidation decoration methods. The [100](001) slip system has been observed by TEM (Durham et al., 1977) and oxidation decoration techniques (Bai and Kohlstedt, 1992; Durham et al., 1977) on laboratory deformed samples under

anhydrous conditions. However, there is no TEM study to confirm the activation of [100](001) slip system under hydrous conditions, and the physical mechanisms for the existence of the E-type fabric under hydrous conditions is therefore unknown. In this study, we have therefore conducted TEM observations on hydrous olivine single crystal sheared in the [100] direction on the (001) plane to investigate a reason for the activation of the [100](001) slip system.

6.3 Experimental Procedures

Sample Preparation

The samples used in this study were single crystals of natural olivine from Pakistan. The same olivine has been described by Gose et al. (2010), which reported its major and trace element contents including its water content. The *c*-axis of each crystal was determined using a Huber single-crystal diffractometer operated by SINGLE2014 (Angel and Finger, 2011). The oriented olivine crystals were mounted in epoxy resin with the (001) plane exposed to the surface, and then polished using diamond powder with a grain size of 0.25 μm . The [010] and [100] axes of the crystals were determined by means of electron backscatter diffraction (EBSD). The cube with 1.5 mm edge length was shaped from the oriented crystal along its principal crystallographic planes.

Hydration/dehydration experiments

The olivine cubes were hydrated or dehydrated before deformation. In dehydration, the cubes were put into a Pt basket and annealed at ambient pressure and a temperature of 1473 K for 12 h in a CO-CO₂ gas mixing furnace. The oxygen partial pressure was controlled at 10^{-7.5} MPa, which was near the enstatite-magnesite-olivine-graphite (EMOG) buffer.

Hydration experiments were conducted at a pressure of 5 GPa and a temperature of 1473 K using a Kawai-type multi-anvil apparatus at University of Bayreuth. The cell assembly is shown in Fig. 1. A single-crystal olivine cube was loaded into a gold capsule with outer and

inner diameters of 3.7 and 3.2 mm, respectively, whose one end was sealed. A mixture of talc and brucite powders (weight ratio 4:1) was loaded at the sealed end of the capsule. It was used as a water source and also to control the silica activity of the sample. Graphite powder was used to surround the cube to prevent its mechanical damage during compression and to constrain the oxygen fugacity inside the capsule under the EMOG buffer conditions. Various water contents in the samples were obtained by having different ratios of the water source to graphite. The open end of the capsule was closed and sealed by arc welding after sample loading. The gold capsule was located in an MgO cylinder in a graphite stepped heater with a ZrO₂ thermal insulator. Tungsten carbide anvils with a 15 mm truncated edge length were used to generate high pressure together with a Cr₂O₃-doped MgO octahedron with a 25 mm edge length as a pressure medium. Sample pressures were estimated from the hydraulic oil pressure based on calibrations using the phase transitions of Bi and Mg₂SiO₄ polymorphs. Temperatures were measured using a W97%Re3%-W75%Re25% thermocouple whose junction was located near one end of the capsule. The sample was pressurized to 5 GPa in 4 h, heated to a temperature of 1473 K at a rate of 50 K/min, and kept at this temperature for 16 h. After annealing, the sample was quenched by switching off the heating power, and decompressed to ambient pressure in 16 h. After hydration, the sample was shaped as a cube with edge length of 1 to 1.2 mm to remove the graphite and magnesite on the surface.

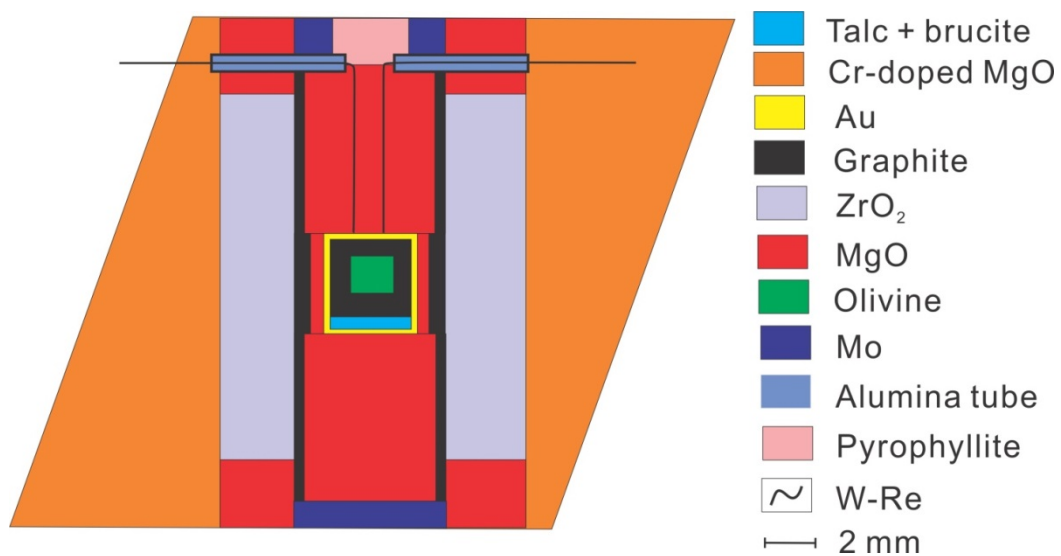


Figure 1. The sample assembly used in the multi-anvil hydration experiments.

Deformation experiments

Deformation experiments were conducted using a Kawai-type multi-anvil apparatus at pressures of 2 to 5 GPa and temperatures of 1473 and 1573 K. Figure 2 shows the experimental setup. A square hole was made at the center of an MgO slice to accommodate the cubic olivine crystal in a unique orientation. The MgO slice with the olivine crystal was sandwiched between two crushable alumina pistons. The shear geometry was in the [100] direction on the (001) plane. In order to prevent dehydration of hydrated olivine at high temperatures, thin layers of talc + brucite mixtures were put between the MgO slice and alumina pistons in the deformation experiments under hydrous conditions. The sample and pistons were placed in a welded Pt capsule. Two columns of crushable alumina were placed on both ends of the capsule. The other parts of assembly were the same as those used in the hydration experiments.

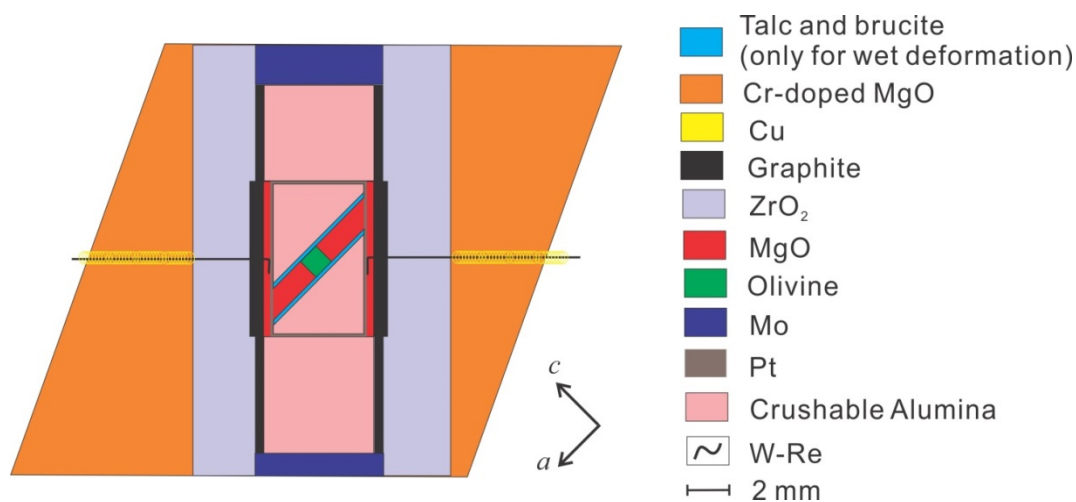


Figure 2. The sample assembly used in the multi-anvil high-pressure deformation experiments. The crystallographic orientation of the olivine single crystal is also shown.

The cell assembly was first pressurized to a target pressure at ambient temperature in 4 h. A target temperature was reached in 15 min, and kept constant for 15 min to sinter the crushable alumina. The sample was then further compressed by increasing press load of 0.2 MN in 15 min to deform the sample. After the deformation, the sample was quenched by switching off the heating power, and then decompressed to ambient pressure for more than 16 h.

FT-IR measurements

Water contents of the samples before and after deformation were determined by un-polarized FT-IR spectroscopy with 200 scans for each spectrum at a resolution of 1 cm^{-1} . Spectra were taken at the rim and center of the sample after deformation to investigate the water distribution inside the sample. The light paths were perpendicular to the (010) planes of the samples. Paterson (1982) calibration was used for calculation of the water contents in order to directly compare our results with those obtained by Jung and Karato (2001) and Katayama et al. (2004).

TEM observation

The deformed samples were double-side polished parallel to the (001) planes to thicknesses ranging from 23 to 35 μm and fixed on glass slides. After removing olivine from the glass slide, an Ar ion-milling method was used to make the sample thinner, with a voltage of 4.5 kV and incident angles of 4 to 8° from the top and bottom of the ion-bombardment, and the total thinning time varying between 14 to 25 h depending on the thicknesses and size of each sample. TEM observations were performed with a FEI Titan G2 80-200 S/TEM equipped with 4 silicon drift detectors for energy-dispersive X-ray spectrometry, operating at an acceleration voltage of 200 kV. Dislocation microstructures were examined by dark-field (DF, Bragg condition, deviation parameter, $s = 0$) and weak-beam dark-field (WBDF, $s > 0$) imaging and selected-area electron diffraction (SAED). We chose diffraction vectors with $\mathbf{g} =$

400 to observe the [100] dislocations which should be the Burgers vector of the deformed olivine in the [100] direction on the (001) plane. If there are [100](001) dislocations, they should be visible as elongated dislocation lines on the plane. We measured the total length of dislocation lines per area and calculated a dislocation density based on the assumption that the thickness of the TEM foils is 250 nm.

6.4 Results

Table 1 shows the experimental conditions together with the water content of the samples before and after deformation. The FT-IR spectra of hydrous samples before and after deformation were shown in Fig. 3. The water contents in these samples increased only slightly after deformation, indicating that a small amount of water was absorbed from the layers of talc and brucite mixture during deformation. Water was homogeneously distributed in the samples as is seen from the fact that the FT-IR spectra in the center and rim of the crystals are almost identical (Fig. 3). The water contents in the samples are below the water solubility in olivine (Kohlstedt et al., 1996).

Table 1. Summary of experimental conditions and water content before and after deformation

No	<i>T</i> (K)	<i>P</i> (GPa)	Dislocation density (μm^{-2})	Stress (MPa)	Water before (ppm H/Si)	Water after (ppm H/Si)
H4477*	1473	2	0.2	40	37	61
Z1486*	1573	3	1.6	175	37	73
Z1711 [#]	1473	5	3.5	305	863	970
Z1714 [#]	1473	2	1.5	167	545	583

* Anhydrous deformation experiment. No layer of mixture of talc and brucite was added.

[#] Hydrous deformation experiment. Layers of a mixture of talc and brucite were added.

Stresses during experiments were estimated from the dislocation density using the relationship between dislocation density and stresses given by Karato and Jung (2003). The dislocation density and estimated stresses are given in Table 1.

TEM images of dislocations activated under anhydrous conditions are shown in Fig. 4. The sample after deformation contained water less than 80 ppm H/Si, which falls into the region of A-type fabric in Katayama et al. (2004). We found only dislocations with the Burgers vector of $[100]$ elongated in the $[001]$ direction in these samples. No line contrast of dislocations was observed on the (001) plane, indicating that (001) is not a slip plane under the experimental conditions.

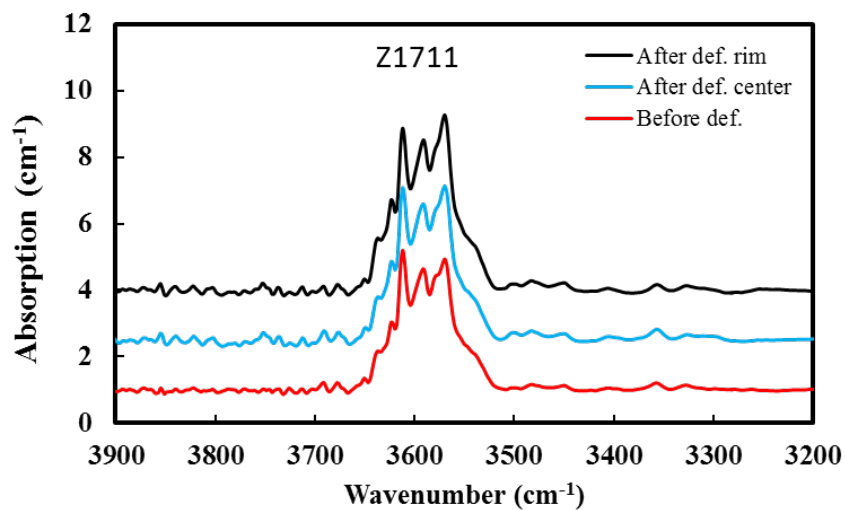
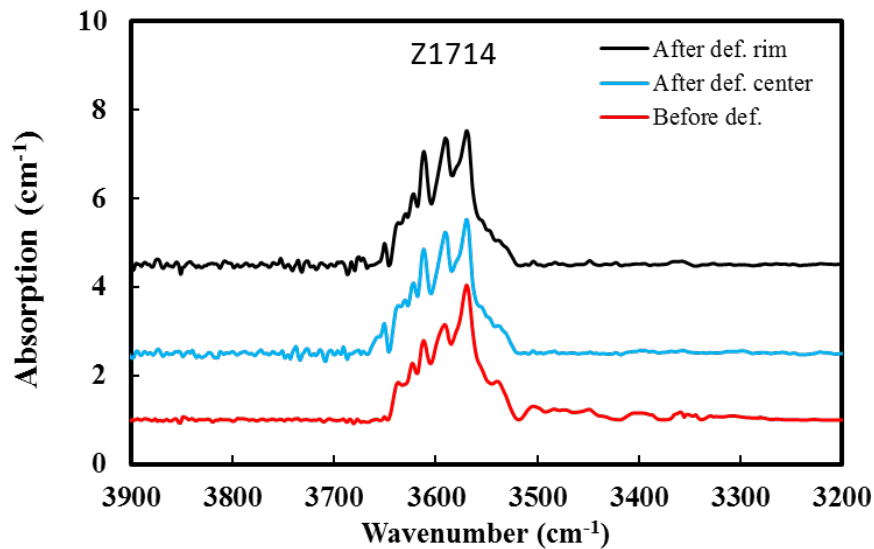


Figure 3. FT-IR spectra of samples deformed at 1473 K under hydrous conditions after base line correction and thickness normalization to 1 cm. (a) sample deformed at 2 GPa. (b) sample deformed at 5 GPa. The red spectra were obtained before deformation. The blue and black spectra were obtained after deformation at the sample center and rim, respectively.

Typical dislocation microstructures activated under hydrous conditions are shown in Fig. 5. Dislocation lines and loops with the Burgers vector of $[100]$ were observed on the (001) plane, suggesting that the $[100](001)$ slip system was activated. The majority of dislocation lines elongate in the $[010]$ direction, indicating their edge characters. The dislocation loops consist of long edge segment (b -elongated) and short screw segment (a -elongated), indicating lower mobility of the edge components in comparison with the screw components. Some screw dislocations have cross-slip (Fig 5c) or were pinned by jogs (Fig. 5b and 5c) and edge dipoles (Fig. 5c), which are related to movements of jogged screw dislocations. The $[100]$ short edge dislocations are likely to be debris which originates from edge dipoles (Fig. 5a and 5c) or dislocations on other $(0kl)$ slip planes (e.g. Green and Radcliffe, 1972). The $[100]$ dislocations elongated to the $[001]$ directions, which are dominant under anhydrous conditions, also exist.

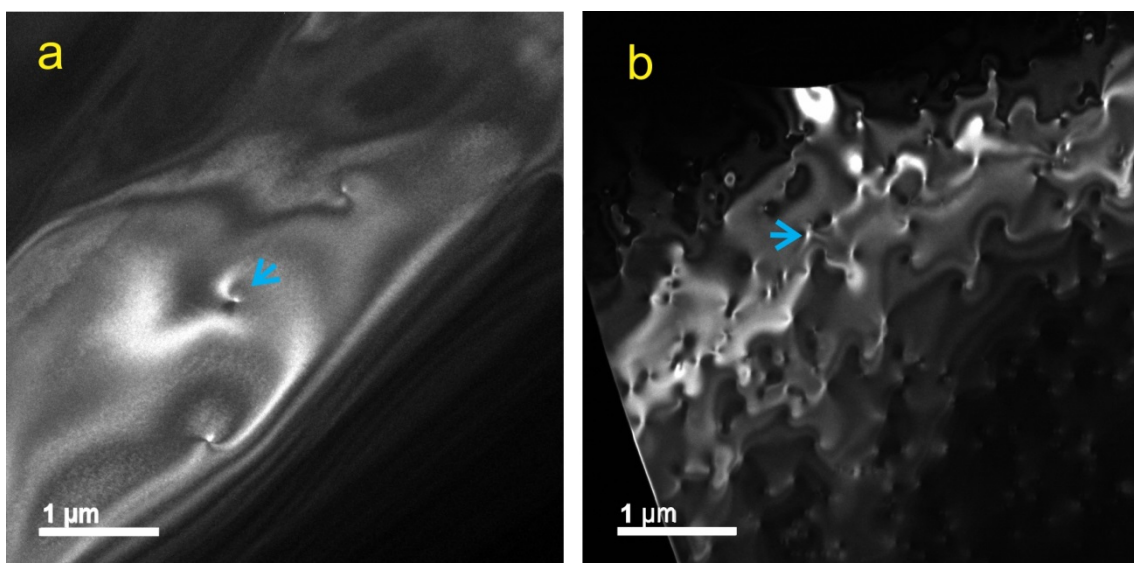


Figure 4. WBDF images showing character of [100] dislocations in the sample deformed under anhydrous conditions. a) sample deformed at 2 GPa and 1473 K. b) sample deformed at 3 GPa and 1573 K. The all images were taken using $g = 400$. The [100] dislocations along the [001] direction are indicated by blue arrows.

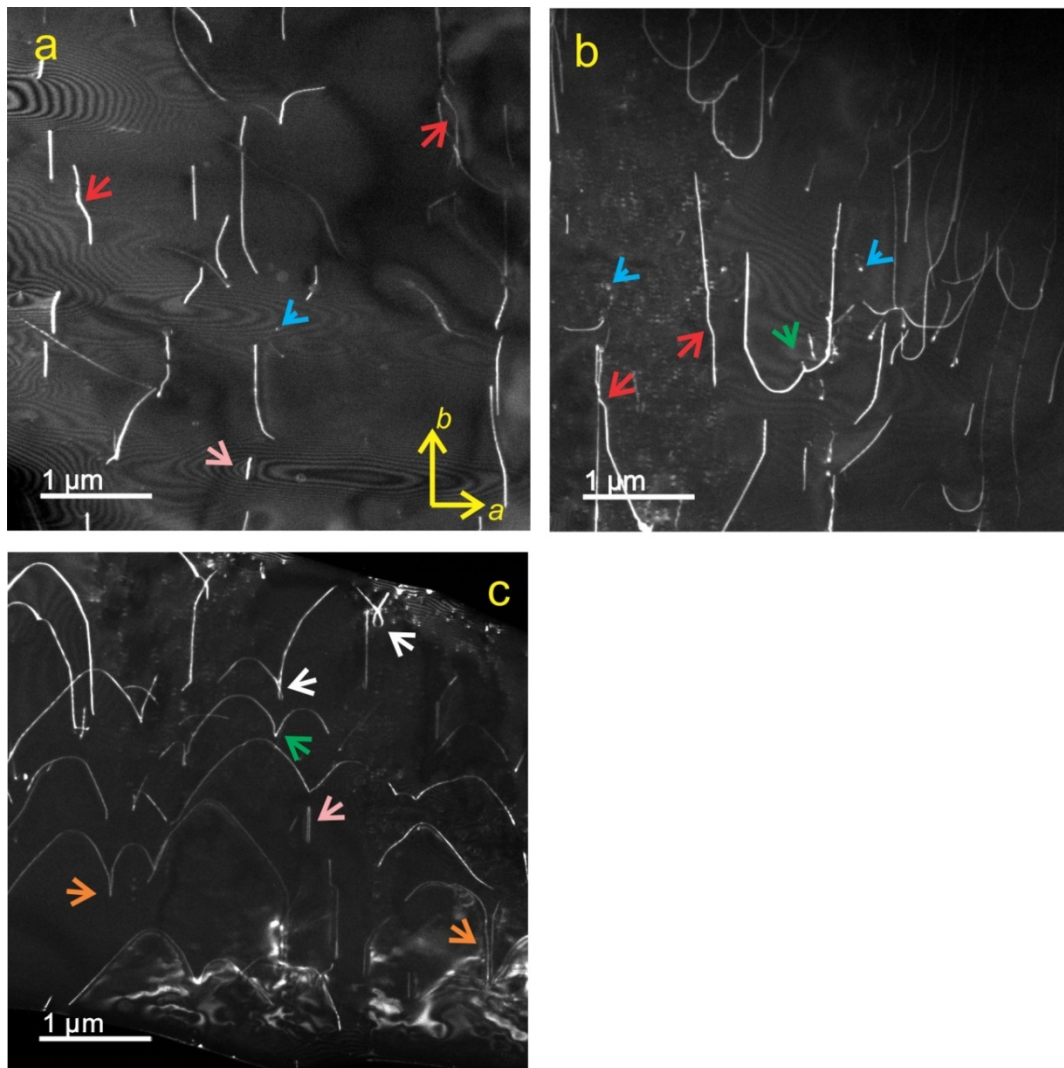


Figure 5. WBDF images showing dislocation character of sample deformed at 1473 K under hydrous conditions. Crystallographic axes are shown in a). a) sample deformed at 2 GPa. b) and c) hydrous sample deformed at 5 GPa. The all images were taken using $g = 400$. The [100] dislocations on the (001) plane are generally curved, and kinks are shown by red arrows. Screw dislocations have cross-slips (white arrows) and are pinned by jogs (green arrows) or edge dipoles (orange arrows). Movement of jogged screw dislocations left a lot of short edge

segments (pink arrows). The [100] dislocations along the [001] direction are indicated by blue arrows.

6.5 Discussion

Comparison of the dislocation microstructures with previous studies

The [100](001) slip system has been reported by previous studies (Durham et al., 1977; Bai and Kohlstedt 1993) under anhydrous and high-temperature (>1623 K) conditions. Durham et al. (1977) reported that such dislocations exhibit a peculiar microstructure with zigzag line configurations corresponding to the stabilization of $\langle 110 \rangle$ segments. Bai and Kohlstedt (1992) found that the dislocation structures developed at high oxygen fugacity are the same as those in Durham et al. (1977). At low oxygen fugacity, Bai and Kohlstedt (1992) found that the dislocation configuration consists of long straight screw and short curved edge segments. The dislocation configuration developed under hydrous conditions in the present study is quite different from these previous studies. Dislocations developed under hydrous conditions in this study consist of long edge and short curved screw segments instead of long straight screw and short curved edge dislocations, indicating that glide velocity of screw dislocation is more enhanced by water incorporation than that of edge dislocations. Moreover, no $\langle 110 \rangle$ zigzag edge dislocation line was observed in the present study. Instead, edge dislocation lines are curved and have kinks. The observations that dislocation lines are generally curved and kinked indicate that the Peierls stress for this slip system is reduced by water incorporation and dislocation glide velocity is enhanced.

The mechanism of activation of the [100](001) slip system due to water incorporation

The olivine structure has an orthorhombic symmetry with the space group $Pbnm$. This structure has three different oxygen sites (O1, O2, O3), two different metal sites (M1, M2) and one silicon site. O1, O2, M2 and Si lie on mirror planes, while M1 lies on an inversion center. O3 lies in a general position. A slip on the (001) plane needs to cut Si-O or/and M-O bonds. Since Si-O bonding has higher energy than M-O bonding, the slip plane prefers to avoid cutting Si-O bonds, as shown in Fig. 6. However, this plane cuts 10 M-O bonds in one unit cell. In the case of (010) slip plane, which is an easy slip plane for olivine, only 4 M-O bonds are needed to be cut. Therefore, the high energy required to break chemical bonding perpendicular to the [001] direction can explain why this slip system was activated at high temperatures (Bai and Kohlstedt, 1993; Durham et al., 1997) but was not activated in the samples that were deformed under low-temperature and anhydrous conditions in our study.

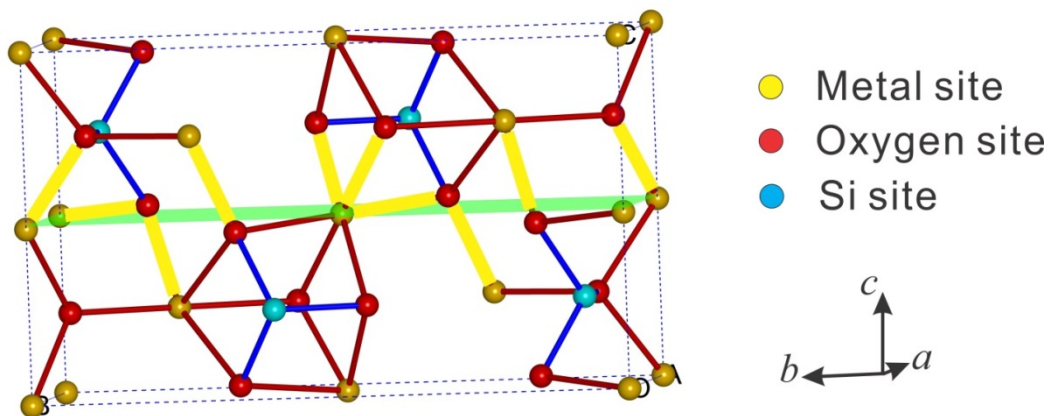


Figure 6. Olivine structure viewed from near [100] direction. The green plane shows a (001) slip plane cut only M-O bonds. Red sticks indicate M-O bonds. Blue sticks indicate Si-O bonds. M-O bonds cut by the slip plane are indicated by yellow sticks.

Crystallographic sites where H is incorporated in the olivine structure are still under debate (Berry et al., 2005; Keppler and Bolfan-Casanova, 2006; Kohlstedt et al., 1996;

Lemaire et al., 2004; Matveev et al., 2001; Matveev et al., 2004; Mosenfelder et al., 2006; Zhao et al., 2004). Nevertheless, there is an agreement on the direction of O-H bonding based on polarized infra-red (IR) spectroscopy. The directions of O-H bonding suggested by IR spectroscopy are generally parallel to the [100] and [001] axes but not parallel to the [010] axis in olivine (e.g. Bell et al., 2003; Jamtveit et al., 2001; Lemaire et al., 2004). The [001] aligned O-H bond certainly weakens the bond strength in the [001] direction, which makes the (001) slip possible.

6.6 Implications

The decrease of seismic anisotropy with depth has been observed by several studies (Dziewonski and Anderson, 1981; Gung et al., 2003; Montagner and Kennett, 1996; Nettles and Dziewonski, 2008; Visser et al., 2008). One explanation is that olivine fabric changes from A- to E-type due to water (Katayama et al., 2004; Karato et al., 2008). However, the [100](001) slip system was only reported under anhydrous conditions (Bai and Kohlstedt, 1992; Durham et al., 1977). Whether this slip system can be activated under hydrous conditions was unclear before the present study. Our TEM observation of the samples deformed under anhydrous and hydrous conditions suggests that water facilitates activation of the [100](001) slip at relatively low temperatures. The physical reason for the activation is the reduction of Peierls stresses because of water incorporation, which was revealed by the dislocation structures. Therefore, the E-type fabric can exist under hydrous conditions, and the weak seismic anisotropy of the asthenosphere could be explained by the predominance of this fabric.

6.7 Acknowledgements

We acknowledge F. Heidelbach and P. O'Brien for providing the olivine single crystals and T. Boffa-Ballaran for instructing the single crystal X-ray diffractometry. We thank technicians in BGI for the sample and assembly preparation. This research was supported by

DFG grants to TK (KA3434/3-1, KA3434/7-1, KA3434/8-1 and KA3434/9-1) and by the annual budget of BGI.

6.8 References

- Angel, R., and Finger, L. (2011) SINGLE: a program to control single-crystal diffractometers. *Journal of Applied Crystallography*, 44(1), 247-251.
- Bai, Q., and Kohlstedt, D.L. (1992) High-temperature creep of olivine single crystals, 2. dislocation structures. *Tectonophysics*, 206(1–2), 1-29.
- Bell, D.R., Rossman, G.R., Maldener, J., Endisch, D., and Rauch, F. (2003) Hydroxide in olivine: A quantitative determination of the absolute amount and calibration of the IR spectrum. *Journal of Geophysical Research-Solid Earth*, 108(B2), 9.
- Berry, A.J., Hermann, J.r., O'Neill, H.S., and Foran, G.J. (2005) Fingerprinting the water site in mantle olivine. *Geology*, 33(11), 869-872.
- Darot, M., and Gueguen, Y. (1981) High - temperature creep of forsterite single crystals. *Journal of Geophysical Research: Solid Earth*, 86(B7), 6219-6234.
- Durham, W.B., and Goetze, C. (1977) A comparison of the creep properties of pure forsterite and iron-bearing olivine. *Tectonophysics*, 40(3), T15-T18.
- Durham, W.B., Goetze, C., and Blake, B. (1977) PLASTIC-FLOW OF ORIENTED SINGLE-CRYSTALS OF OLIVINE .2. OBSERVATIONS AND INTERPRETATIONS OF DISLOCATION-STRUCTURES. *Journal of Geophysical Research*, 82(36), 5755-5770.
- Dziewonski, A.M., and Anderson, D.L. (1981) Preliminary reference Earth model. *Physics of the Earth and Planetary Interiors*, 25(4), 297-356.
- Gaboriaud, R., Darot, M., Gueguen, Y., and Woirgard, J. (1981) Dislocations in olivine indented at low temperatures. *Physics and Chemistry of Minerals*, 7(2), 100-104.
- Goetze, C., and Kohlstedt, D.L. (1973) Laboratory study of dislocation climb and diffusion in olivine. *Journal of Geophysical Research*, 78(26), 5961-5971.

- Gose, J., Schmaedicke, E., Markowitz, M., and Beran, A. (2010) OH point defects in olivine from Pakistan. *Mineralogy and Petrology*, 99(1-2), 105-111.
- Green, H., and Radcliffe, S. (1972) Dislocation mechanisms in olivine and flow in the upper mantle. *Earth and Planetary Science Letters*, 15(3), 239-247.
- Gung, Y., Panning, M., and Romanowicz, B. (2003) Global anisotropy and the thickness of continents. *Nature*, 422(6933), 707-711.
- Hirth, G., and Kohlstedt, D.L. (1996) Water in the oceanic upper mantle: implications for rheology, melt extraction and the evolution of the lithosphere. *Earth and Planetary Science Letters*, 144(1-2), 93-108.
- Ismail, W.B., and Mainprice, D. (1998) An olivine fabric database: an overview of upper mantle fabrics and seismic anisotropy. *Tectonophysics*, 296(1-2), 145-157.
- Jamtveit, B., Brooker, R., Brooks, K., Larsen, L.M., and Pedersen, T. (2001) The water content of olivines from the North Atlantic Volcanic Province. *Earth and Planetary Science Letters*, 186(3-4), 401-415.
- Jung, H., and Karato, S.-i. (2001) Water-Induced Fabric Transitions in Olivine. *Science*, 293(5534), 1460-1463.
- Jung, H., Katayama, I., Jiang, Z., Hiraga, T., and Karato, S. (2006) Effect of water and stress on the lattice-preferred orientation of olivine. *Tectonophysics*, 421(1-2), 1-22.
- Karato, S.-I., and Jung, H. (2003) Effects of pressure on high-temperature dislocation creep in olivine. *Philosophical Magazine*, 83(3), 401-414.
- Karato, S.-i., Jung, H., Katayama, I., and Skemer, P. (2008) Geodynamic Significance of Seismic Anisotropy of the Upper Mantle: New Insights from Laboratory Studies. *Annual Review of Earth and Planetary Sciences*, 36(1), 59-95.
- Katayama, I., Jung, H., and Karato, S.-i. (2004) New type of olivine fabric from deformation experiments at modest water content and low stress. *Geology*, 32(12), 1045-1048.
- Keppler, H., and Bolfan-Casanova, N. (2006) Thermodynamics of water solubility and partitioning. *Reviews in Mineralogy and Geochemistry*, 62(1), 193-230.

- Kohlstedt, D., Keppeler, H., and Rubie, D. (1996) Solubility of water in the α , β and γ phases of (Mg, Fe) 2SiO_4 . *Contributions to Mineralogy and Petrology*, 123(4), 345-357.
- Kohlstedt, D.L., and Goetze, C. (1974) Low-stress high-temperature creep in olivine single crystals. *Journal of Geophysical Research*, 79(14), 2045-2051.
- Kumazawa, M., and Anderson, O.L. (1969) Elastic moduli, pressure derivatives, and temperature derivatives of single-crystal olivine and single-crystal forsterite. *Journal of Geophysical Research*, 74(25), 5961-5972.
- Lemaire, C., Kohn, S., and Brooker, R. (2004) The effect of silica activity on the incorporation mechanisms of water in synthetic forsterite: a polarised infrared spectroscopic study. *Contributions to Mineralogy and Petrology*, 147(1), 48-57.
- Mainprice, D. (2007) Seismic anisotropy of the deep Earth from a mineral and rock 1022 physics perspective. Schubert, G. *Treatise in Geophysics Volume 2* pp437-492. Oxford.
- Matveev, S., O'Neill, H.S.C., Ballhaus, C., Taylor, W.R., and Green, D. (2001) Effect of silica activity on OH⁻ IR spectra of olivine: implications for low- a SiO₂ mantle metasomatism. *Journal of Petrology*, 42(4), 721-729.
- Matveev, S., Portnyagin, M., Ballhaus, C., Brooker, R., and Geiger, C. (2004) FTIR spectrum of phenocryst olivine as an indicator of silica saturation in magmas. *Journal of Petrology*, 46(3), 603-614.
- Michibayashi, K., Mainprice, D., Fujii, A., Uehara, S., Shinkai, Y., Kondo, Y., Ohara, Y., Ishii, T., Fryer, P., and Bloomer, S.H. (2016) Natural olivine crystal-fabrics in the western Pacific convergence region: A new method to identify fabric type. *Earth and Planetary Science Letters*, 443, 70-80.
- Montagner, J.P., and Kennett, B.L.N. (1996) How to reconcile body-wave and normal-mode reference earth models. *Geophysical Journal International*, 125(1), 229-248.
- Mosenfelder, J.L., Deligne, N.I., Asimow, P.D., and Rossman, G.R. (2006) Hydrogen incorporation in olivine from 2–12 GPa. *American Mineralogist*, 91(2-3), 285-294.

- Mussi, A., Cordier, P., Demouchy, S., and Vanmansart, C. (2014) Characterization of the glide planes of the [001] screw dislocations in olivine using electron tomography. *Physics and Chemistry of Minerals*, 41(7), 537-545.
- Nettles, M., and Dziewonski, A.M. (2008) Radially anisotropic shear velocity structure of the upper mantle globally and beneath North America. *Journal of Geophysical Research-Solid Earth*, 113(B2), 27.
- Ohuchi, T., Kawazoe, T., Higo, Y., Funakoshi, K.-i., Suzuki, A., Kikegawa, T., and Irifune, T. (2015) Dislocation-accommodated grain boundary sliding as the major deformation mechanism of olivine in the Earth's upper mantle. *Science advances*, 1(9), e1500360.
- Paterson, M. (1982) The determination of hydroxyl by infrared absorption in quartz, silicate glasses, and similar materials. *Bulletin de la Societe Francaise de Mineralogie*, 105, 20-29.
- Phakey, P., Dollinger, G., and Christie, J. (1972) Transmission electron microscopy of experimentally deformed olivine crystals. *Flow and Fracture of rocks*, 117-138.
- Ringwood, A.E. (1991) Phase transformations and their bearing on the constitution and dynamics of the mantle. *Geochimica et Cosmochimica Acta*, 55(8), 2083-2110.
- Tommasi, A., and Vauchez, A. (2015) Heterogeneity and anisotropy in the lithospheric mantle. *Tectonophysics*, 661, 11-37.
- Visser, K., Trampert, J., Lebedev, S., and Kennett, B.L.N. (2008) Probability of radial anisotropy in the deep mantle. *Earth and Planetary Science Letters*, 270(3-4), 241-250.
- Zhao, Y.-H., Ginsberg, S., and Kohlstedt, D. (2004) Solubility of hydrogen in olivine: dependence on temperature and iron content. *Contributions to Mineralogy and Petrology*, 147(2), 155-161.

7 Small effect of water on olivine dislocation creep

Lin Wang^{a,*}, Nobuyoshi Miyajima^a, Takaaki Kawazoe^a, and Tomoo Katsura^a

^a Bayerisches Geoinstitut, University of Bayreuth, 95440 Bayreuth, Germany.

7.1 Abstract

Dislocation recovery experiments were conducted on pre-deformed olivine single crystals at 1,473 K, 5 GPa, and oxygen fugacity near the enstatite-magnesite-olivine-graphite (EMOG) buffer at water contents ranging from 5 to 90 wt. ppm to determine the annihilation rates for [001] dislocations on the (001) plane. Olivine single crystals were first hydrated or dehydrated at 5 GPa, 1473 K or room pressure, 1473 K, respectively. The pre-annealed olivine was then deformed to activate the desired slip systems under simple shear geometry and then annealed at target conditions. The dislocation characters change from screw to edge with increasing water contents. The dislocation annihilation rate constants increase with water content with a power of 0.3. Since the rate constant is proportional to dislocation mobility, we conclude that water has small effect on olivine dislocation creep. Hence, the softening of asthenosphere cannot be explained by the hydrous weakening.

7.2 Introduction

Olivine is the most abundant and weakest mineral in the upper mantle, and therefore its rheological properties are fundamental to understand mantle dynamics. Dislocation creep, which is facilitated by motion of dislocations, is considered as one of the important

mechanisms for olivine deformation in the upper mantle (e.g. Fei et al., 2016; Hirth and Kohlstedt, 2003; Karato and Wu, 1993), and consequently determine the upper mantle viscosity to a great extent. In addition, the lattice preferred orientation (LPO), or fabric, of olivine, which is a consequence of dislocation creep, is the main reason for the upper mantle seismic anisotropy. Since dislocation creep is influenced by thermodynamic parameters, such as P , T , water content, it is important to understand the effects of these parameters on dislocation creep.

Among all the parameters, the effect of water on the olivine dislocation creep has been debated recently. Deformation experiments on olivine aggregate demonstrated that the creep rate of olivine is enhanced by water incorporation with a power of 1.2 (Hirth and Kohlstedt, 2003). On the other hand, recent diffusion experiments (Fei et al., 2016; Fei et al., 2013) suggested a small effect on the olivine rheology based on the assumption that olivine creep is controlled by Si diffusion. Since the asthenosphere contains certain amounts of water (Hirth and Kohlstedt, 1996), the viscosities of the asthenosphere estimated by these two methods differ by orders of magnitude.

Another debate on the effect of water on olivine rheology is that whether water-induced fabric transition exists or not. Deformation experiments (Jung and Karato, 2001; Jung et al., 2006; Katayama et al., 2004) suggested that the dominant fabric changes from A- to E- to C-type with increasing water content, indicating different slip systems have different water dependences. However, diffusion experiments (Costa and Chakraborty, 2008; Fei et al., 2013) suggested that the effect of water on Si lattice diffusion in olivine is isotropic. Accordingly, it is unlikely to have water-induced fabric transition if dislocation creep is controlled by Si lattice diffusion. Therefore, it is essential to constrain the effect of water on olivine dislocation creep for different slip systems.

Both deformation and diffusion techniques have limitations in determining the effect of water on olivine dislocation creep. In one hand, strain rates in deformation experiments are in the range of 10^{-6} to 10^{-4} s^{-1} , which are nearly ten orders of magnitude higher than those in the asthenosphere. The rate-limiting process of dislocation creep may change at different strain

rates. Therefore, the extrapolation of deformation results to natural strain rate conditions may be problematic. In addition, the majority of deformation experiments were conducted on polycrystalline olivine samples under water-saturated conditions, which is not the case at most regions of the asthenosphere. The possible existence of free water in grain boundaries may also bias the results. On the other hand, connection between dislocation creep rate and Si self-diffusivity is rather indirect. Application of diffusion results on deformation has to base on certain models, which need various assumptions. In addition, steady-state deformation requires the same rates of dislocation production and annihilation. This indicates interactions between dislocations must occur during dislocation creep, which cannot be investigated by diffusion experiments.

For these reasons, we use dislocation recovery method in this study to study dislocation motions. The activation of [001](100) slip system is responsible for the C-type fabric in olivine. Deformation experiments demonstrated that C-type fabric dominates at high water content (Jung and Karato, 2001), indicating that this slip system must have the largest water dependence among all slip systems in olivine. Therefore, the water dependence of this slip system represents the maximum water dependence of olivine dislocation creep. We conducted dislocation recovery experiments to dislocations produced by the [001](100) slip system (hereafter called *c*-dislocations) at various water contents at a pressure of 5 GPa and a temperature of 1473 K to get water dependence of dislocation annihilation rate constants of this kind of dislocations. Since annihilation rate constants are considered to be proportional to dislocation mobility, the water dependence of rate constants should be identical to that of dislocation motions. Our results show that the rate constants of *c*-dislocations increase with water content only with a power of 0.3. Therefore, the effect of water on olivine dislocation creep is small.

7.3 Experimental Procedures

Sample Preparation

Single crystals of natural olivine from Pakistan were employed in this study. The same olivine was used in our previous studies (Wang et al., 2016; 2017). The *a*-axis of each crystal was determined using a Huber single-crystal diffractometer operated by SINGLE2014 (Angel and Finger, 2011). The oriented olivine crystals were mounted in epoxy resin with the (100) plane exposed to the surface, and then polished using diamond powder with a grain size of 0.25 μm . The [010] and [001] directions were determined by means of electron backscattered diffraction (EBSD). The cube with 1.5 mm edge length was shaped from the oriented crystal along its crystallographic planes.

Hydration/dehydration experiments

The olivine cubes were hydrated or dehydrated before deformation. In dehydration experiments, the cubes were put into a Pt basket and annealed at ambient pressure and a temperature of 1473 K for 12 h in a CO-CO₂ gas mixing furnace. The oxygen partial pressure was controlled at $10^{-7.5}$ MPa, which was near the enstatite-magnesite-olivine-graphite (EMOG) buffer.

Hydration experiments were conducted at a pressure of 5 GPa and a temperature of 1473 K using a Kawai-type multi-anvil apparatus at University of Bayreuth. The cell assembly is shown in Fig. 1. A single-crystal olivine cube was loaded into a gold capsule with outer and inner diameters of 3.7 and 3.2 mm, respectively, whose one end was sealed. A mixture of talc, brucite and FeO powders (weight ratio 1.7:1:0.3) was loaded at the sealed end of the capsule. This mixture gives the composition of $(\text{Mg}_{0.9}\text{Fe}_{0.1})_2\text{SiO}_4$ and $(\text{Mg}_{0.9}\text{Fe}_{0.1})\text{SiO}_3$ with molar ratio of 9:1. It was used as a water source and also to control the silica activity of the sample. Graphite powder was used to surround the cube to prevent its mechanical damage during compression and to constrain the oxygen fugacity inside the capsule near the EMOG buffer

conditions. Various water contents in the samples were obtained by varying the ratio of the water source to graphite. Open ends of the capsules were closed and sealed by arc welding after loading. The gold capsule was located in an MgO cylinder in a graphite stepped heater with a ZrO₂ thermal insulator. Tungsten carbide anvils with a 15 mm truncated edge length were used to generate high pressure together with a Cr₂O₃-doped MgO octahedron with a 25 mm edge length as a pressure medium. Sample pressures were estimated based on calibration against the hydraulic oil pressure using the phase transitions of Bi at ambient temperature and Mg₂SiO₄ polymorphs. Temperatures were measured using a W97%Re3%-W75%Re25% thermocouple whose junction was located near one end of the capsule. The samples were pressurized to 5 GPa in 4 h, heated to a temperature of 1473 K at a rate of 50 K/min, and kept at this temperature for more than 12 h. After annealing, the samples were quenched by switching off the heating power, and decompressed to ambient pressure in 16 h. After hydration, the samples were polished to be cubes with an edge length of 1 to 1.2 mm to remove graphite and magnesite on the surfaces.

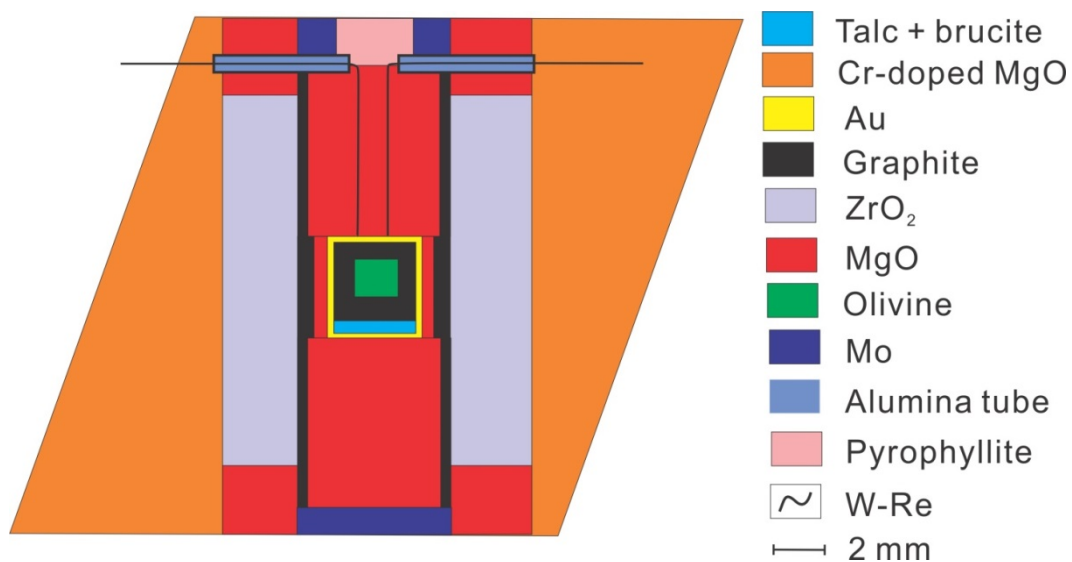


Figure 1. The sample assembly used in the multi-anvil hydration experiments.

Deformation experiments

Deformation experiments were conducted using a Kawai-type multi-anvil apparatus at

pressures of 5 GPa and temperatures of 1473. Figure 2 shows the experimental setup. The setup is similar to that used in Wang et al., (2016) except for the following three points. One is that olivine was oriented in the shear geometry in the [001] direction on the (100) plane. The second one is that thin layers of talc + brucite+ FeO mixtures were put between the MgO slice and alumina pistons in hydrous deformation experiments in order to prevent dehydration of olivine at high temperatures. The third one is that the Pt capsule was welded.

The samples were first pressurized to a target pressure at ambient temperature for 4 h. A target temperature was reached in 15 min, and kept constant for 15 min to sinter the crushable alumina. The samples were then further compressed by increasing press load of 0.2 MN in 15 min for deformation. After the deformation, the samples were quenched by switching off the heating power, and then decompressed to ambient pressure for more than 16 h.

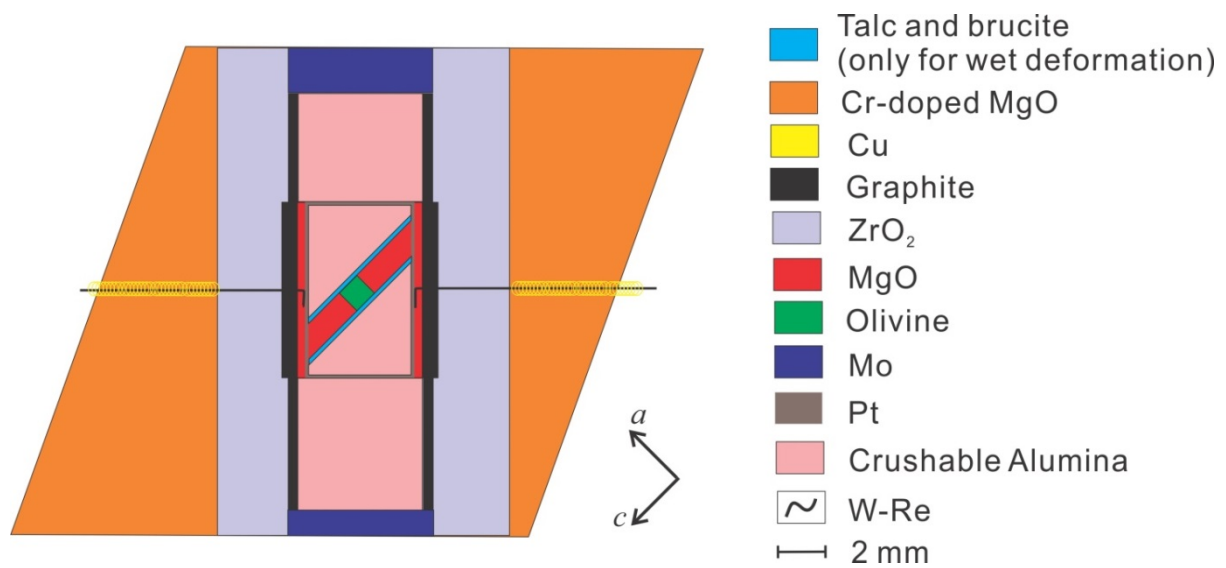


Figure 2. The sample assembly used in the multi-anvil high-pressure deformation experiments. The crystallographic orientation is also shown.

TEM observation

Deformed samples were fixed on glass slides and double-side polished parallel to the (100) planes to thicknesses ranging from 23 to 35 μm . After removing olivine from the glass

slide, an Ar ion-milling method was used to make the sample thinner, with a voltage of 4.5 kV and incident angles of 4 to 8° from the top and bottom of the ion-bombardment, and the total thinning time varying between 14 to 25 h depending on the thicknesses and size of each sample. TEM observations were performed with a FEI Titan G2 80-200 S/TEM equipped with 4 SDD energy-dispersive X-ray spectrometers, operating at an acceleration voltage of 200 kV. Dislocation microstructures were examined by dark-field (DF) and weak-beam dark-field (WBDF) imaging and selected-area electron diffraction (SAED). We chose the diffraction vector with $g = 004$ to observe the [001] dislocations and determine their characters. c -edge dislocations would elongate in [010] while c -screws would elongate in [001].

Recovery experiments

The rest of the deformed single crystals were cut into 4 pieces and paired into 2 groups. If c -edge dislocations dominate, pieces in the same group shear a common (010) plane. If c -screw dislocations dominate, pieces in the same group shear a common (001) plane. One piece in each group was used in the annealing experiments. The other was used to determine the dislocation density before annealing.

Recovery experiments were conducted at a pressure of 5 GPa and a temperature of 1473 K using a Kawai-type multi-anvil apparatus at University of Bayreuth. The cell assembly is the same as that in hydration experiments. The same amounts of water source as those in the corresponding hydration experiments were used in order to keep water contents remain unchanged during annealing. No water source was added in anhydrous recovery experiments.

FT-IR measurements

Water contents of the samples before and after annealing were determined by un-polarized FT-IR spectroscopy with 200 scans for each spectrum at a resolution of 1 cm^{-1} . Spectra were taken at the rim and center of the sample after annealing to investigate the water

distributions inside the sample. The light paths were perpendicular to the (010) planes of the samples. Paterson (1982) calibration was used for calculation of the water contents in order to compare our results with those obtained by Hirth and Kohlstedt., (2003). We emphasize that, as is shown later, we will obtain water content dependence of dislocation annihilation rate constant, which is independent from choice of calibration.

Measurement of dislocation density and data reduction

Dislocations were observed using the same oxidation decoration technique as Wang et al. (2016), except for the oxidation temperature, which is 800°C. The corresponding areas away from subgrain boundary on the common (001) or (010) plane in the initial and annealed pieces from the same group were observed to determine the change in dislocation density before and after annealing.

The annihilation rate constants were calculated using the second-order dislocation recovery kinetics (Karato and Ogawa, 1982; Kohlstedt et al., 1980)

$$k = \frac{\frac{1}{\rho_f} - \frac{1}{\rho_i}}{t}, \quad (2)$$

where ρ_f and ρ_i are the dislocation density after and before annealing, respectively, and t is the annealing time. The k at different water contents were fitted to the power law:

$$k = k_0 C_{\text{OH}}^r \quad (3)$$

where k_0 is a constant, C_{OH} is water content, r is the water exponent. As discussed above, this exponent should represent that of dislocation creep.

7.4 Results

Table 1 shows recovery experimental results together with the annealing conditions.

Figure 3 shows TEM observations of dislocation structures after deformation without annealing. At lower water contents (< 25 wt. ppm), [001]-elongated *c*-screw dislocations are dominant, while [010]-elongated *c*-edge dislocations dominate at higher water contents. This indicates dislocation motions are controlled by screw and edge dislocations at lower and higher water contents, respectively. For this reason, the dislocation densities are counted using the images on the (001) and (010) plane in high-water content and low-water content samples to count *c*-screw and *c*-edge dislocations, respectively. Fig. 4 shows the decorated dislocations before and after annealing. The decrease in dislocation density was observed after annealing.

Table 1. Summary of experiment conditions and results.¹

No	Water before (wt. ppm)	Water after (wt. ppm)	ρ_i (μm^{-2})	ρ_f (μm^{-2})	t (h)	Log k ()
Z1483*	5	5	8.09±0.95	0.46±0.04	18.2	16.5 ± 0.1
Z1495*	5	7	1.31±0.16	0.66±0.04	15.5	16.9 ± 0.1
Z1675*	19	25	0.33±0.11	0.20±0.05	10	-16.3 ± 0.4
Z1712 [#]	86	91	1.91±0.1	0.88±0.09	6	-16.5 ± 0.1
Z1731 [#]	76	75	2.54±0.05	0.53±0.11	6	16.2 ± 0.1

¹ All the annealing experiments were conducted as 5 GPa, 1473 K

* Anhydrous annealing experiments, samples from anhydrous deformation experiments

[#] Hydrus annealing experiments, sample from hydrus deformation experiments

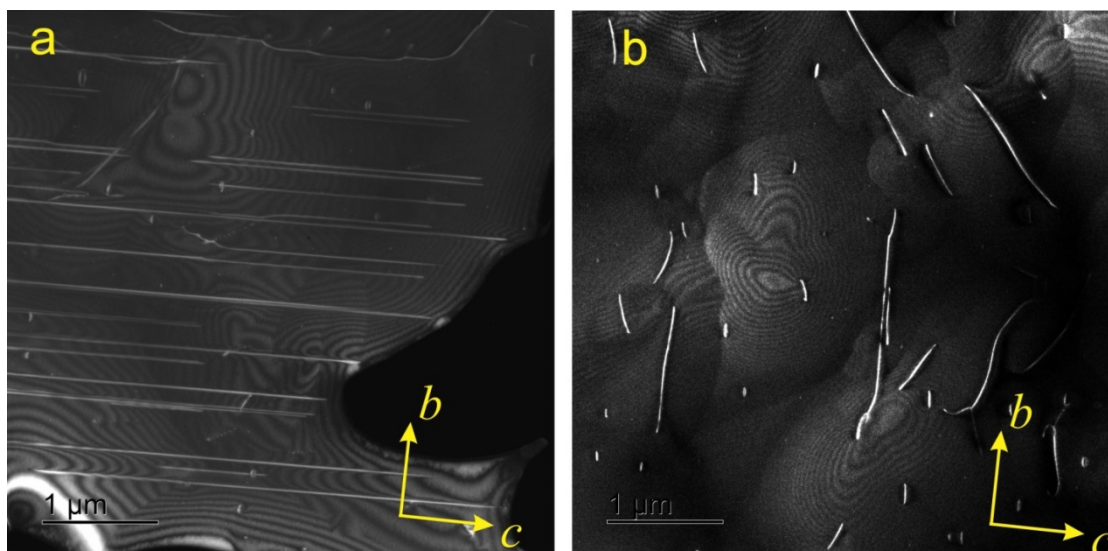


Figure 3. TEM images showing dislocation character changes with water. (a) 7 wt. ppm water. (b) 75 wt. ppm water. Screw and edge dislocations elongate in [001] and [010] direction, respectively.

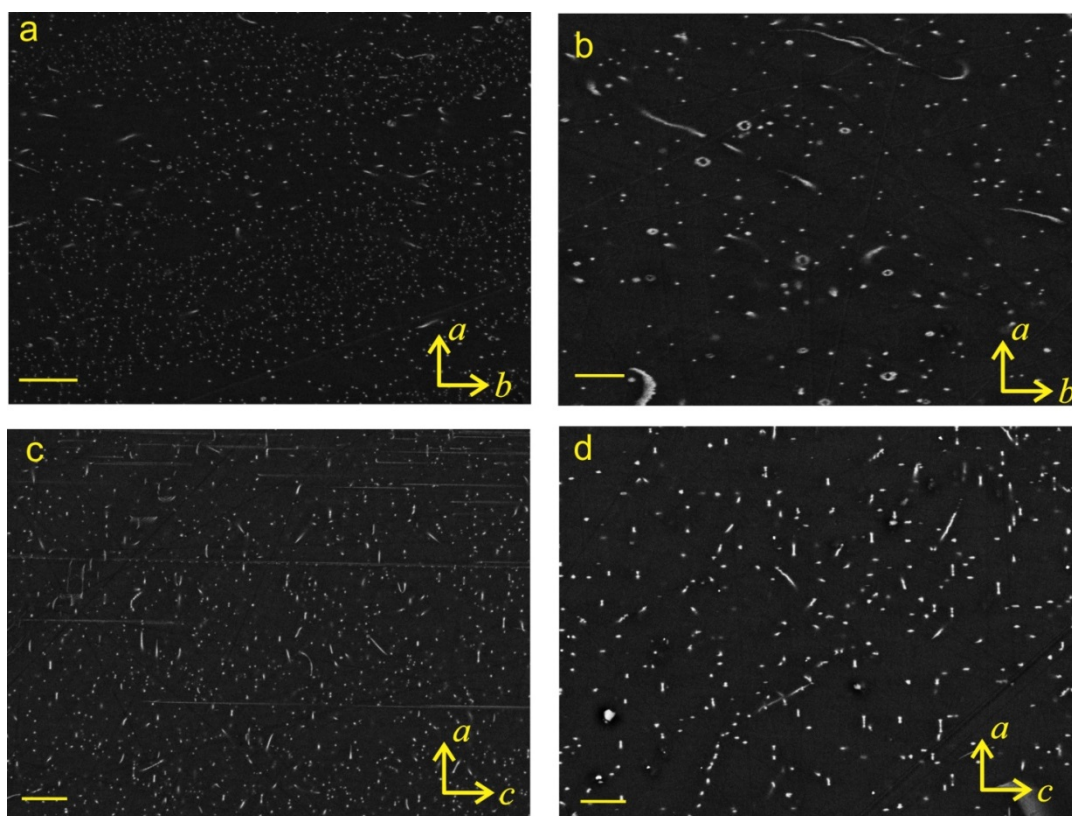


Figure 4. Backscattered electron images of the oxidation-decorated olivine. The bright spots and lines are expected to indicate presence of dislocations. The scale bars denote 2 μm . (a) and (b) are dislocation structure before and after annealing at anhydrous conditions from sample Z1483. (c) and (d) are dislocation structure before and after annealing at hydrous

conditions from sample Z1731.

The FT-IR spectra of samples before and after annealing were shown in Fig. 5. Water content nearly remains constant during annealing. Moreover, the spectra take at rim and center in the hydrous annealed sample are indistinguishable. This indicates the distribution of water in the sample after annealing was nearly homogeneous. The water contents in the samples are below the water solubility in olivine (Kohlstedt et al., 1996).

Figure 6 plots the logarithmic of dislocation annihilation rate constants against the logarithmic of water contents. The fitted water exponent r is 0.3 ± 0.2 . Since the water exponents of the rate constant and dislocation creep are considered identical, we conclude that the water effect on olivine dislocation creep is small.

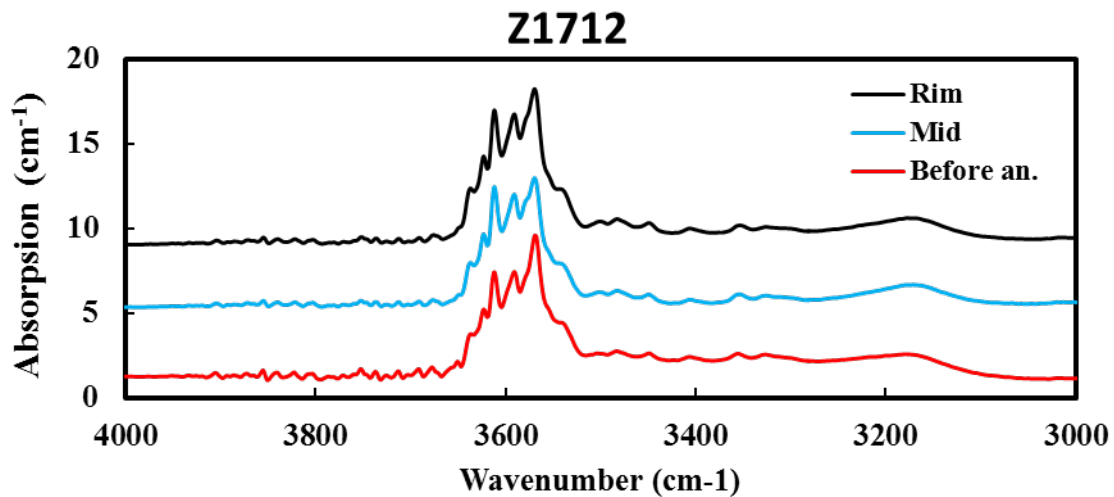
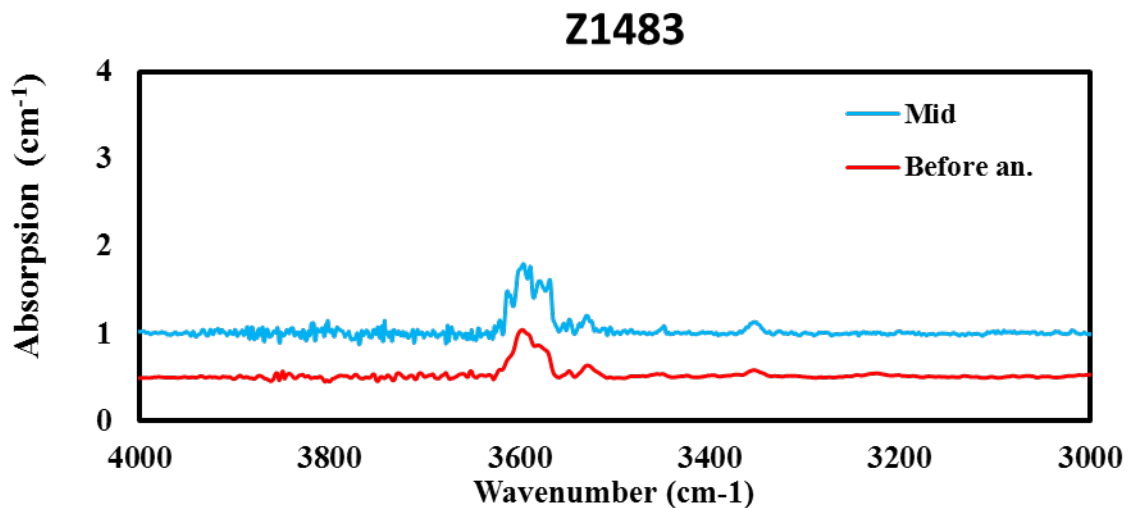


Figure 5. FT-IR spectra after base line correction and thickness normalization to 1 cm. Top: anhydrous annealed sample. Bottom: hydrous annealed sample. The red spectra were obtained before annealing. The blue and black spectra were obtained after annealing at the sample center and rim, respectively.

7.5 Discussion

Comparison with previous studies

The effect of water on olivine dislocation creep has been investigated by deformation experiments. The experiments on olivine aggregate (e.g. Hirth and Kohlstedt, 2003; Mei and Kohlstedt, 2000) render a water exponent of 1.2, which indicates a large effect of water. Since these experiments did not specify the slip systems activated in their experiments, 1.2 can be regarded as the average value of water exponent of all slip systems activated in these experiments. Since the C-type fabric is expected to dominate at high water contents (Jung and Karato, 2001), the water exponent of *c*-dislocations should be higher than 1.2. This contradicts with present results. The possible reason is that the free water existing at grain boundaries in these experiments lubricate the grain boundaries, and therefore enhance the creep rate (Fei et al., 2013). This is supported by deformation experiments on olivine single crystal at hydrous conditions, which renders the water exponent only 0.2 (Mackwell and Kohlstedt, 1985).

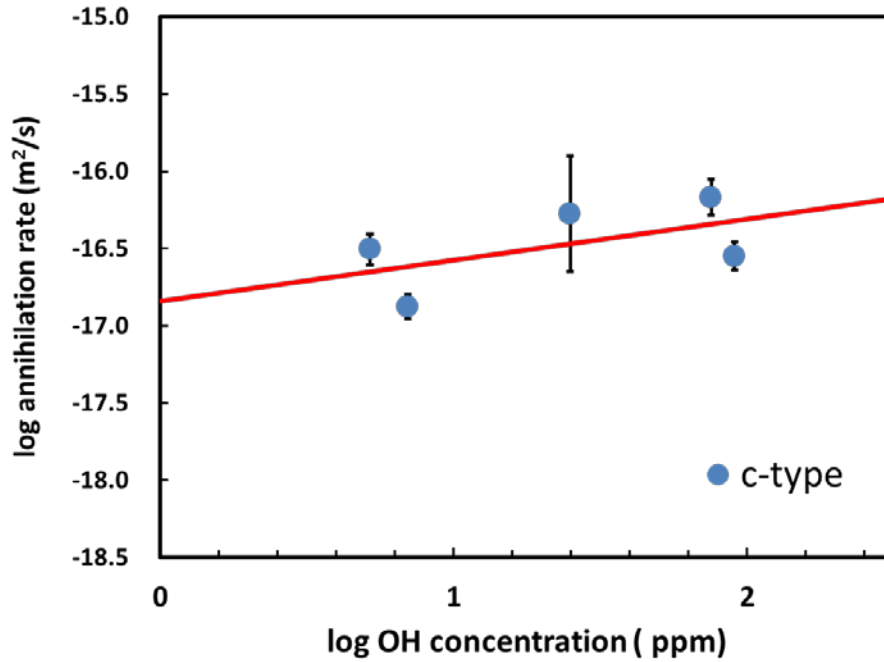


Figure 6. Dislocation annihilation rate constants (k) in the [001](100) slip systems against water content.

Since dislocation creep of olivine is believed to be controlled by Si diffusion at high temperatures, the effect of water on olivine dislocation creep can be understood by studying the effect of water on Si diffusivities in olivine. The rate constants are expected to be proportional to the diffusivity that controls the dislocation motions with a proportional constant 300 (Karato and Ogawa, 1982). Figure 7 compares the diffusivity calculated from rate constants (D^R) and that from previous studies on Si lattice diffusion ($D_{\text{Si}}^{\text{Lat}}$, Fei et al., 2013) and grain-boundary diffusion ($D_{\text{Si}}^{\text{GB}}$, Fei et al., 2016) at different water contents. Diffusion data were normalized to 5 GPa and 1473 K using their activation energies and activation volumes and 10 nm width of grain boundary is assumed when calculate $D_{\text{Si}}^{\text{GB}}$ from Fei et al., (2016). The water dependence of D^R is identical to that of $D_{\text{Si}}^{\text{Lat}}$ and $D_{\text{Si}}^{\text{GB}}$. However, the absolute values differ by orders of magnitude. This indicates dislocation annihilation is not controlled by $D_{\text{Si}}^{\text{Lat}}$ or $D_{\text{Si}}^{\text{GB}}$. Hirth and Kohlstedt (2015) proposed that Si pipe diffusion (D^{Pipe}) may control the deformation. Since vacancies, dislocations and grainboundaries are 0-, 1-, 2-dimension defects, the structure distortion near vacancies is

expected to be higher than that near dislocation cores, which should be higher than that in grain-boundaries. Therefore, it is reasonable to assume that D^{Pipe} lies between $D_{\text{Si}}^{\text{Lat}}$ or $D_{\text{Si}}^{\text{GB}}$. Thus, Si pipe diffusion may control dislocation recovery and therefore dislocation creep of olivine.

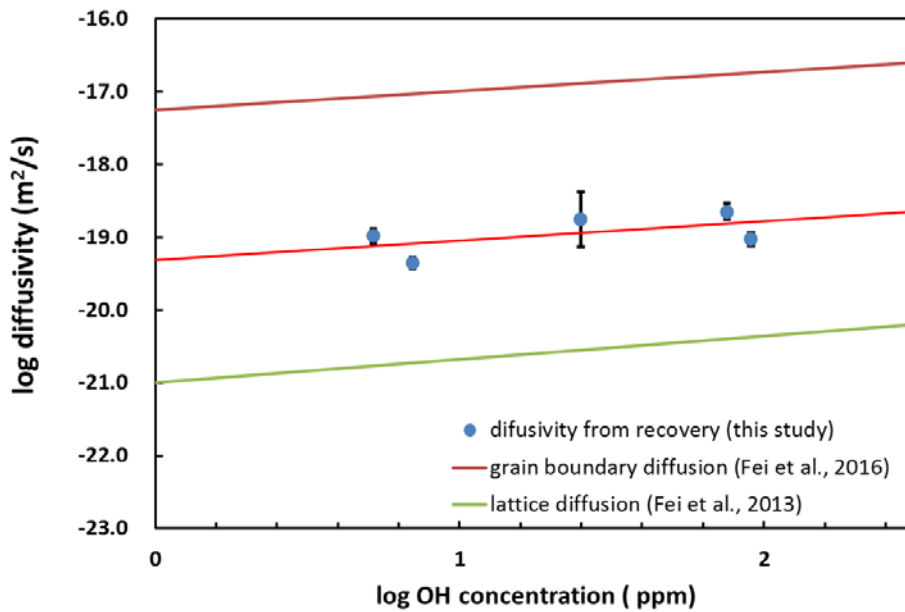


Figure 7. Comparison of Si diffusivities in olivine with diffusivity that controls dislocation motions estimated from dislocation recovery.

Geophysical implications

The small water exponent of olivine dislocation creep indicates water is not the reason for the softening of the asthenosphere. Geophysical observations (e.g. Hager, 1991; Peltier, 1998) and geodynamic modellings (e.g. Becker, 2017; Craig and McKenzie, 1986) suggested that viscosity of the asthenosphere is much lower than that of the lithosphere. Since the asthenosphere contains more water than the lithosphere, the small viscosity of the asthenosphere was explained by hydrous weakening of olivine (Hirth and Kohlstedt, 2003; Karato, 1986). However, based on our study, this explanation is not possible. The water content in olivine at the source of mid-ocean ridge basalt (MORB) is expected to be 810 ppm

H/Si (Hirth and Kohlstedt, 1996). Such amount of water only reduces viscosity of MORB source mantle only by a factor 8. On the other hand, the rapid increase of temperature from lithosphere to asthenosphere (Green and Ringwood, 1967) cause seven orders of magnitude reduction of mantle viscosity from 60 km to 200 km, assuming the activation energy for olivine dislocation creep is 400 kJ/mol (Wang et al., 2016). Therefore, the effect of water on the upper mantle rheology is negligible comparing with temperature effect.

The water induced fabric transition may be impossible judging from present results. Since r of olivine dislocation creep obtained from deformation experiments on olivine aggregate is biased by grain boundary water, we use r from olivine single crystal deformation experiments (Mackwell and Kohlstedt, 1985), which is 0.2, to represent the average water exponent for all slip systems in olivine. This value is identical to our result. Therefore, we conclude that all the slip systems in olivine might have the same water dependence. Thus, the water-induced fabric transitions are unlikely. This hypothesis needs to be checked by further studies on the water effect on other slip systems in olivine.

7.6 Acknowledgements

We thank H. Fischer, R. Njul in BGI for the sample and assembly preparation. This research was supported by DFG grants to TK (KA3434-3/1, KA3434-7/1 and KA3434-8/1) and by the annual budget of BGI.

7.7 References

- Angel, R., Finger, L., 2011. SINGLE: a program to control single-crystal diffractometers. *Journal of Applied Crystallography* 44, 247-251.
- Becker, T.W., 2017. Superweak asthenosphere in light of upper mantle seismic anisotropy. *Geochemistry, Geophysics, Geosystems*.
- Costa, F., Chakraborty, S., 2008. The effect of water on Si and O diffusion rates in olivine and implications for transport properties and processes in the upper mantle. *Physics of the*

- Earth and Planetary Interiors 166, 11-29.
- Craig, C.H., McKenzie, D., 1986. The existence of a thin low-viscosity layer beneath the lithosphere. *Earth and Planetary Science Letters* 78, 420-426.
- Fei, H., Koizumi, S., Sakamoto, N., Hashiguchi, M., Yurimoto, H., Marquardt, K., Miyajima, N., Yamazaki, D., Katsura, T., 2016. New constraints on upper mantle creep mechanism inferred from silicon grain-boundary diffusion rates. *Earth and Planetary Science Letters* 433, 350-359.
- Fei, H., Wiedenbeck, M., Yamazaki, D., Katsura, T., 2013. Small effect of water on upper-mantle rheology based on silicon self-diffusion coefficients. *Nature* 498, 213-+.
- Gose, J., Schmaedicke, E., Markowitz, M., Beran, A., 2010. OH point defects in olivine from Pakistan. *Mineralogy and Petrology* 99, 105-111.
- Green, D., Ringwood, A., 1967. The genesis of basaltic magmas. *Contributions to Mineralogy and Petrology* 15, 103-190.
- Hager, B.H., 1991. Mantle viscosity: A comparison of models from postglacial rebound and from the geoid, plate driving forces, and advected heat flux, Glacial isostasy, sea-level and mantle rheology. Springer, pp. 493-513.
- Hirth, G., Kohlstedt, D., 2003. Rheology of the Upper Mantle and the Mantle Wedge: A View from the Experimentalists, *Inside the Subduction Factory*. American Geophysical Union, pp. 83-105.
- Hirth, G., Kohlstedt, D., 2015. The stress dependence of olivine creep rate: Implications for extrapolation of lab data and interpretation of recrystallized grain size. *Earth and Planetary Science Letters* 418, 20-26.
- Hirth, G., Kohlstedt, D.L., 1996. Water in the oceanic upper mantle: implications for rheology, melt extraction and the evolution of the lithosphere. *Earth and Planetary Science Letters* 144, 93-108.
- Jung, H., Karato, S.-i., 2001. Water-Induced Fabric Transitions in Olivine. *Science* 293, 1460-1463.
- Jung, H., Katayama, I., Jiang, Z., Hiraga, T., Karato, S., 2006. Effect of water and stress on

- the lattice-preferred orientation of olivine. *Tectonophysics* 421, 1-22.
- Karato, S.-i., Wu, P., 1993. Rheology of the upper mantle: a synthesis. *Science* 260, 771-778.
- Karato, S., 1986. Does partial melting reduce the creep strength of the upper mantle? *Nature* 319, 309-310.
- Karato, S., Ogawa, M., 1982. High-pressure recovery of olivine: implications for creep mechanisms and creep activation volume. *Physics of the Earth and Planetary Interiors* 28, 102-117.
- Katayama, I., Jung, H., Karato, S.-i., 2004. New type of olivine fabric from deformation experiments at modest water content and low stress. *Geology* 32, 1045-1048.
- Kohlstedt, D., Keppler, H., Rubie, D., 1996. Solubility of water in the α , β and γ phases of (Mg, Fe) 2SiO_4 . *Contributions to Mineralogy and Petrology* 123, 345-357.
- Kohlstedt, D., Nichols, H., Hornack, P., 1980. The effect of pressure on the rate of dislocation recovery in olivine. *Journal of Geophysical Research: Solid Earth (1978–2012)* 85, 3122-3130.
- Mackwell, S.J., Kohlstedt, D.L., Paterson, M.S., 1985. The role of water in the deformation of olivine single-crystals. *Journal of Geophysical Research-Solid Earth and Planets* 90, 1319-1333.
- Mei, S., Kohlstedt, D.L., 2000. Influence of water on plastic deformation of olivine aggregates 2. Dislocation creep regime. *Journal of Geophysical Research-Solid Earth* 105, 21471-21481.
- Paterson, M., 1982. The determination of hydroxyl by infrared absorption in quartz, silicate glasses, and similar materials. *Bulletin de la Societe Francaise de Mineralogie* 105, 20-29.
- Peltier, W., 1998. Postglacial variations in the level of the sea: Implications for climate dynamics and solid - earth geophysics. *Reviews of Geophysics* 36, 603-689.
- Wang, L., Blaha, S., Pintér, Z., Farla, R., Kawazoe, T., Miyajima, N., Michibayashi, K., Katsura, T., 2016. Temperature dependence of [100](010) and [001](010) dislocation mobility in natural olivine. *Earth and Planetary Science Letters* 441, 81-90.

Acknowledgments

I would like to sincerely express my thanks to my supervisors Prof. Tomoo Katsura for his patience and instruction in my study and life during my Ph.D. I also would like to appreciate Takaaki Kawazoe for his guide and discussion during my study. I also thank Stephan Blaha, Nobuyoshi Miyajima, Prof. Dan Frost, Tiziana Boffa Ballaran, Prof. Hans Keppler, Caroline Bollinger, Florian Heidelberg for their instructions on experimental techniques and discussion about the project.

I thank Joana Polednia for translating the German parts of this thesis and Kirsten Schulze for her kind help to my family. I appreciate all BGI staff, Raphael Njul and Hubert Schulze for preparing samples, Heinz Fischer and Uebelhack Stefan for making cell assemblies and parts, Gerti Golner and Ulrike Trenz for help with chemicals, Stefan Keyssner, Petra Buchert and Lydia Kison-Herzing for administrative and general helps.

I would also like to thank my families. Their supports and encouragements are always valuable for me.

(Eidesstattliche) Versicherungen und Erklärungen

(§ 9 Satz 2 Nr. 3 PromO BayNAT)

Hiermit versichere ich eidesstattlich, dass ich die Arbeit selbstständig verfasst und keine anderen als die von mir angegebenen Quellen und Hilfsmittel benutzt habe (vgl. Art. 64 Abs. 1 Satz 6 BayHSchG).

(§ 9 Satz 2 Nr. 3 PromO BayNAT)

Hiermit erkläre ich, dass ich die Dissertation nicht bereits zur Erlangung eines akademischen Grades eingereicht habe und dass ich nicht bereits diese oder eine gleichartige Doktorprüfung endgültig nicht bestanden habe.

(§ 9 Satz 2 Nr. 4 PromO BayNAT)

Hiermit erkläre ich, dass ich Hilfe von gewerblichen Promotionsberatern bzw. -vermittlern oder ähnlichen Dienstleistern weder bisher in Anspruch genommen habe noch künftig in Anspruch nehmen werde.

(§ 9 Satz 2 Nr. 7 PromO BayNAT)

Hiermit erkläre ich mein Einverständnis, dass die elektronische Fassung meiner Dissertation unter Wahrung meiner Urheberrechte und des Datenschutzes einer gesonderten Überprüfung unterzogen werden kann.

(§ 9 Satz 2 Nr. 8 PromO BayNAT)

Hiermit erkläre ich mein Einverständnis, dass bei Verdacht wissenschaftlichen Fehlverhaltens Ermittlungen durch universitätsinterne Organe der wissenschaftlichen Selbstkontrolle stattfinden können.

.....
Ort, Datum, Unterschrift